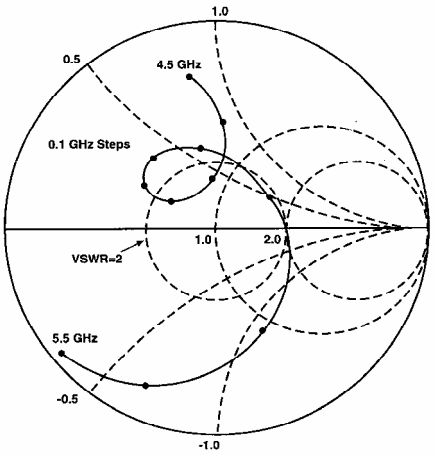

Applied Computational Electromagnetics Society Journal

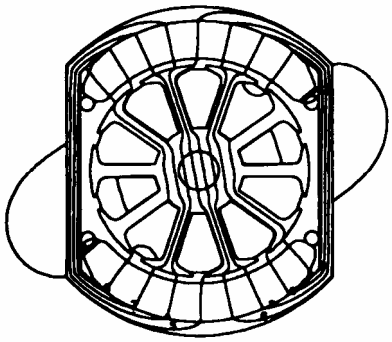

Editor-in-Chief
Atef Z. Elsherbeni

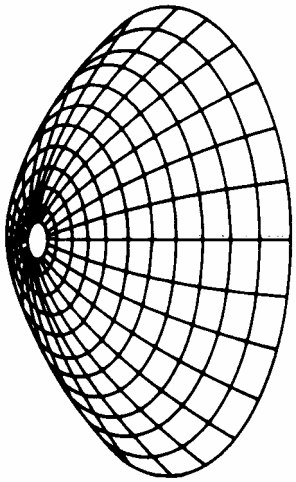

June 2008
Vol. 23 No. 2
ISSN 1054-4887

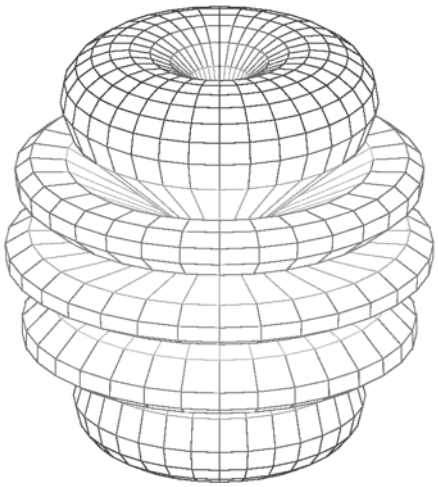

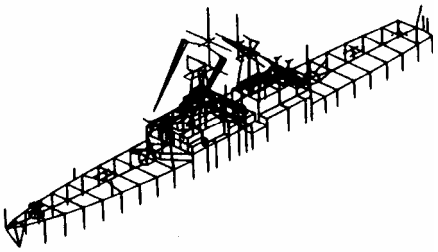

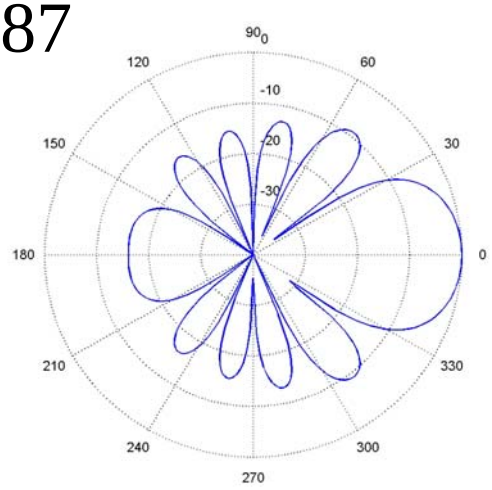

GENERAL PURPOSE AND SCOPE: The Applied Computational Electromagnetics Society ***(ACES)*** Journal hereinafter known as the ***ACES Journal*** is devoted to the exchange of information in computational electromagnetics, to the advancement of the state-of-the art, and the promotion of related technical activities. A primary objective of the information exchange is the elimination of the need to "re-invent the wheel" to solve a previously-solved computational problem in electrical engineering, physics, or related fields of study. The technical activities promoted by this publication include code validation, performance analysis, and input/output standardization; code or technique optimization and error minimization; innovations in solution technique or in data input/output; identification of new applications for electromagnetics modeling codes and techniques; integration of computational electromagnetics techniques with new computer architectures; and correlation of computational parameters with physical mechanisms.

SUBMISSIONS: The ***ACES Journal*** welcomes original, previously unpublished papers, relating to applied computational electromagnetics. Typical papers will represent the computational electromagnetics aspects of research in electrical engineering, physics, or related disciplines. However, papers which represent research in applied computational electromagnetics itself are equally acceptable.

Manuscripts are to be submitted through the upload system of ***ACES*** web site http://aces.ee.olemiss.edu See "Information for Authors" on inside of back cover and at ***ACES*** web site. For additional information contact the Editor-in-Chief:

Dr. Atef Elsherbeni
Department of Electrical Engineering
The University of Mississippi
University, MS 386377 USA
Phone: 662-915-5382 Fax: 662-915-7231
Email: atef@olemis.edu

SUBSCRIPTIONS: All members of the Applied Computational Electromagnetics Society who have paid their subscription fees are entitled to receive the ***ACES Journal*** with a minimum of three issues per calendar year and are entitled to download any published journal article available at http://aces.ee.olemiss.edu.

Back issues, when available, are $15 each. Subscriptions to ***ACES*** is through the web site. Orders for back issues of the ***ACES Journal*** and changes of addresses should be sent directly to ***ACES***:

Dr. Allen W. Glisson
302 Anderson Hall
Dept. of Electrical Engineering
Fax: 662-915-7231
Email: aglisson@olemiss.edu

Allow four week's advance notice for change of address. Claims for missing issues will not be honored because of insufficient notice or address change or loss in mail unless the Executive Officer is notified within 60 days for USA and Canadian subscribers or 90 days for subscribers in other countries, from the last day of the month of publication. For information regarding reprints of individual papers or other materials, see "Information for Authors".

LIABILITY. Neither ***ACES***, nor the ***ACES Journal*** editors, are responsible for any consequence of misinformation or claims, express or implied, in any published material in an ***ACES Journal*** issue. This also applies to advertising, for which only camera-ready copies are accepted. Authors are responsible for information contained in their papers. If any material submitted for publication includes material which has already been published elsewhere, it is the author's responsibility to obtain written permission to reproduce such material.

APPLIED COMPUTATIONAL ELECTROMAGNETICS SOCIETY JOURNAL

Editor-in-Chief
Atef Z. Elsherbeni

June 2008
Vol. 23 No. 2
ISSN 1054-4887

The ACES Journal is abstracted in INSPEC, in Engineering Index, DTIC, Science Citation Index Expanded, the Research Alert, and to Current Contents/Engineering, Computing & Technology.

The first, fourth, and sixth illustrations on the front cover have been obtained from the Department of Electrical Engineering at the University of Mississippi.

The third and fifth illustrations on the front cover have been obtained from Lawrence Livermore National Laboratory.

The second illustration on the front cover has been obtained from FLUX2D software, CEDRAT S.S. France, MAGSOFT Corporation, New York.

THE APPLIED COMPUTATIONAL ELECTROMAGNETICS SOCIETY

JOURNAL

Vol. 23 No. 2 June 2008

TABLE OF CONTENTS

The Floating PML Applied to Practical FDTD Applications

M. Wong and A. R. Sebak

Concordia University, Montreal, Quebec
mich_won@ece.concordia.ca

Abstract – In this paper we present the Floating Perfectly Matched Layer (Floating PML) where a "floating" PML is implemented within the solution space without making contact with the main PML walls. The Floating PML can be used as a terminating technique within the solution space of the Finite Difference Time Domain (FDTD) Method. The formulation of the Floating PML is based on an optimized implementation of the Convolutional PML (CPML), which is discussed briefly in the Appendix. In this paper we present benchmark validation tests, applications using the Floating PML, as well as some advantages and disadvantages of this method.

I. INTRODUCTION

The Finite Difference Time Domain (FDTD) method is an extremely versatile, simple computational tool that has been used extensively in recent applications involving electromagnetics [1, 2]. In general, the FDTD method requires the truncation of the solution space so that an infinitely large solution space is not required to simulate free space. This problem of terminating the solution space has been an important component in the development of the FDTD method, and continues to be an area of active research [3].

When investigating various transmission line structures such as microstrips, striplines, or waveguides, it is convenient to terminate the line at the edge of the solution space. This is a common terminating technique as shown in Fig. 1 [2, 4]. This type of port is often used because the termination of a transmission line in a PML, which simulates an infinitely long transmission line, is very convenient to implement in the FDTD method and ensures a very low return loss which does not interfere with the analysis of the structure itself.

It is, however, often necessary to terminate the transmission line within the solution space instead of at its edge. This type of termination, often called a port, is used so that the entire structure may be simulated without any contact to any Absorbing Boundary Condition (ABC) or Perfectly Matched Layer (PML) at the edge of the solution space. This is necessary so that a radiation box may surround the structure to perform a near to far field operation, so that the finite size of a device may be taken into account during a simulation, or so that the port itself may be surrounded by other devices. An example of this is shown in Fig. 2.

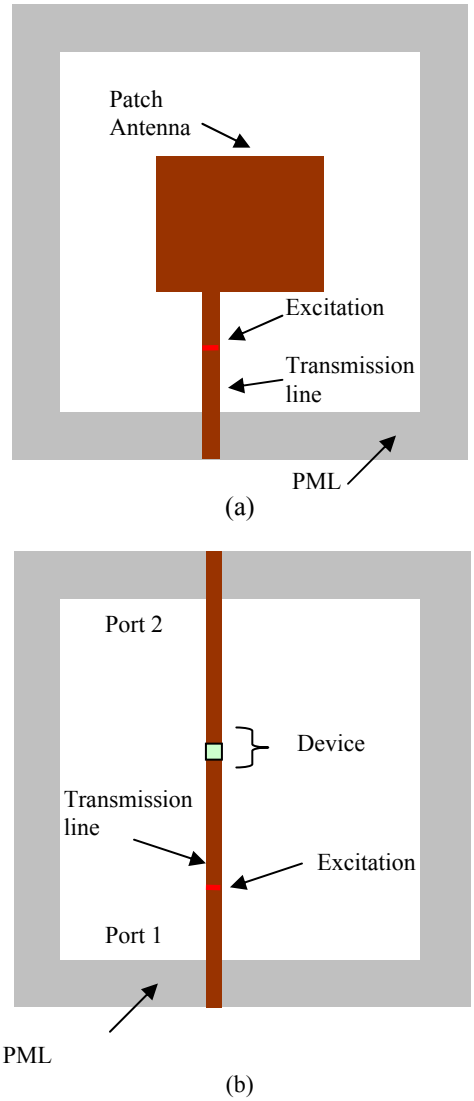

Fig. 1. Common terminating techniques applied to FDTD, (a) microstrip patch antenna [4] with a transmission line terminated in the PML and (b) circuit modeling for arbitrary lumped elements (Device) using the main PML for termination of the 2 ports [2].

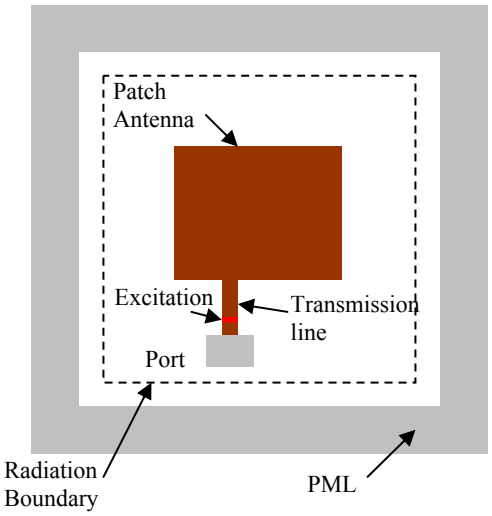

(a)

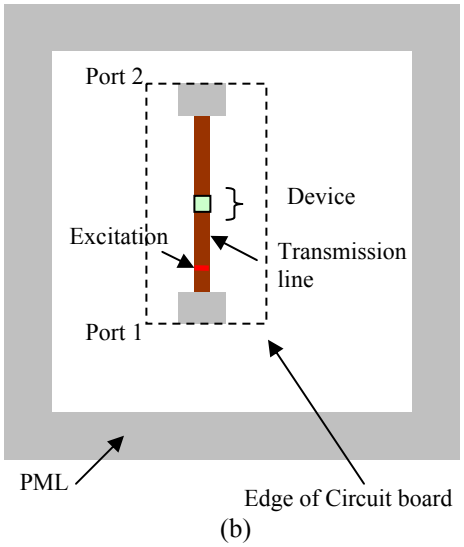

(b)

Fig. 2. Terminating technique when (a) a radiation pattern must be found and (b) finite ground plane of a circuit must be taken into account.

Various techniques have been reported for implementing a port within the solution space. Luebbers and Langdon [5] have implemented a resistive source, and Schuster and Luebbers have terminated transmission lines with lumped loads [6] using a recursive convolution technique. Piket-May and Taflove [7] have implemented similar loads, however, their results show that the resistor generates parasitic capacitance at frequencies above 1 GHz. Recently, the Lumped Element FDTD Method has been introduced which can model high-speed microwave circuit networks consisting of active and passive devices within a single Yee cell [2, 8]. This type of element can also be used to simulate a port within the solution space.

In this paper we present an alternative approach which implements the termination of a port using a PML within the solution space [9] away from the main PML wall. In some cases we may prefer to model a port as an infinitely long transmission line within the solution space, as opposed to a lumped element attached to a transmission line. To achieve this, we introduce an optimized Convolutional Perfectly Matched Layer (CPML) formulation that fully separates PML equations from FDTD equations, as discussed in the Appendix. Adding the PML within the solution space then becomes simple and very useful. This technique is referred to as the Floating PML [9], since this PML does not touch the external walls of the solution space and can therefore act as a port. This method results in a wideband operation with low radiation losses where results are discussed in the following sections.

We begin with the discussion of the Floating PML and describe its "physical" structure. Benchmark tests are then performed, followed by examples of practical electromagnetic applications. The optimized CPML formulation is included in Appendix A.

II. INTRODUCING THE FLOATING PML

As discussed in the introduction, there exist various methods to terminate a port using a resistor or lumped elements within the solution space, however, the Floating PML provides wideband characteristics simply by the nature of its structure since it models an infinitely long transmission line.

In addition, some methods such as microstrip termination using the resistive voltage source suffer from parasitic capacitance above 1 GHz [7]. This limits its potential for use at high frequencies. The Floating PML described in this section is extremely wideband by comparison and is perhaps a better choice for higher frequencies.

The PML in a regular solution space is typically surrounded by metallic walls [3] as shown in Fig. 3. This technique ensures a "double" attenuation of incoming waves, since they are attenuated as the hit the PML, and attenuated again as they are reflected. The Floating PML is implemented in a similar way, that is, with a metallic box surrounding the PML. It was found that for this implementation of the Floating PML, the PEC box was required to maintain stability of the solution space.

During simulations of microstrip and stripline structures, it was found that it is best to model the PEC box with a transmission line as a rectangular coaxial cable as discussed in [11]. Using this model, it is possible to model the PEC walls at a distance large enough to avoid interaction with the transmission line.

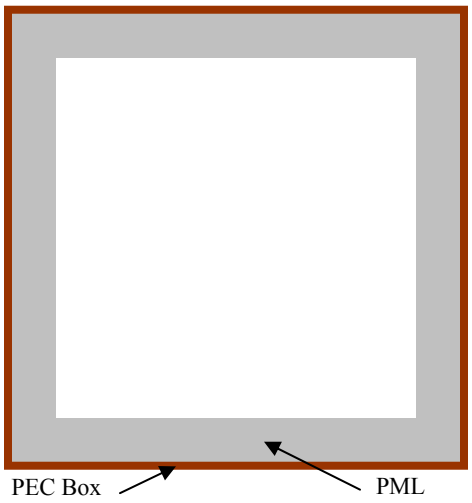

Fig. 3. Use of a PEC box in (a) the main PML wall in a typical solution space and (b) with the floating PML, modeled as a rectangular coaxial cable [11].

There are some advantages and disadvantages of the Floating PML as a terminating technique. One disadvantage is that the PEC box will affect the simulation, however, this box is not more intrusive than an SMA connector used during real measurements. The PEC box has the advantage that there are very low radiation losses at the port compared to resistive loads. An additional advantage is that the PEC box is well suited to waveguide applications. The Floating PML is extremely wideband simply by the nature of the structure itself because the port is modeled as an infinitely long transmission line. One problem that was encountered during simulation was that the Floating PML did not perform as well for microstrip terminations as for stripline terminations as is discussed in the following sections in this paper. Finally, the Floating PML is very easy to implement using the optimized CPML formulation discussed in the Appendix, however, requires more computational resources than a resistive source.

III. BENCHMARK PERFORMANCE OF THE FLOATING PML

In this section we measure the return loss performance of the Floating PML over a large frequency range from 0 to 20 GHz. A good return loss indicates that the port absorbs most of the incoming waves, thus not interfering with reflected waves from the simulated structure.

A. Stripline Applications

In this example, we examine a stripline structure that terminates in the PML wall on one side, and in the Floating PML on the other side as shown in Fig. 4. In this test, we attempt to attain the lowest possible return loss for a Gaussian incident pulse on the Floating PML.

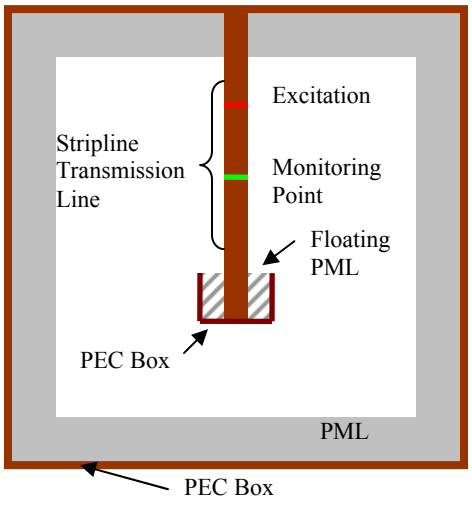

Fig. 4. Structure for the benchmark test for the stripline transmission line incident on the floating PML.

For the test as shown in Figs. 4 and 5, we have run various widths for the PEC box. It was found that a larger width of box provided fewer reflections.

In Fig. 6 we show that the return loss for the stripline incident on the Floating PML has a very wideband performance with a return loss of better than 50 dB from 0 GHz to 20 GHz. The number of cells represents the distance from the PEC box to the trace.

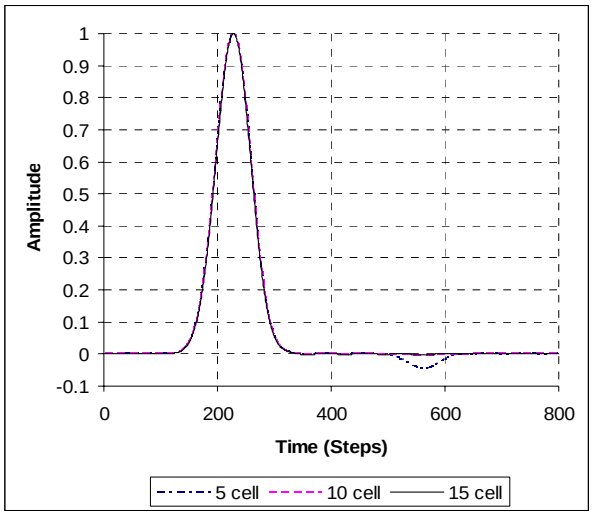

Fig. 5. Time-domain simulation for various widths of the PEC box. The number of cells represents distance on either side of the transmission line between the line and the PEC wall. Each cell is 0.2 mm large.

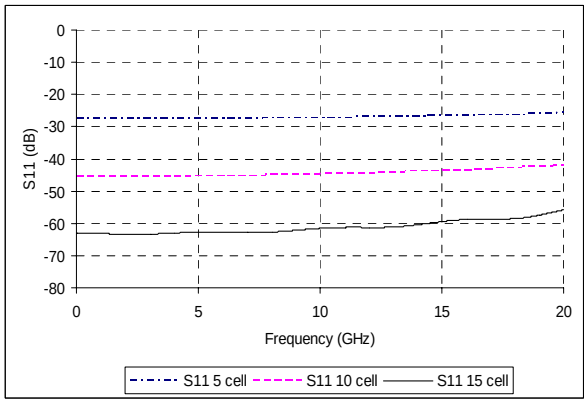

Fig. 6. Return loss for the stripline incident on the floating PML for differently sized PEC boxes.

B. Microstrip Applications

In this section we examine a microstrip transmission line terminating in a Floating PML as shown in Fig. 7. The transmission line is 1.88 mm wide and lies on a 0.813 mm thick Rogers 5880 substrate, with a dielectric constant of 3.38. The Floating PML consists of the PML material surrounded by a PEC box. The bottom half of the box is filled with the Rogers 5880 substrate, while the top half of the box is filled with air.

In this method, the PEC box is made large enough to reduce the interaction of the fields traveling along the microstrip line with the PEC box. The size of the cells is 0.31374 mm wide in the x and y directions, and 0.20325 mm tall in the z direction.

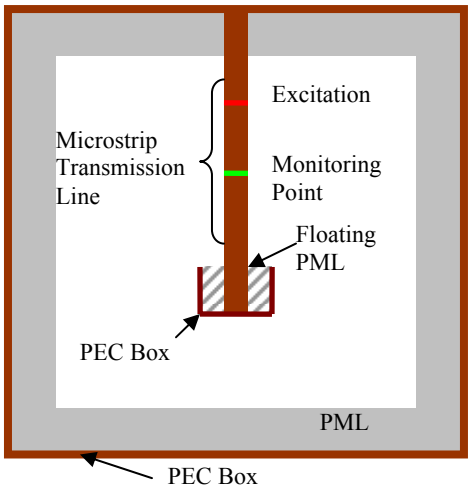

Fig. 7. Structure for the benchmark test of a microstrip transmission line incident on a floating PML. The top half of the floating PML box is filled with air. The bottom half is filled with the same dielectric as the substrate. The whole floating PML box is filled with PML material.

In Fig. 8. we have simulated various sizes for the PEC box. It was found that a larger box provided a fewer reflections. The number of cells represents the distance from the trace in both the x and z directions.

In Fig. 9. we show that for a larger PEC box, the return loss is improved. This correlates with the fewer reflections seen in Fig. 8. The performance for the microstrip case is not as good as for the stripline case because of the difference in dielectric constant throughout the Floating PML.

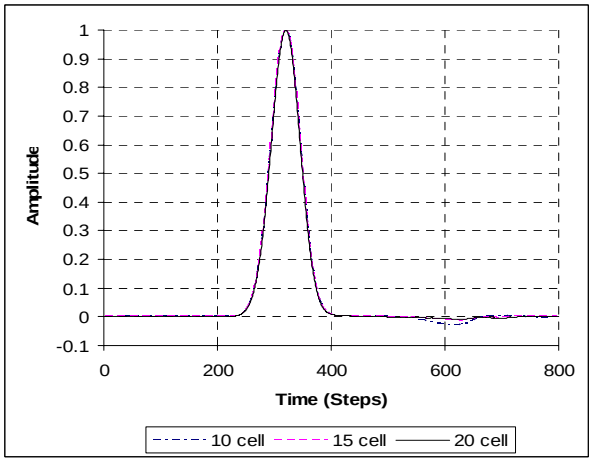

Fig. 8. Time domain comparison of Floating PML. The incident wave is clearly visible while the reflected wave is barely visible around 600th time step. The number of cells from the trace to the PEC box in the x and z directions are shown in the legend.

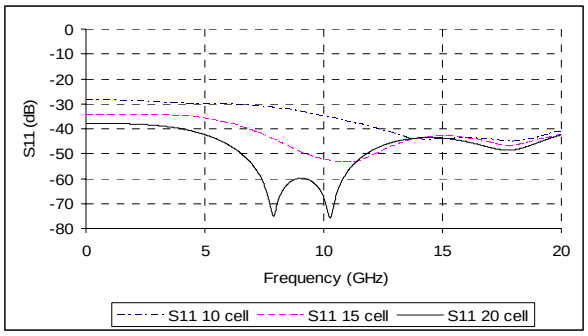

Fig. 9. Return loss for the microstrip incident on the Floating PML for differently sized PEC boxes.

IV. APPLICATIONS

In this section we examine two practical applications of the Floating PML: the microstrip-fed slot antenna, and the dual band dual slot stripline antenna.

A. Microstrip-Fed Slot Antenna

The microstrip slot antenna to be studied is shown in Fig. 10. This problem is particularly problematic for termination of the microstrip line because the impedance match is very narrow, leading to a large reflected pulse with long duration and interaction with the PML. In this example a Floating PML was used to obtain results that were similar to the published results for the antenna pattern [12]. In the published results, the microstrip line is terminated in a lumped element instead of a Floating PML.

As we can see from the results in Fig. 11, the return loss using the Floating PML matched simulated results using the Lumped Load method [13], as well as measured results [13].

In Fig. 12, we show that the antenna pattern matched the measured pattern and the pattern simulated using the LE-FDTD method.

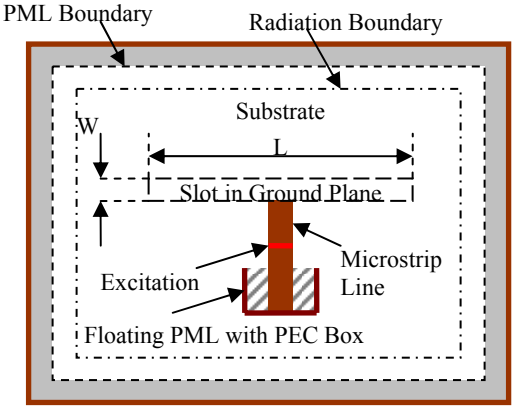

Fig. 10. The microstrip-fed slot antenna.

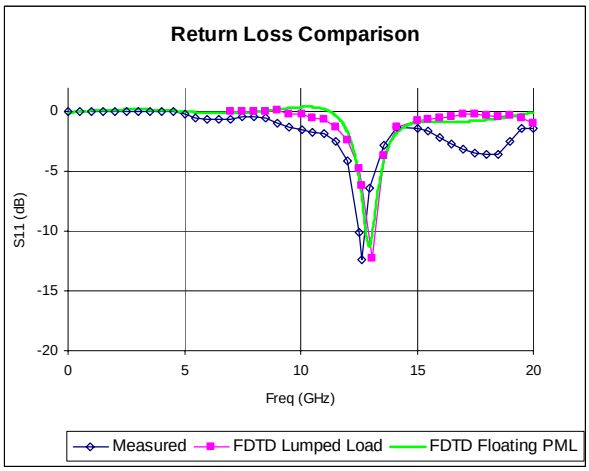

Fig. 11. Return loss comparison between the Lumped load method as in [13], the Floating PML, and measured [13] results.

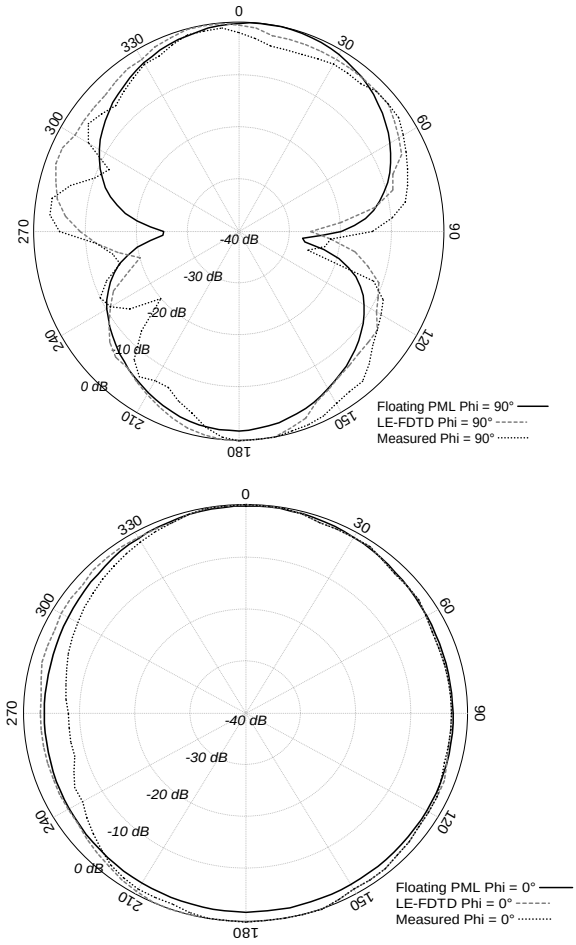

Fig. 12. Measured [12], LE-FDTD simulated [12], and Floating PML simulated antenna patterns at 13 GHz for simple slot antenna along Phi = 0 (X-Z Plane) and Phi = 90 (Y-Z Plane).

B. Dual Band Dual Slot Stripline Antenna

In this example we examine a stripline application [14] for the Floating PML as shown in Fig. 13. The stripline is used to feed dual slots which act as a single antenna with dual bands. The stripline is excited on both sides of the trace, as shown in Fig. 14. The dimensions are given in Table 1. The pulse travels in both directions, where on one side the pulse is absorbed by the Floating PML and the pulse continues to travel towards the dual slots.

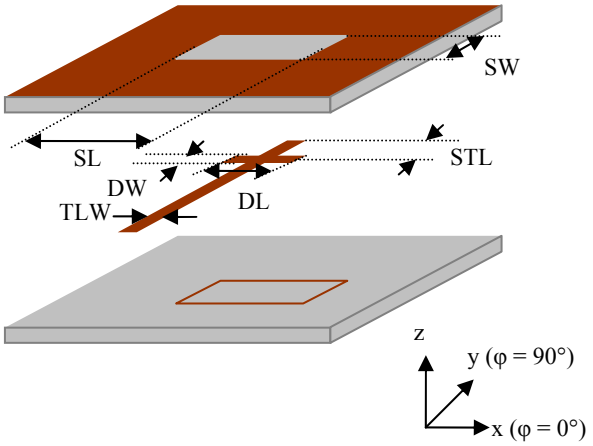

Fig. 13. The dual band dual slot stripline antenna [14]. (for dimensions see Table 1).

Table 1. Dual slot stripline antenna dimensions.

Dimension	Size (cells)	Physical Size (mm)	Description
TLW	8	2.6	Width of transmission line
STL	17	4.25	Stub length
SW	56	14	Width of slot
SL	120	39	Length of slot
h	5	1.575	Height of each substrate
DL	16	5.2	Length of tuning stub
DW	4	1.0	Width of tuning stub

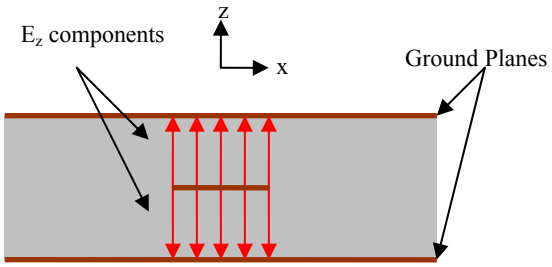

Fig. 14. Excitation of stripline structure.

In Fig. 15, we can see that the return loss of the Floating PML matches the return loss calculated using Ansoft Designer and measured results.

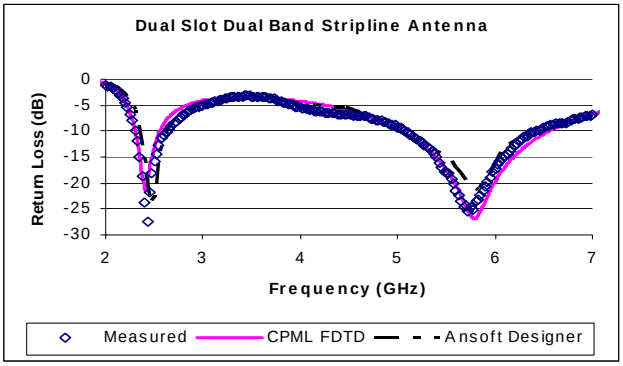

Fig. 15. Simulated return loss of dual band dual slot stripline antenna [14].

In Figs. 16 and 17, we show both the antenna co- and cross-polarization patterns at 2.45 GHz and 5.2 GHz, respectively. The results based on the Floating PML match those of the measured antenna. At both frequencies, it is noticed that E-plane cross-polarization is less than -40 dB.

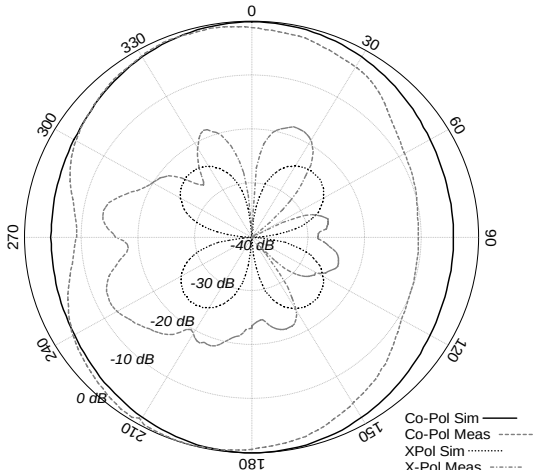

Fig. 16a. Antenna patterns at 2.45GHz: φ = 0° H-Plane.

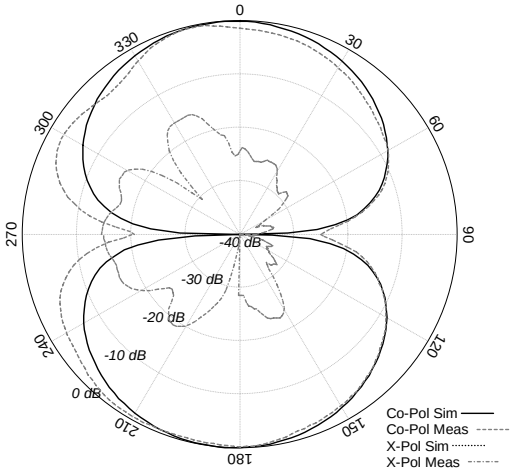

Fig. 16b. Antenna patterns at 2.45 GHz, φ=90° E-Plane.

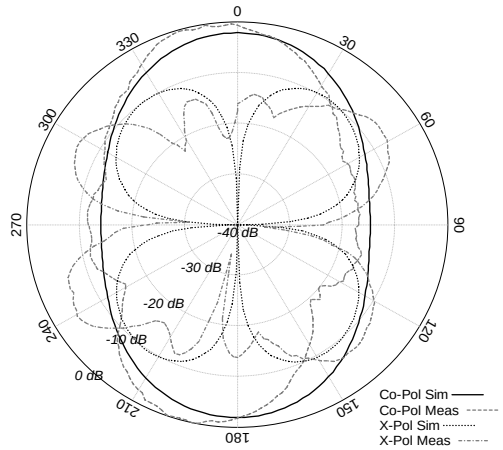

Fig. 17a. Antenna patterns at 5.8 GHz: φ = 0° H-Plane.

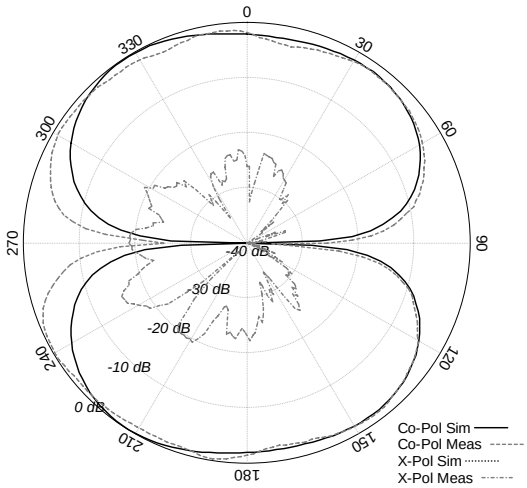

Fig. 17b. Antenna patterns at 5.8 GHz: φ = 90° E-Plane.

V. CONCLUSION

In this paper, the Floating PML, a new application for the CPML is introduced and discussed. Two benchmark cases to measure the return loss performance of the proposed Floating PML are considered for stripline and microstrip structures. Numerical results for microstrip-fed slot and for a dual band dual slot stripline antenna supporting the optimized CPML formulation and the Floating PML are then presented. In the Appendix we discuss the implementation of an optimized version of the CPML, where the κ tensor parameters (PML coefficients) have been removed from the main FDTD equations. It is successfully shown that it is possible to implement the Floating PML within the solution space as a port, as long as it is surrounded by a PEC box, meaning it is closed on five of the six sides of the box.

REFERENCES

[1] Y. Zhang and S.-W. Lu, "Genetic algorithm in reduction of numerical dispersion of 3-D alternating-direction-implicit finite-difference time-domain method," *IEEE Trans. on Microwave Theory and Techniques*, vol. 55, no. 5, pp. 966 - 973, May 2007.

[2] C.-C. Wang and C.-W. Kuo, "An efficient scheme for processing arbitrary lumped multiport devices in the finite-difference time-domain method," *IEEE Trans. on Microwave Theory and Techniques*, vol. 55, no. 5, pp. 958 – 965, May 2007.

[3] A. Taflove and S. C. Hagness, *Computational Electrodynamics The Finite-Difference Time-Domain Method*, Third Edition, Artech House, 2005.

[4] D. M. Sheen, S. M. Ali, M. D. Abouzahra, and J. A. Kong, "Application of the three-dimensional finite-difference time-domain method to the analysis of planar microstrip circuits," *IEEE Trans. on Microwave Theory and Techniques,* vol. 38, no. 7, pp. 849 – 857, July 1990.

[5] R. J. Luebbers and H. S. Langdon, "A simple feed model that reduces time steps needed for FDTD antenna and microstrip calculations," *IEEE Trans. on Antennas and Propagation*, vol. 44, no. 7, pp. 1000 – 1005, July 1996.

[6] J. W. Schuster, R. J. Luebbers, and T. G. Livernois, "Application of the recursive convolution technique to modeling lumped circuit elements in FDTD simulations," *IEEE Antennas and Propagation Society International Symposium*, vol. 4, pp. 1792 – 1795, 21-26 June 1998.

[7] M. Piket-May, A. Taflove, and J. Baron, "FD-TD modeling of digital signal propagation in 3-D circuits with passive and active loads," *IEEE Trans. on Microwave Theory and Techniques*, vol. 42, no. 8, pp. 1514 – 1523, August 1994.

[8] J. A. Pereda, F. Alimenti, P. Mezzanotte, L. Roselli, and R. Sorrentino, "A new algorithm for the incorporation of arbitrary linear lumped networks into FDTD simulators," *IEEE Trans. on Microwave Theory and Techniques*, vol. 47, no. 6, Part 2, pp. 943 – 949, June 1999.

[9] M. Wong and A. R. Sebak, "The Floating PML: a novel CPML application," *ANTEM/URSI Conference Ecole Polytechnqiue*, Montreal, QC, Canada, pp. 601, 17-19 July 2006.

[10] S. D. Gedney, "An anisotropic PML absorbing media for FDTD simulation of fields in lossy dispersive media," *Electromagnetics*, vol. 16, pp. 399-415, 1996.

[11] M. Wong, B. M. Hobson, and A. R. Sebak, "A coaxial to waveguide feeding method for substrate integrated waveguides," *EMTS 2007 International URSI – Commission B Electromagnetic Theory Symposium*, Fairmount Chateau Laurier, Ottawa, 26-28 July 2007.

[12] M. Cryan, S. Helbing, F. Alimenti, P. Mezzanotte, L. Roselli, and R. Sorrentino, "Analysis and design of quasi-optical multipliers using lumped element (LE)-FDTD method," *IEEE Antennas and Propagation Society International Symposium*, vol. 1, pp. 100 - 103, 11-16 July 1999.

[13] M. Cryan, S. Helbing, F. Alimenti, P. Mezzanotte, L. Roselli, and R. Sorrentino, "Analysis and design of quasi-optical multipliers using lumped element (LE)-FDTD method," *IEEE Antennas and Propagation Society International Symposium*, vol. 1, pp. 100 -103, 11-16 July 1999.

[14] M. Wong, A. R. Sebak, and T. A. Denidni, "Analysis of a Dual-Band Dual Slot omnidirectional stripline antenna," *IEEE Antennas and Wireless Propagation Letters*, vol. 6, pp. 199 - 202, 2007.

APPENDIX A: AN OPTIMIZED CPML FORMULATION: ISOLATION OF CPML COEFFICIENTS

The CPML formulation is very efficient in its implementation due to the fact that the recursively calculated CPML components (see equation (2)) need only be calculated and added to the individual vector components within the PML [3]. Conversely, the Uniaxial Perfectly Matched Layer (UPML) requires the computation of the PML components throughout the entire solution space, requiring a much larger amount of computation time [3].

The complex frequency shifted (CFS) tensor allows the CPML to absorb waves of low frequency or long duration, since the denominator does not approach zero at DC [3]. It is given as,

$$s_w = \kappa_w + \frac{\sigma_w}{a_w + j\omega\varepsilon}. \quad (1)$$

The "a" term in the denominator is added to prevent the denominator from approaching zero when the radian frequency "ω" approaches zero and has no physical significance. "ε" and "σ" are properties of the material. "κ" has a value of 1.0 throughout the solution space, however, these κ coefficients can be greater than 1.0 in the CPML region to effectively scale the mesh so that at incoming wave is more effectively attenuated [3]. The subscripts w and v represent vectors perpendicular to the wave propagation.

The recursively calculated CPML component using the CFS tensor in equation (1) is given as [10],

$$\psi_{w,v}(n) = b_w \psi_{w,v}(n-1) + c_w \frac{\partial}{\partial w} H_v(n) \quad (2)$$

where

$$b_w = \exp\left[-\left(\frac{\sigma_w}{\varepsilon_o \kappa_w} + \frac{a_w}{\varepsilon_o}\right)\Delta t\right],$$

$$c_w = \frac{\sigma_w}{\sigma_w \kappa_w + \kappa_w^2 a_w}\left[\exp\left[-\left(\frac{\sigma_w}{\varepsilon_o \kappa_w} + \frac{a_w}{\varepsilon_o}\right)\Delta t\right] - 1\right].$$

As discussed above, the κ tensor parameters as given in equation (1) and implemented in the CPML in equation (2) have a value of 1.0 throughout the main solution space, however, still appear within the standard CPML formulation as shown in equation (3) [10]. If left in this format, the software needs to either store values of κ = 1.0 throughout the solution space, or check to see if the computation lies within the PML to compute a set of FDTD equations without the κ component.

In this section we present a solution to this problem. It is possible to remove the κ component from the CPML FDTD in equation (3), to reduce storage requirements or simplify the programming, depending on the implementation. The equations within the FDTD computation region then reduce to the standard Yee equations. This yields optimal simplicity / accuracy within the computational region and increases running speed / reduces storage at the same time.

Consider the standard E field updates equation in the CPML region,

$$E_x\Big|_{i+1/2,j,k}^{n+1/2} = C_{ax}\Big|_{i+1/2,j,k} Ex\Big|_{i+1/2,j,k}^{n-1/2} + C_{bx}\Big|_{i+1/2,j,k} \left(\begin{array}{l} \dfrac{H_z\Big|_{i+1/2,j+1/2,k}^{n} - H_z\Big|_{i+1/2,j-1/2,k}^{n}}{\kappa_{yj}\Delta y} - \\ \dfrac{H_y\Big|_{i+1/2,j,k+1/2}^{n} - H_y\Big|_{i+1/2,j,k-1/2}^{n}}{\kappa_{zk}\Delta z} \\ + \psi_{Ex,y}\Big|_{i+1/2,j,k}^{n} - \psi_{Ex,z}\Big|_{i+1/2,j,k}^{n} \end{array} \right). \quad (3)$$

Without loss of generality, this may be written as

$$E_x\Big|_{i+1/2,j,k}^{n+1/2} = C_{ax}\Big|_{i+1/2,j,k} Ex\Big|_{i+1/2,j,k}^{n-1/2} + C_{bx}\Big|_{i+1/2,j,k} \left(\begin{array}{l} \left[\begin{array}{l} \dfrac{H_z\Big|_{i+1/2,j+1/2,k}^{n} - H_z\Big|_{i+1/2,j-1/2,k}^{n}}{\Delta y} - \\ \dfrac{H_z\Big|_{i+1/2,j+1/2,k}^{n} - H_z\Big|_{i+1/2,j-1/2,k}^{n}}{\Delta y} \end{array} \right] \\ + \dfrac{H_z\Big|_{i+1/2,j+1/2,k}^{n} - H_z\Big|_{i+1/2,j-1/2,k}^{n}}{\kappa_{yj}\Delta y} \\ - \left[\begin{array}{l} \dfrac{H_y\Big|_{i+1/2,j,k+1/2}^{n} - H_y\Big|_{i+1/2,j,k-1/2}^{n}}{\Delta z} - \\ \dfrac{H_y\Big|_{i+1/2,j,k+1/2}^{n} - H_y\Big|_{i+1/2,j,k-1/2}^{n}}{\Delta z} \end{array} \right] \\ - \dfrac{H_y\Big|_{i+1/2,j,k+1/2}^{n} - H_y\Big|_{i+1/2,j,k-1/2}^{n}}{\kappa_{zk}\Delta z} \\ + \psi_{Ex,y}\Big|_{i+1/2,j,k}^{n} - \psi_{Ex,z}\Big|_{i+1/2,j,k}^{n} \end{array} \right). \quad (4)$$

Notice that the two identical difference terms in equation (4) have been added and subtracted.

Consider now, grouping the second two components and factoring out the difference term,

$$E_x\Big|_{i+1/2,j,k}^{n+1/2} = C_{ax}\Big|_{i+1/2,j,k} Ex\Big|_{i+1/2,j,k}^{n-1/2} + C_{bx}\Big|_{i+1/2,j,k} \left(\begin{array}{l} \dfrac{H_z\Big|_{i+1/2,j+1/2,k}^{n} - H_z\Big|_{i+1/2,j-1/2,k}^{n}}{\Delta y} + \\ \left[\dfrac{1}{\kappa_{yj}} - 1 \right] \dfrac{H_z\Big|_{i+1/2,j+1/2,k}^{n} - H_z\Big|_{i+1/2,j-1/2,k}^{n}}{\Delta y} \\ \dfrac{H_y\Big|_{i+1/2,j,k+1/2}^{n} - H_y\Big|_{i+1/2,j,k-1/2}^{n}}{\Delta z} \\ - \left[\dfrac{1}{\kappa_{zk}} - 1 \right] \dfrac{H_y\Big|_{i+1/2,j,k+1/2}^{n} - H_y\Big|_{i+1/2,j,k-1/2}^{n}}{\Delta z} \\ + \psi_{Ex,y}\Big|_{i+1/2,j,k}^{n} - \psi_{Ex,z}\Big|_{i+1/2,j,k}^{n} \end{array} \right). \quad (5)$$

If the κ components are 1.0 within the main solution space, the new terms disappear, yielding the standard Yee update equations. The new terms, then, can be added within the PML only. The finite difference update equation for the Ex component is then,

$$E_x\Big|_{i+1/2,j,k}^{n+1/2} = C_{ax}\Big|_{i+1/2,j,k} Ex\Big|_{i+1/2,j,k}^{n-1/2} + C_{bx}\Big|_{i+1/2,j,k} \left(\begin{array}{l} \dfrac{H_z\Big|_{i+1/2,j+1/2,k}^{n} - H_z\Big|_{i+1/2,j-1/2,k}^{n}}{\Delta y} - \\ \dfrac{H_y\Big|_{i+1/2,j,k+1/2}^{n} - H_y\Big|_{i+1/2,j,k-1/2}^{n}}{\Delta z} \end{array} \right). \quad (6)$$

This difference equation may now be calculated within the entire solution space, including the PML, in one loop. Within the PML, the ψ components are then added after computation of equation (4), along with the new difference terms, as follows,

$$E_{xPML}\Big|_{i+1/2,j,k}^{n+1/2} = E_x\Big|_{i+1/2,j,k}^{n+1/2} + C_{bx}\Big|_{i+1/2,j,k} \left(\begin{array}{l} \left[\dfrac{1-\kappa_{yj}}{\kappa_{yj}} \right] \dfrac{H_z\Big|_{i+1/2,j+1/2,k}^{n} - H_z\Big|_{i+1/2,j-1/2,k}^{n}}{\Delta y} \\ - \left[\dfrac{1-\kappa_{zk}}{\kappa_{zk}} \right] \dfrac{H_y\Big|_{i+1/2,j,k+1/2}^{n} - H_y\Big|_{i+1/2,j,k-1/2}^{n}}{\Delta z} \\ + \psi_{Ex,y}\Big|_{i+1/2,j,k}^{n} - \psi_{Ex,z}\Big|_{i+1/2,j,k}^{n} \end{array} \right). \quad (7)$$

This completes the modified formulation of the CPML. We can now assign a PEC wall around the entire solution space, then implement equation (6) everywhere, including the PML region. We then add the PML material in the regions required as described by equation (7).

Note that for this implementation, 2 additional add/subtracts and 1 additional multiplication must take place in equations (6) and (7) as compared to equation (3). One additional "if then" is saved per field or cell, depending on the implementation.

Michael Wong received the B.Sc. degree in Electrical Engineering from Queen's University in Kingston, Ontario, in 1997, and the M.Sc. degree in Electrical Engineering from Concordia University in Montreal, Quebec in 2006. He is currently a Ph.D. candidate at Concordia University in Montreal, Quebec. From 1998 to 2004 he was with TMI Communications (later Mobile Satellite Ventures) working on software, RF Engineering, licensing, and regulatory requirements all related to satellite communications and mobile satellite telephony. His current research focuses on electromagnetic band gap structures for antenna and microwave device applications, stripline and microstrip antennas, as well as the FDTD method.

Abdel-Razik Sebak received the B.Sc. degree (with honors) in Electrical Engineering from Cairo University, Egypt, in 1976 and the B.Sc. degree in Applied Mathematics from Ein Shams University, Egypt, in 1978. He received the M.Eng. and Ph.D. degrees from the University of Manitoba, Winnipeg, MB, Canada, in 1982 and 1984, respectively, both in electrical engineering. From 1984 to 1986, he was with the Canadian Marconi Company, Kanata, Ontario, working on the design of microstrip phased array antennas. From 1987 to 2002, he was a Professor in the Electrical and Computer Engineering Department, University of Manitoba, Winnipeg. He is currently a Professor of Electrical and Computer Engineering, Concordia University, Montreal. His current research interests include phased array antennas, computational electromagnetics, integrated antennas, electromagnetic theory, interaction of EM waves with new materials and bio-electromagnetics. Dr. Sebak received the 2003-2004 Faculty of Engineering, Concordia University double Merit Award for outstanding Teaching and Research. He has also received the 2000 and 1992 University of Manitoba Merit Award for outstanding Teaching and Research, the 1994 Rh Award for Outstanding Contributions to Scholarship and Research in the Applied Sciences category, and the 1996 Faculty of Engineering Superior Academic Performance. Dr. Sebak has served as Chair for the IEEE Canada Awards and Recognition Committee (2002-2004) and IEEE Canada CONAC (1999-2001). He has also served as Chair of the IEEE Winnipeg Section (1996-97). He is the Technical Program Co-Chair (2006) and served as the Treasurer (1992, 1996, and 2000) and Publicity Chair (1994) for the Symposium on Antenna Technology and Applied Electromagnetics (ANTEM). Dr. Sebak has also served as Chair (1991-92) of the joint IEEE AP/MTT/VT Winnipeg Chapter. He received, as the Chapter Chair, the 1992 IEEE Antennas and Propagation Society Best Chapter Award. He is a Senior Member of the IEEE, and a member of the International Union of Radio Science Commission B.

Effective Permittivity Scheme for ADI-FDTD Method at the Interface of Dispersive Media

[1]W. Fu and [2]E. L. Tan

[1] The University of Liverpool and Guidance Monitoring Ltd., the United Kingdom
E_mail: fuwe0001@ntu.edu.sg

[2] School of EEE, Nanyang Technological University, Singapore 639798

***Abstract* –** This paper presents an effective permittivity scheme to treat the dispersive media interfaces in ADI-FDTD method so as to avoid significant error due to improper assignment of media permittivity. In order to reduce the extra memory storage and computation operation required, a reduced-order modeling method is introduced to our scheme, which can simplify the programming work as well and therefore has a significant practical meaning. One numerical experiment will be performed to illustrate the procedure and effect of this effective permittivity scheme. The stability analysis of the updating equations will also be discussed.

***Keywords*:** ADI-FDTD, biological tissues, dispersive media, and material interfaces.

I. INTRODUCTION

For accurate modeling of material interfaces in the conventional finite difference time domain (FDTD) method [1], the effective permittivity scheme has been proposed for the interfaces of non dispersive media [2, 3] and dispersive media [4]. In this paper, the effective permittivity scheme is presented for the alternating-directional-implicit (ADI) FDTD method [5] at the interface of dispersive media. During recent years a lot of research works related to the ADI-FDTD method have been carried out due to its unconditional stability, which means the time step size of this method would not be constraint by the mesh size any more. For example, the three-dimensional ADI-FDTD method as well as its stability analysis was proposed in [6]. The higher order [7] and parameter-optimized ADI-FDTD methods [8, 9] have also been developed. The discussion here is based on the ADI method for dispersive media in [10], where the treatment for the interface of dispersive media has not been mentioned. This scheme is also applicable to the cases of non dispersive-non dispersive and dispersive-non dispersive media interfaces. To the best of our knowledge, the treatment of media interfaces in ADI-FDTD method has not been discussed in the literature.

In the next section, the formulas for the effective permittivity scheme are provided. Section III performs one numerical experiment to illustrate the procedure and effect of our proposed scheme. This experiment is about the wave propagation in different biological tissues and the reflection coefficient at the interface of muscle and bone is evaluated, which are both Debye dispersive media. To reduce the extra memory storage and computation operation required, a reduced-order modeling method for discrete system will be applied to deal with the effective permittivity at the interface of two neighboring dispersive media, which can also simplify the programming work and therefore has a significant practical advantage. It can be seen that this scheme can avoid the significant error due to improper assignment of media permittivity. Thus it is meaningful to investigate the treatment of media interface in ADI-FDTD method since it will be useful for many practical problems, such as the one about bio-electromagnetics discussed here. The stability analysis of the updating equations of this scheme is discussed in Section IV, which provides the approach to investigate the stability based on the reduced-order model of the permittivity obtained.

II. FORMULATION

Following [10], we consider the case of two-dimensional (2-D) TE wave propagation in dispersive media. The permittivity $\varepsilon(\omega)$ is related to the frequency ω and the permeability μ. is assumed to be constant. Therefore we will focus the discussion on solving Maxwell's equation from Ampere's law, whose integral form is represented as,

$$\frac{\partial}{\partial t}\iint_S D \cdot dS = \oint_C H \cdot dl \,. \tag{1}$$

The electric flux density D can be related to the electric field intensity E in s domain by,

$$D(s) = \varepsilon(s)E(s) \,. \tag{2}$$

According to the second order temporal approximation of equation (1), it can be obtained that,

$$\frac{\iint_S D^{n+1}\cdot dS-\iint_S D^{n}\cdot dS}{\Delta t} = \frac{\oint_C H^{n+1}\cdot dl+\oint_C H^{n}\cdot dl}{2}+O\left(\Delta t^2\right). \tag{3}$$

Here Δt is the time step size and n is the temporal index. The D and E in discrete time domain can be related in z domain by,

$$D(z)=\varepsilon(z)E(z)\,. \tag{4}$$

Equation (4) can be derived from equation (2) by substituting,

$$s=\frac{4}{\Delta t}\frac{1-z^{-1/2}}{1+z^{-1/2}}. \tag{5}$$

Henceforth, all the poles, zeros and orders of the representation for the media permittivity in z domain are in relation to the term $z^{-1/2}$, because each field component is marching one half time step for each update sub-procedure.

Considering the field components arrangement in Fig. 1 and splitting equation (3) into two sub-procedures in discrete spatial domain, we can obtain the equations in equation (6) for the treatment of the interface of two different dispersive media in ADI-FDTD method.

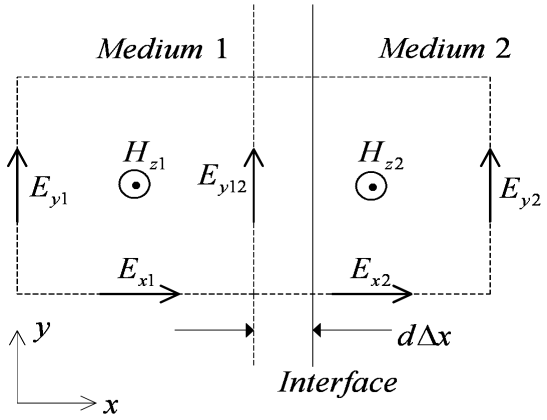

Fig. 1. TE wave field components arrangement at the interface.

$$\frac{D_{y12}{}^{n+1/2}-D_{y12}{}^{n}}{\Delta t/2}=-\frac{H_{z2}{}^{n+1/2}-H_{z1}{}^{n+1/2}}{\Delta x}, \tag{6a}$$

$$\frac{D_{y12}{}^{n+1}-D_{y12}{}^{n+1/2}}{\Delta t/2}=-\frac{H_{z2}{}^{n+1/2}-H_{z1}{}^{n+1/2}}{\Delta x} \tag{6b}$$

where Δx is the mesh size in x direction, $d\Delta x$ ($-0.5 \le d \le 0.5$) is the displacement of the media interface relative to the nearest parallel FDTD mesh edge, and the subscripts *1* and *2* denote the field components in media *1* and *2*, respectively. D_{y12} can be related to the electric field component E_{y12} at the mesh edge by the effective permittivity scheme as,

$$\begin{aligned} D_{y12}(z) &= (\frac{1}{2}+d)D_1(z)+(\frac{1}{2}-d)D_2(z) \\ &= (\frac{1}{2}+d)\varepsilon_1(z)E_{12}(z)+(\frac{1}{2}-d)\varepsilon_2(z)E_{12}(z). \end{aligned} \tag{7}$$

In practice, the mesh edge is usually set to overlap with the interface of different media. So here we mainly consider this case, where d = 0 and we obtain,

$$D_{y12}(z)=\frac{\varepsilon_1(z)+\varepsilon_2(z)}{2}E_{y12}(z)=\varepsilon_{12}(z)E_{y12}(z)\,. \tag{8}$$

Based on equations (6) and (8), the update equations for the interface of dispersive media can be derived as in [10]. The symbols $\varepsilon_1(z)$ and $\varepsilon_2(z)$ are the permittivity of these two neighboring media in z domain. The $\varepsilon_{12}(z)$ is the effective permittivity at the material interface and is related to the sum of $\varepsilon_1(z)$ and $\varepsilon_2(z)$. One can find that the number of the poles of $\varepsilon_{12}(z)$ is increased when the poles of $\varepsilon_1(z)$ and $\varepsilon_2(z)$ are different, which is in accordance with the statement in [4]. Since the order of the numerator and denominator of the representation for the effective permittivity will grow with the increase of the number of poles, extra memory storage and computation operation will be required. In order to reduce the extra memory storage and computation operation, here we introduce a reduced-order modeling method of discrete system [11] to deal with the effective permittivity. Through this method, the order of both the numerator and denominator of the effective permittivity in z domain can be reduced. We can select the order of the reduced-order model to be no higher than the maximum order of either neighboring media. The whole procedure of the simulation can be summarized as:

1) Determine the conditions of the simulation, such as mesh size, time step, boundary condition, and properties of media.
2) Derive the representation of each medium permittivity in z domain.
3) Derive the relation between D and E in the z domain at the interface of different media.
4) Apply the reduced-order modeling method to achieve the reduced-order model of the effective permittivity at the interface if there are different poles of the permittivity for the neighboring media.
5) Obtain the update equations in a similar way as in [10] and run simulation.

When one or both of neighboring media are replaced by non dispersive media permittivity, equation (8) will represent the effective scheme for interfaces of dispersive-non dispersive and non dispersive-non dispersive media, respectively, where the permittivity of the non dispersive media is a constant and in a simpler form compared with that of dispersive media. In the next section, numerical experiment will be performed to illustrate the procedure and effect of our scheme for the case of dispersive-dispersive media interface.

III. NUMERICAL EXPERIMENT

To show the procedure and benefit of this effective permittivity scheme for ADI-FDTD method at the interface of dispersive media, let us assume a Gaussian pulse propagating normally through the interface of the muscle (assumed to be medium *1*) and bone (assumed to be medium *2*), and study the reflection coefficient at this interface, which is parallel to *y* axis. The continuous function of the pulse is $g(t)=100\exp\left(-\left((t-320\Delta t)/64\Delta t\right)^2\right)$, where Δt = 10ps is the simulation time step. The uniform mesh size is set to be 0.5 mm and the thickness of both tissues is assumed to be 1 cm. The structure to be analyzed is truncated by 10-cell PML.

To start the illustration for the procedure of the effective permittivity scheme, the parameters of the Debye equation for the muscle and bone are obtained from [12] and [13], respectively. The Debye equation of relative permittivity can be presented in *s* domain as,

$$\varepsilon_r(s)=\varepsilon_\infty+\frac{A_1}{1+s\tau_1}+\frac{A_2}{1+s\tau_2}. \tag{9}$$

For the relative permittivity $\varepsilon_{msl}(s)$ of muscle, ε_∞=19, A_1=10000, τ_1=1.13×10^{-7}s, A_2=42, and τ_2=1.19×10^{-11}s. For the relative permittivity $\varepsilon_{bon}(s)$ of bone, ε_∞=3.4, A_1=309.4, τ_1=4.625×10^{-8}s, A_2=3.71, and τ_2=9.07×10^{-11}s. Their representations in *z* domain, $\varepsilon_1(z)$ and $\varepsilon_2(z)$, can be derived by the bi-linear transform in equation (5),

$$\begin{aligned}\varepsilon_1(z)&=\varepsilon_{msl}(s)\Big|_{s=\frac{4}{\Delta t}\frac{1-z^{-1/2}}{1+z^{-1/2}}}\\&=\frac{26.512901-31.324797z^{-1/2}+4.966468z^{-1}}{1-1.652734z^{-1/2}+0.652749z^{-1}},\end{aligned} \tag{10}$$

$$\begin{aligned}\varepsilon_2(z)&=\varepsilon_{bon}(s)\Big|_{s=\frac{4}{\Delta t}\frac{1-z^{-1/2}}{1+z^{-1/2}}}\\&=\frac{3.516241-6.616321z^{-1/2}+3.101916z^{-1}}{1-1.946244z^{-1/2}+0.946250z^{-1}}.\end{aligned} \tag{11}$$

Here all the numbers are kept to six digits after the decimal part in order to distinguish them. It should be noted that in this section we only talk about the process of the relative permittivity for simplicity, and the final permittivity in the updating equation should be the relative permittivity obtained times the vacuum permittivity ε_0.

According to equation (9), the effective permittivity at the material interface can be achieved. One can find that the poles of the muscle permittivity in *z* domain are 0.999955 and 0.652778, and those of the bone permittivity are 0.999892 and 0.946352. Therefore the effective permittivity will possess four different poles and zeros, rather than two poles and zeros like the permittivity of each neighboring medium. So the field components *D* and *E* at two extra time steps need to be saved and processed. When the reduced-order modeling method is applied to reduce the order of the effective permittivity, a discrete model for the effective permittivity at the interface can be deduced, which possesses the same number of poles and zeros as these two media. Therefore the memory and computation operation for the extra field components of two time steps are not needed any more. Here if we assume that the number of the nodes on the interface is N_d and the memory occupied by each field component value is N_m bytes, the scheme adopting reduced-order modeling at least can save $4N_dN_m$ bytes memory and the computation operation on the extra field components is also eliminated. In addition, this reduced-order modeling process simplifies the programming work, which has a significant practical advantage.

If $z^{1/2}$ in equations (10) and (11) is replaced by $z^{1/2}=\exp(j\omega\Delta t/2)=\exp(j\theta)$, where ω is the frequency we are interested in and Δt is the time step size of the FDTD scheme, the system response before the reduced-order modeling can be obtained from equation (8). Since the reduce-order model of the permittivity at the interface is supposed to possess two poles and zeros as the two neighboring media, let us substitute $z^{1/2}=\exp(j\theta)$ into the reduced-order model of equation (12),

$$\varepsilon_{12}(z)=\frac{p_0+p_1z^{-1/2}+p_2z^{-1}}{q_0+q_1z^{-1/2}+q_2z^{-1}}=\frac{p_0z+p_1z^{1/2}+p_2}{q_0z+q_1z^{1/2}+q_2} \tag{12}$$

where p_0, p_1, p_2, q_0, q_1, and q_2 are the parameters to be achieved in this reduced-order model. Based on the model in equation (12) and the system response from equation (8) mentioned above, an equation similar to the equation (8) in [11] can be achieved and the reduced-order modeling can be carried out accordingly [11]. The result of the reduced-order model of the effective permittivity in *z* domain reads,

$$\varepsilon_{12}(z)=\frac{24.397910\text{-}44.359457z^{-1/2}+19.991045z^{-1}}{1\text{-}1.877082z^{-1/2}+0.877088z^{-1}}. \quad (13)$$

With all these permittivity representations in z domain, the relation between D and E in z domain everywhere in the computational domain can be derived, and then the update equations can be obtained in a similar way as in [10].

The magnitude and phase angle (in degree) of the reflection coefficients at various frequencies are evaluated by three different schemes, which include the effective permittivity scheme, and the permittivity at the boundary simply assigned to either one of the two media. The numerical results are compared with the exact values in Figs. 2 and 3.

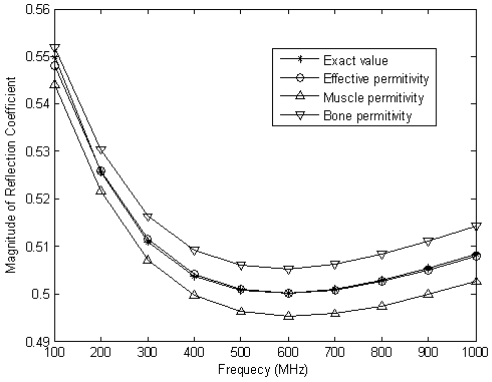

Fig. 2. Comparison of the magnitudes of reflection coefficients.

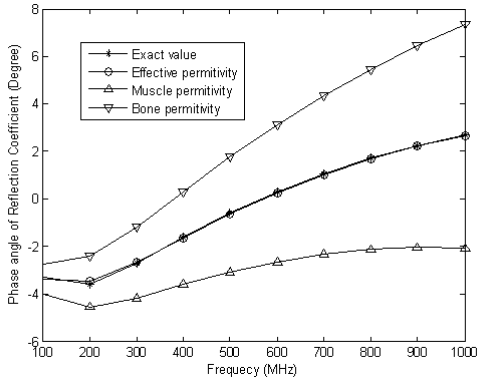

Fig. 3. Comparison of the phase angles of reflection coefficients.

From these two figures, one can find that the results of the effective permittivity scheme agree with the exact values very well, however, the results of the other two cases obviously disagree with the exact value. In order to highlight the difference between the numerical results and exact value, *ErrordB* in equation (14) defines the error of the numerical results in decibel for each sampling point,

$$ErrordB(f_m)=20\log\left(\frac{\left|F(f_m)-F_0(f_m)\right|}{\left|F_0(f_m)\right|}\right). \quad (14)$$

$F(f_m)$ is the numerical result at the m-th frequency sampling point f_m while $F_0(f_m)$ is the corresponding exact value.

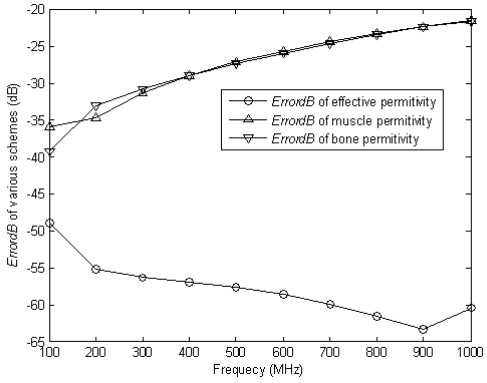

Fig. 4. Comparison of Error (dB) of various schemes.

Figure 4 plots *ErrordB* of the three schemes mentioned above and it can be found that this effective permittivity scheme in ADI-FDTD successfully avoids the significant error due to improper assignment of media permittivity.

IV. STABILITY ANALYSIS

In order to analyze the stability of the updating equations for the ADI-FDTD method at the interface of dispersive media discussed in the previous section by the von Neumann method [14], the trial solutions of the field components in the form of equation (15) are substituted into the updating equations,

$$V\big|_{I,J}^{n}=V^{n}e^{-j(k_xI\Delta x+k_yJ\Delta y)} \quad (15)$$

where V represents various field components, I and J are the spatial indexes. Then the updating equations can be written in a matrix form as,

$$\mathbf{M}_{1\mathrm{L}}\vec{u}^{\,n+1/2}=\mathbf{M}_{1\mathrm{R}}\vec{u}^{\,n}, \quad (16a)$$

$$\mathbf{M}_{2\mathrm{L}}\vec{u}^{\,n+1}=\mathbf{M}_{2\mathrm{R}}\vec{u}^{\,n+1/2} \quad (16b)$$

where

$$\vec{u}^{\,n}=\left[\widetilde{D}_x^{n}\quad E_x^{n}\quad \widetilde{D}_x^{n-1/2}\quad E_x^{n-1/2}\quad \widetilde{D}_y^{n}\quad E_y^{n}\quad \widetilde{D}_x^{n-1/2}\quad E_x^{n-1/2}\quad H_z^{n}\right]^{T},$$

$$\mathbf{M}_{1\mathrm{L}}=\begin{bmatrix} 1 & 0 & 0 & 0 & 0 & 0 & 0 & 0 & 0 \\ -q_0 & p_0 & 0 & 0 & 0 & 0 & 0 & 0 & 0 \\ 0 & 0 & 1 & 0 & 0 & 0 & 0 & 0 & 0 \\ 0 & 0 & 0 & 1 & 0 & 0 & 0 & 0 & 0 \\ 0 & 0 & 0 & 0 & 1 & 0 & 0 & 0 & jbP_x \\ 0 & 0 & 0 & 0 & -q_0 & p_0 & 0 & 0 & 0 \\ 0 & 0 & 0 & 0 & 0 & 0 & 1 & 0 & 0 \\ 0 & 0 & 0 & 0 & 0 & 0 & 0 & 1 & 0 \\ 0 & 0 & 0 & 0 & 0 & jdP_x & 0 & 0 & 1 \end{bmatrix},$$

$$\mathbf{M}_{1\mathrm{R}}=\begin{bmatrix} 1 & 0 & 0 & 0 & 0 & 0 & 0 & 0 & jbP_y \\ q_1 & -p_1 & q_2 & -p_2 & 0 & 0 & 0 & 0 & 0 \\ 1 & 0 & 0 & 0 & 0 & 0 & 0 & 0 & 0 \\ 0 & 1 & 0 & 0 & 0 & 0 & 0 & 0 & 0 \\ 0 & 0 & 0 & 0 & 1 & 0 & 0 & 0 & 0 \\ 0 & 0 & 0 & 0 & q_1 & -p_1 & q_2 & -p_2 & 0 \\ 0 & 0 & 0 & 0 & 1 & 0 & 0 & 0 & 0 \\ 0 & 0 & 0 & 0 & 0 & 1 & 0 & 0 & 0 \\ 0 & jdP_y & 0 & 0 & 0 & 0 & 0 & 0 & 1 \end{bmatrix},$$

$$\mathbf{M}_{2\mathrm{L}}=\begin{bmatrix} 1 & 0 & 0 & 0 & 0 & 0 & 0 & 0 & -jbP_y \\ -q_0 & p_0 & 0 & 0 & 0 & 0 & 0 & 0 & 0 \\ 0 & 0 & 1 & 0 & 0 & 0 & 0 & 0 & 0 \\ 0 & 0 & 0 & 1 & 0 & 0 & 0 & 0 & 0 \\ 0 & 0 & 0 & 0 & 1 & 0 & 0 & 0 & 0 \\ 0 & 0 & 0 & 0 & -q_0 & p_0 & 0 & 0 & 0 \\ 0 & 0 & 0 & 0 & 0 & 0 & 1 & 0 & 0 \\ 0 & 0 & 0 & 0 & 0 & 0 & 0 & 1 & 0 \\ 0 & -jdP_y & 0 & 0 & 0 & 0 & 0 & 0 & 1 \end{bmatrix},$$

$$\mathbf{M}_{2\mathrm{R}}=\begin{bmatrix} 1 & 0 & 0 & 0 & 0 & 0 & 0 & 0 & 0 \\ q_1 & -p_1 & q_2 & -p_2 & 0 & 0 & 0 & 0 & 0 \\ 1 & 0 & 0 & 0 & 0 & 0 & 0 & 0 & 0 \\ 0 & 1 & 0 & 0 & 0 & 0 & 0 & 0 & 0 \\ 0 & 0 & 0 & 0 & 1 & 0 & 0 & 0 & -jbP_x \\ 0 & 0 & 0 & 0 & q_1 & -p_1 & q_2 & -p_2 & 0 \\ 0 & 0 & 0 & 0 & 1 & 0 & 0 & 0 & 0 \\ 0 & 0 & 0 & 0 & 0 & 1 & 0 & 0 & 0 \\ 0 & 0 & 0 & 0 & 0 & -jdP_x & 0 & 0 & 1 \end{bmatrix},$$

$$b=\frac{\Delta t}{2\varepsilon_0},\ d=\frac{\Delta t}{2\mu},\ P_\xi=-\frac{2\sin\left(k_\xi\Delta\xi/2\right)}{\Delta\xi}$$

where $\widetilde{D}_\xi=\varepsilon_r E_\xi$ and ξ can be x or y.

According to the von Neumann method, the magnitudes of all the eigenvalues of the updating matrix **M** in equation (17) need to be no greater than 1 to make sure the updating equations to be stable, as shown

$$\vec{u}^{n+1}=\mathbf{M}\vec{u}^{n}=\left(\mathbf{M}_{2\mathrm{L}}\right)^{-1}\mathbf{M}_{2\mathrm{R}}\left(\mathbf{M}_{1\mathrm{L}}\right)^{-1}\mathbf{M}_{1\mathrm{R}}\vec{u}^{n}. \quad (17)$$

However, for the case of dispersive media, it is difficult to achieve the analytical solutions of the eigenvalues as in [6]. Therefore the combination of von Neumann method and Routh-Hurwitz criterion [15] is adopted here to investigate the stability. The reduced-order model of the dispersive media permittivity in equation (13) needs to be substituted into equation (17) to analyze the stability. If the bilinear transformation in equation (3) of [15] is applied to the eigenpolynomial of **M** and then the steps in [15] are followed to build the Routh table, it can be found that all the entries of the first column of the Routh table are non-negative quantities regardless of the time step size, which means the updating equation is still unconditionally stable for this case. One can analyze the stability of the updating equations by this approach.

The detailed procedures and the result of the Routh table will not be presented here due to the limit of paper length since they are very lengthy. But it is not difficult to work it out with the help of some mathematical software such as Matlab.

V. CONCLUSION

This paper has presented an effective permittivity scheme to treat the dispersive media interfaces in ADI-FDTD method. The approach to analyze its stability has been discussed as well. This scheme is also applicable to the cases of the dispersive and non dispersive media interfaces. To reduce the extra memory storage and computation operation generally required, a reduced-order modeling method for discrete system is applied to deal with the effective permittivity at the interface of two neighboring dispersive media, which can also simplify the programming work and therefore has a significant practical advantage. The numerical experiment, which is about wave propagation in different biological tissues for the demonstration of the case of dispersive-dispersive media interfaces, has been performed to illustrate the procedure and effect of our scheme. One can find that this scheme works well for avoiding the significant error due to improper assignment of media permittivity, as well as reducing the extra memory storage and computation operation required. Meanwhile the programming work is simplified. So the investigation on the treatment of media interfaces in ADI-FDTD method is meaningful since it will be useful for many practical problems.

REFERENCES

[1] K. S. Yee, “Numerical solution of initial boundary value problem involving Maxwell’s equations in

isotropic media," *IEEE Trans. Antennas and Propagation*, vol. 14, no. 4, pp. 302-307, Apr. 1966.

[2] T. Hirono, Y. Shibata, W. W. Lui, S. Seki, and Y. Yoshikuni, "The second-order condition for the dielectric interface orthogonal to the Yee-Lattice axis in the FDTD scheme," *IEEE Microwave and Wireless Components Lett.*, vol. 10, no. 9, pp. 359-361, Sep. 2000.

[3] K.-P. Hwang and A. C. Cangellaris, "Effective permittivities for second-order accuracy FDTD equations at dielectric interfaces," *IEEE Microwave and Wireless Components Lett.*, vol. 11, no. 4, pp. 158-160, Apr. 2001.

[4] D. Popovic and M. Okoniewski, "Effective permittivity at the interface of dispersive dielectrics in FDTD", *IEEE Microwave and Wireless Components Lett.*, vol. 13, no. 7, pp. 265-267, July 2003.

[5] T. Namiki, "A new FDTD algorithm based on alternating direction implicit method," *IEEE Trans. Microwave Theory and Techniques*, vol. 47, no. 10, pp. 2003-2007, Oct. 1999.

[6] F. Zheng, Z Chen, and J. Zhang, "Toward the development of a Three-Dimensional Unconditionally stable finite-difference time-domain method," *IEEE Trans. Microwave Theory Techniques*, vol. 48, no. 9, pp. 1550-1558, Sep. 2000.

[7] J. Chen, Z. Wang, and Y. Chen, "Higher-order alternative direction implicit FDTD method," *Electronics Lett.*, vol. 38, no. 22, pp. 1321-1322, Oct. 2002.

[8] M. Wang, Z. Wang, and J. Chen, "A parameter optimized ADI-FDTD method," *IEEE Antennas Wireless Propagation Lett.*, vol. 2, no. 1, pp. 118-121, 2003.

[9] W. Fu and E. L. Tan, "A parameter optimized ADI-FDTD method based on the (2,4) stencil," *IEEE Trans. Antennas and Propagation*, vol. 54, no. 6, pp. 1836-1842, June 2006.

[10] X. T. Dong, N. V. Venkatarayalu, B. Guo, W. Y. Yin, and Y. B. Gan, "General formulation of unconditionally stable ADI-FDTD method in linear dispersive media," *IEEE Trans. Microwave Theory and Techniques*, vol. 52, no. 1, pp. 170-174, Jan. 2004.

[11] S. Pan and L. J. Pal, "Reduced-order modeling of discrete-time system," *Applied Mathematical Modeling*, vol. 19, no. 3, pp. 133-138, Mar. 1995.

[12] O. P. Gandhi, B.-Q. Gao, and J.-Y. Chen, "A frequency-dependent finite-difference time-domain formulation for general dispersive media," *IEEE Trans. Microwave Theory and Techniques*, vol. 41, no. 4, pp. 658-665, Apr. 1993.

[13] O. P. Gandhi and C. M. Furse, "Currents induced in the human body for exposure to ultrawideband electromagnetic pulse," *IEEE Trans. Electromagnetic compatibility*, vol. 39, no. 2, pp. 174-180, May 1997.

[14] J. D. Hoffman, *Numerical methods for engineers and scientists*, McGraw-Hill, Inc, 1993.

[15] A. Pereda, L. A. Vielva, A. Vegas, and A. Prieto, "Analyzing the stability of the FDTD technique by combining the von Neumann method with the Routh-Hurwitz criterion," *IEEE Trans. Microwave Theory and Techniques*, vol. 49, no. 2, pp. 377-381, Feb. 2001.

Weiming Fu received the B. Eng. and M. Eng. degrees in information & communication engineering from Xi'an Jiaotong University (XJTU), Xi'an, China, in 2000 and 2003, respectively. In 2007, he received the Ph.D. degree from Nanyang Technological University (NTU), Singapore. From Sep. 2006 to Sep 2007, he was a Research Associate with Positioning and Wireless Technology Centre (PWTC), NTU. Currently he is a KTP Associate with the University of Liverpool and Guidance Monitoring Ltd. His research interests include computational electromagnetics, global simulation of RF circuit and EM structure, RF/microwave circuit design.

Eng Leong Tan received the B. Eng. degree with first class honors from the University of Malaya, Malaysia, and the Ph.D. degree from Nanyang Technological University, Singapore. In 1991-1992, he was a Research Assistant at University of Malaya, Malaysia. In 1991-1994, he worked part time at Commercial Network Corporations Sdn.Bhd., Malaysia. In 1999-2002, he was a Member of Technical Staff at Institute for Infocomm Research, Singapore. Since 2002, he is an Assistant Professor at the School of Electrical & Electronic Engineering, Nanyang Technological University, Singapore. His research interests include electromagnetic and acoustic simulations, RF and microwave circuit design.

New Physical Discrete UHF Multilayer Propagation Model for Urban Areas

[1]S. S. Seker and [1,2]G. Apaydin

[1] Department of Electrical and Electronic Engineering,
Bogazici University, 34340, Istanbul, Turkey, email: seker@boun.edu.tr

[2] Applied Research and Development, University of Technology Zurich,
Technoparkstrasse 1, 8005, Zurich, Switzerland, e-mail: gapaydin@hsz-t.ch

Abstract **–** In this paper, a newly developed discrete multilayer propagation model using scattering theory is studied using rectangular lossy multilayer dielectric plates which model the walls, the streets, and avenues in urban areas. The model is presented to study radio wave propagation in street environments and to compare it with previous theoretical and experimental studies. Good agreements are found. Using the developed model, it is possible to calculate the contributions of direct and scattered wave separately. The simulations reveal that the developed model can be applicable for a broad band of frequencies. This model can be used effectively for prediction of loss characteristics in a situation when two antennas are located below the rooftops in conditions of direct visibility.

Keywords*:* Discrete model, path loss, urban areas, scattering, and multilayer propagation model.

I. INTRODUCTION

There are many propagation models of Electromagnetic (EM) waves propagating in various kinds of building structures with differing shapes. The field of modeling has been extensively studied over the last decade. The models are important for designers of urban wireless communication links, namely for a precise prediction of link budget and radio coverage of areas of services. For each kind of planar building structures, different mathematical models have been proposed and good approximations have been done by successful studies. The evaluation of "Multislit Street Waveguide Model" [1-2] is introduced to describe the propagation characteristics along straight rectangular streets in cases where all antennas, the receiver, and the transmitter are placed in direct visibility (Line Of Sight conditions) at lower than rooftop level. In the same study [1], the conditions of regular terrain are considered further in the obstructive conditions (No Line Of Sight) for antennas, and they are described in the case of urban environments with a rectangular crossing street plan for different positions of both antennas relative to the rooftops. Furthermore, "Crossing Waveguides Model" [1-2] and the "Two Dimensional Multi diffraction Model" [3] are presented to describe the propagation characteristics and the coverage effects. The frequency characteristics and propagation attenuation constant in straight open-groove structures are presented in [4]. Ray tracing technique is explained in [3-5]. Ray Theory and Uniform Theory of Diffraction (UTD) are used to predict wave strength. In [6], modeling and measurements of EM-wave propagation in the Berlin Subway is presented.

As it has been mentioned in [1], the path loss in a residential environment depends on the dielectric properties of structures. All of the studies in literature assume that the walls are planar. However, this is not the case in the real world.

The developed propagation model based on the scattering formulation for the streets, ground, and walls in urban areas, has been introduced consisting of rectangular lossy multilayer dielectric plates for EM-waves. The novelty in this paper is the usage of "Discretized approach for scattering field" from irregular or arbitrary dielectric surfaces, where no exact solution is available.

In section II, the discretized approach for scattering field is illustrated. In sections III and IV, verification of the method is acquired using the results from literature for the radar cross section (RCS) of tunnel. Development of model for urban areas and simulations are done in section V and VI. In conclusions, we present the advantages of the model compared to the earlier model of propagation.

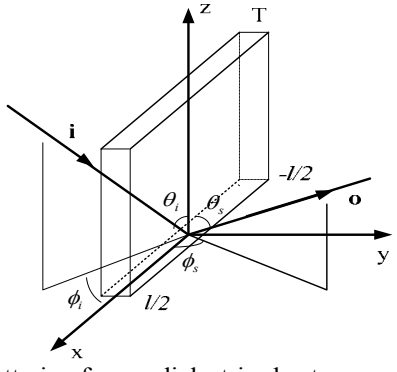

Fig. 1. Scattering from a dielectric sheet.

II. THE DISCRETIZED APPROACH FOR SCATTERING FIELD

The developed model is based on the determination of scattering amplitudes and scattering fields, introduced in [7] using scattering theory. The suggested method, which relies on the discretization approach, is valid only when curved surface is big compared to thickness in one direction. Firstly, the surface or shape is divided into multilayer rectangular plates. The scattering amplitudes and fields caused by each individual plate are calculated. Afterwards the contribution of each plate in the arbitrary shape is summed in an integral form to determine the scattering amplitudes for the whole surface or shape.

Consider an incident plane electromagnetic wave at an arbitrary dielectric surface representing multilayer plate seen in Fig. 1. The plane wave is assumed to have polarization (**p**) and to be propagating in the **i** direction,

$$\mathbf{E}_{\mathbf{i}}(\mathbf{r}) = \mathbf{p}\, E_0\, e^{jk_0 \mathbf{i}\cdot\mathbf{r}} \tag{1}$$

where E_0 is the magnitude of the incident wave, **r** is the general position vector, $k_0 = \omega\sqrt{\mu_0\varepsilon_0}$ is the free space wave number and the direction of incident wave is

$$-\mathbf{i} = \sin\theta_i\left(\cos\phi_i\hat{x} + \sin\phi_i\hat{y}\right) + \cos\theta_i\hat{z}\,. \tag{2}$$

In equation (2), the spherical angles of the incident wave (θ_i and φ_i) are measured with respect to polar axes z and x, respectively. Incident waves with both horizontal ($\mathbf{p} = \mathbf{h_i}$) and vertical ($\mathbf{p} = \mathbf{v_i}$) polarizations are taken into consideration. The horizontal polarization is $\mathbf{h_i} = (\mathbf{i}\times\hat{z})/|\mathbf{i}\times\hat{z}|$. The vertical polarization is taken perpendicular to both **i** and $\mathbf{h_i}$, thus $\mathbf{v_i} = \mathbf{h_i}\times\mathbf{i}$.

The formal solution for the scattered fields ($\mathrm{E_s(o,i)} = \mathrm{f(o,i)}\, e^{jk_0 R}/R$ where R is the distance between scatterer and observation point) from the surface can be obtained in terms of the fields inside the scatterer using a standard procedure [8]. The integral form of scattering amplitude is ($f_{pq} = \mathbf{p}\cdot\mathbf{f}\cdot\mathbf{q}$, $\mathbf{p}\in\{\mathbf{h_i},\mathbf{v_i}\}$, $\mathbf{q}\in\{\mathbf{h_o},\mathbf{v_o}\}$),

$$\begin{aligned}\mathrm{f(o,i)} &= \frac{k_0^2}{4\pi}\int_{Vol}(\varepsilon_r(\mathbf{r}')-1)(\mathrm{I}-\mathrm{oo})\cdot\mathrm{E_{int}}(\mathbf{r}')\cdot e^{-jk_0\mathrm{o}\cdot\mathbf{r}'}d\mathbf{r}' \\ &= f_{hh}\,\mathrm{h_o h_i} + f_{vh}\,\mathrm{v_o h_i} + f_{hv}\,\mathrm{h_o v_i} + f_{vv}\,\mathrm{v_o v_i}\end{aligned} \tag{3}$$

where f_{hh}, f_{vh}, f_{hv}, and f_{vv} are the scattering amplitudes, **I** is a unit dyadic, **o** is a unit vector towards an observation point, and $\mathbf{E_{int}}$, which is not known in general, is the internal field inside the scatterer or object. The integration is carried out over the volume of the scatterer. In terms of the scattering angles θ_s and φ_s, **o** is written as

$$\mathbf{o} = \sin\theta_s\left(\cos\varphi_s\hat{x} + \sin\varphi_s\hat{y}\right) + \cos\theta_s\hat{z}\,. \tag{4}$$

In order to solve equation (3), it is necessary to know the fields inside the scatterer which is the dielectric surface of street, wall or ground for this study. It is characterized by constitutive parameters: permittivity ($\varepsilon_0\varepsilon_r$) and permeability ($\mu_0$) of the dielectric material. Next, we deal with the problem of finding the internal field of the surface.

The fields inside the rectangular plate sheet are the same as the ones that would exist in a multilayer dielectric slab of the same physical and geometrical properties. Thus the horizontal ($\mathbf{E^h}$) and vertical ($\mathbf{E^v}$) electric fields inside each layer can be expressed as,

$$\mathbf{E}_m^{\mathbf{h}} = A_m\, e^{-\gamma_m\cdot\mathbf{r}}\mathbf{q}_- + B_m\, e^{\gamma_m\cdot\mathbf{r}}\mathbf{q}_+, \quad \mathbf{q}\in\{\mathbf{h},\mathbf{v}\} \tag{5}$$

$$\mathbf{E}_m^{\mathbf{v}} = F_m\, e^{-\gamma_m\cdot\mathbf{r}}\mathbf{q}_- + G_m\, e^{\gamma_m\cdot\mathbf{r}}\mathbf{q}_+, \quad \mathbf{q}\in\{\mathbf{h},\mathbf{v}\}, \tag{6}$$

where γ_m is the propagation constant in the m^{th} layer and A_m, B_m, F_m, G_m are coefficients of the plane wave for horizontal and vertical electric fields. An electromagnetic wave of any kind of polarization can be decomposed into its orthogonal linearly polarized components. The electric fields parallel to the interface are horizontally polarized and the fields perpendicular to the interface are vertically polarized.

Using boundary conditions, the coefficients for the horizontal and vertical polarized wave having an incident angle of each layer θ_m and layer position d_m upon a multilayer dielectric slab of n layers with a relative permittivity (ε_m), and the loss tangent ($\tan\delta_m$) are,

$$\begin{bmatrix}A_m\\ B_m\end{bmatrix} = \frac{1}{2}\begin{bmatrix}(1+Y_{m+1})e^{(\gamma_{m+1}-\gamma_m)d_m} & (1-Y_{m+1})e^{-(\gamma_{m+1}+\gamma_m)d_m}\\ (1-Y_{m+1})e^{(\gamma_m+\gamma_{m+1})d_m} & (1+Y_{m+1})e^{(\gamma_m-\gamma_{m+1})d_m}\end{bmatrix}\begin{bmatrix}A_{m+1}\\ B_{m+1}\end{bmatrix} \tag{7}$$

$$\begin{bmatrix}F_m\\ G_m\end{bmatrix} = \frac{1}{2}\begin{bmatrix}(1+W_{m+1})e^{(\gamma_{m+1}-\gamma_m)d_m} & (1-W_{m+1})e^{-(\gamma_{m+1}+\gamma_m)d_m}\\ (1-W_{m+1})e^{(\gamma_m+\gamma_{m+1})d_m} & (1+W_{m+1})e^{(\gamma_m-\gamma_{m+1})d_m}\end{bmatrix}\begin{bmatrix}F_{m+1}\\ G_{m+1}\end{bmatrix}, \tag{8}$$

where $Y_{m+1} = \dfrac{\cos\theta_{m+1}}{\cos\theta_m}\sqrt{\dfrac{\varepsilon_{m+1}(1-j\tan\delta_{m+1})}{\varepsilon_m(1-j\tan\delta_m)}}$, and

$W_{m+1} = \dfrac{\cos\theta_{m+1}}{\cos\theta_m}\sqrt{\dfrac{\varepsilon_m(1-j\tan\delta_m)}{\varepsilon_{m+1}(1-j\tan\delta_{m+1})}}$, respectively.

After substituting equations (5) and (6) into equation (3), and evaluating the integral, scattering amplitudes for horizontal and vertical polarization are obtained as,

$$f_{hh} = \sum_{m=1}^{n} \left[\frac{{k_0}^2 (\varepsilon_m - 1) S_m}{4\pi} \left(\begin{array}{l} A_m \dfrac{e^{d_m C_m} - e^{d_{m-1} C_m}}{C_m} \\ +B_m \dfrac{e^{-d_{m-1} D_m} - e^{-d_m D_m}}{D_m} \end{array} \right) \right] \quad (9)$$

$$f_{vv} = \frac{{k_0}^2}{4\pi} \left(K_1 \cos\theta_s - K_2 \sin\theta_s \right), \quad (10)$$

where

$$K_1 = \sum_{m=1}^{n} \left[\frac{k_{m-1} (\varepsilon_m - 1) S_m}{k_0 \varepsilon_m} \left(F_m \frac{e^{d_{m-1} C_m} - e^{d_m C_m}}{C_m} + G_m \frac{e^{-d_{m-1} D_m} - e^{-d_m D_m}}{D_m} \right) \right],$$

$$K_2 = \sin\theta_i \sum_{m=1}^{n} \left[\frac{(\varepsilon_m - 1) S_m}{\varepsilon_m} \left(F_m \frac{e^{d_m C_m} - e^{d_{m-1} C_m}}{C_m} + G_m \frac{e^{-d_{m-1} D_m} - e^{-d_m D_m}}{D_m} \right) \right],$$

$C_m = j(k_m + k_0 \cos\theta_s)$, $D_m = j(k_m - k_0 \cos\theta_s)$, $k_m = k_0 \sqrt{\varepsilon_m - \sin^2\theta_i}$, S_m is the shape function, θ_s is the scattered angle, and n is the number of layers. The shape function for rectangular cross section is obtained as,

$$S_m = X_0 \, Y_0 \, Sinc(k_0 \, X_o \sin\theta_m) \quad (11)$$

where X_0, Y_0 are the side lengths, and θ_m is the incident angle of each layer.

After determining the scattering amplitudes of multilayer rectangular plate, the scattering amplitude of an arbitrary dielectric surface is obtained as:

1. The arbitrary dielectric surface is divided into N small approximately rectangular strips, each of which has a center described by x_c, y_c, and z_c. For each strip, the normal vector ($\mathbf{n_c}$) is determined ($c = 1,2,....N$).
2. The scattering amplitudes of each sheet $\mathbf{f}^{(c)}(\mathbf{o},\mathbf{i})$ are determined by using the multilayer model.
3. Each scattering amplitude is added coherently in order to obtain scattering amplitude of the total surface as, $\mathbf{f(o,i)} = \sum_{c=1}^{N} \mathbf{f}^{(c)}(\mathbf{o},\mathbf{i}) e^{jk_0 \zeta \cdot \mathbf{r}_c}$ where $\boldsymbol{\zeta} = \mathbf{i} - \mathbf{o}$ with $\mathbf{r}_c$ being the position vector to the center of the c^{th} strip.

III. VERIFICATION OF THE METHOD USING A HOLLOW CYLINDRICAL SHELL

In view of the above development, the bi-static RCS of surface can be obtained in terms of the scattering amplitude as follows [8-10]

$$\sigma_{pq} = 4\pi \, | f_{pq}(\mathbf{o},\mathbf{i}) |^2 . \quad (12)$$

Notice from equations (9) and (10) that f_{pq} depends on the shape (S), and the dielectric properties of scatterer. Both functions depend on the orientation of the scatterer, but S generally varies much more rapidly than other functions in f_{pq}.

Using the developed method, the scattering amplitudes of circular hollow finite length discrete cylindrical shell with length l as seen in Fig. 2., are found as,

$$f_{pq} = \frac{{k_0}^2 T}{4\pi} \left\{ \begin{array}{l} \mathrm{p}\cdot\mathrm{q} \sum_{c=1}^{N} (\varepsilon_r - 1) e^{jk_0 \zeta \cdot \mathrm{r_c}} S_m^{(c)} \\ -\sum_{c=1}^{N} \dfrac{(\varepsilon_r - 1)^2}{\varepsilon_r} (\mathrm{p}\cdot\mathrm{n_c}) \, (\mathrm{n_c}\cdot\mathrm{q}) \, e^{jk_0 \zeta \cdot \mathrm{r_c}} S_m^{(c)} \end{array} \right\} \quad (13)$$

with $\boldsymbol{\zeta} \cdot \mathbf{r}_c = a\,\zeta_y + a(\zeta_y \cos\varphi + \zeta_z \sin\varphi)$, a is the inner radius of the cylinder, φ is the angle which is measured from x axis, and T is the thickness. Next converting the sum, equation (13) becomes,

$$f_{hh} = \frac{{k_0}^2 (\varepsilon_r - 1) T l}{4\pi} \left\{ h_{is} s_1 - \frac{\varepsilon_r - 1}{\varepsilon_r} (h_1 s_2 + h_2 s_3 + h_3 s_4) \right\} \quad (14)$$

$$f_{vv} = \frac{{k_0}^2 (\varepsilon_r - 1) T l}{4\pi} \left\{ v_{is} s_1 - \frac{\varepsilon_r - 1}{\varepsilon_r} (v_1 s_2 + v_2 s_3 + v_3 s_4) \right\} . \quad (15)$$

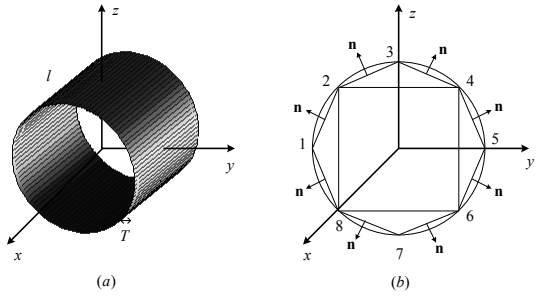

Fig. 2. (a) 3D Discretized cylinder shell and (b) exaggerated cross section.

The parameters, which appear in equations (14) and (15) are given in Appendix. Comparison of equations (14) and (15) with [10] shows very good agreement and summations in equations yield the Bessel function of the first kind as expected. This is the proof of discretization of the hollow finite length cylindrical shell. Equations (14) and (15) give the same RCS in [10] and in the limit of low frequencies as in [8].

We also verify our numerical result with the exact results of [11] by inverting their two dimensional results to three dimensional radar cross-sections (σ_{3D}) using the following formula [12],

$$\sigma_{3D} = \sigma_{2D} \frac{2l^2}{\lambda} \tag{16}$$

where λ is the wavelength and σ_{2D} is two dimensional RCS. In [11], the theoretical scattering solution for plane wave incident normally on a lossy dielectric multilayer circular cylinder of infinite length is outlined, and the two dimensional exact RCS are given as,

$$\sigma_{2D} = \frac{4}{k_0} |T_p(\varphi)|^2 \tag{17}$$

where

$$T_p(\varphi) = \sum_{n=0}^{\infty} e_n D_n^{(p)} \cos(n\varphi), \quad p \in \{h, v\}, \tag{18}$$

with $e_n = 1$ for $n = 0$, $e_n = 2$ for $n = 1, 2, \ldots$.

Next as a part of the study, the bi-static RCS of cylindrical surface with $\varepsilon_r = 29.1 - j13.3$, radius $a = 27.5$ cm, thickness $T = 0.2$ mm, length $l = 1$ m, and $f = 900$ MHz was computed by using equation (12). The results were compared with those obtained by using the exact solution (16) for verification [11]. Figures 3 and 4 clearly show that the solution obtained for cylinder by developed discretizing method approaches very closely to exact results for horizontal and vertical polarization.

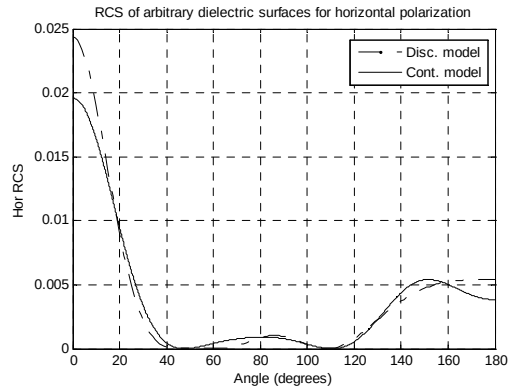

Fig. 3. RCS for horizontal polarization at 900MHz.

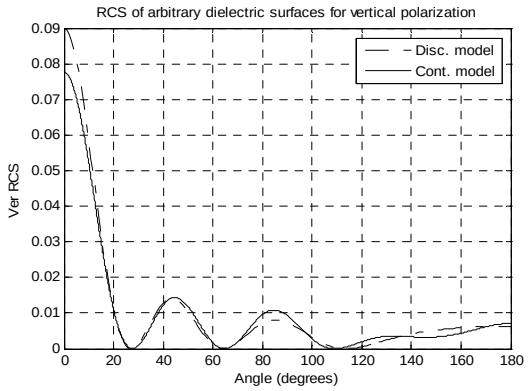

Fig. 4. RCS for vertical polarization at 900 MHz.

IV. SIMULATION RESULTS OF A TUNNEL

In this part, as a further proof of the method, attenuation in a tunnel was simulated by a cylindrical shell as seen in Fig. 2. We have run our simulation program and compared with the measurements, which were done in Berlin Subway system [6]. In our simulation, the tunnel cross section was modeled by a different cross sectional shapes. Statistical packet like spline routine provides necessary extra points for good accuracy. If the cross section is rectangular then all the strips in Fig. 2 taken between the points 8-2, 2-4, 4-6, and 6-8 are located along the line. If the cross section is open-grove then the normal vectors of strips along the points 2-4 are taken as a zero. The length of the configuration does not have to be constant; it can be variable as well. The building material was given to be dry concrete with $\varepsilon_r = 5 - j0.1$.

Figures 5 and 6 show the simulation results of our model. Figure 5 depicts the tunnel cross section as modeled by a circle with elevated floor. Figure 6 depicts rectangular cross section of width $w = 5.25$ m and height $h = 4.28$ m. The thickness of the wall is taken as 20 cm. Several different layers can be used in the simulation where necessary.

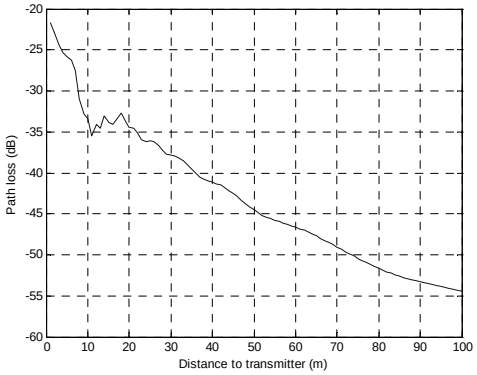

Fig. 5. The simulation results for f=1800MHz, $\varepsilon_r = 5 - j0.1$ arched cross-section.

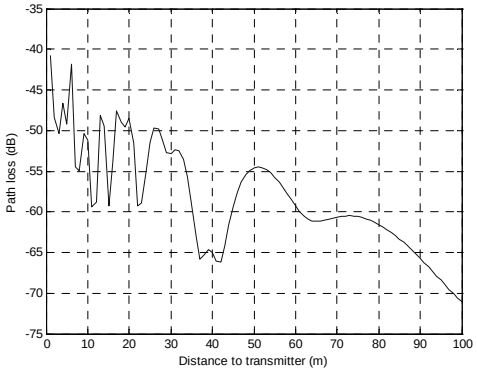

Fig. 6. The simulation results for f=1800MHz, $\varepsilon_r = 5 - j0.1$ rectangular cross-section.

The comparison between the results of discrete model with literature shows that the results of the simulation are indeed very close to measured values. The general shapes of the curves (considering the mean curve in figures) are exactly the same. They are both monotonically decreasing curves. They share the same range of values for attenuation.

Once again, depending on the ratio between the transverse dimensions of the tunnels and wavelength and on the distance from the transmitter, the attenuation values can be either greater or smaller than the attenuation in free-space. Curves in Figs. 5 and 6 clearly show this phenomenon.

In evaluating the results, it should also be noticed that the real world measurements involve many incident rays at different angles of interference simultaneously. The possible constructive and destructive interference between different plane waves is ignored. This also contributes to the differences between the measurement and simulation curves. The simulations reveal that the correct modeling parameter of the tunnel's cross-section influences the accuracy of the modeling results.

V. DEVELOPMENT OF MODEL FOR THE URBAN AREAS

In the real world, there are many objects, walls with windows and door, and gaps on the streets that contribute to the loss of electromagnetic wave at the receiver point. If we want to model buildings in the urban areas, we have to take into account these contributions to get reasonable results. Thus, actual discretization must be as seen in Fig. 7. In order to verify the model, windows, openings etc. are not taken into consideration in the following simulations.

Now, we will enhance our model to use it in urban areas, which have both side walls and slits (gaps between side walls). The walls and streets are modeled as a multilayer thin rectangular plate.

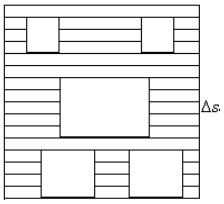

Fig. 7. The discretized wall of building.

As seen in Fig. 8, the total field density at the receiver is the sum of several rays, which are scattered from the inner side of walls (no windows) and smooth ground. But, our model can handle walls with windows and a door, and ground with holes or irregularities. Since the antennas' height is lower than the rooftop level the diffraction from the roof edges has been omitted.

Some of the parameters seen in the figure are h_i transmitter height, h_r receiver height, h_b average building height, l length of slits, and L length of sidewalls. Waves 1 and 3 can reach to the receiver antenna trough the wall and ground respectively. Wave 4 cannot reach to receiver and gets lost in the side streets.

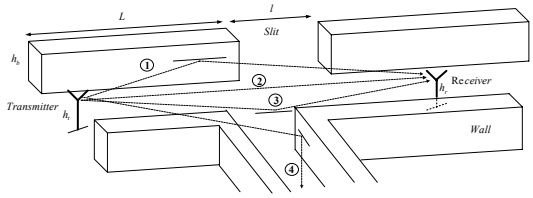

Fig. 8. 3D illustration of urban areas.

Only single scattering (first order) from the walls and ground is illustrated in the Fig. 8. However, we know that the second and third order scattering also contribute to the field density. Therefore, we have added these contributions to our calculation. After the third scattering, the loss of electric field increases so much that the contribution of this multiple scattered waves can be neglected.

As seen from the Fig. 8 some of the waves cannot reach to the receiver antenna as wave 4 does. Therefore, we have to choose the waves that can reach the antenna in order to find the total field. Scattering from the walls is taken into account by introducing the special brokenness parameter χ in terms of slit length of l_i and length of sidewalls L_i as presented in [1]

$$\chi = \frac{L_i}{L_i + l_i} \qquad (i = 1,2...) . \tag{19}$$

The magnitude of χ shows the density of the buildings and takes the value between 1 and 0 ($0 \leq \chi \geq 1$). If χ is "0", it means there is no side wall. The result must be equal to the loss of free space. If χ is "1", there are no slits or any gaps . As a result the following can be written,

$$\chi = \begin{cases} 1 \;\; \mathrm{AT} = \mathrm{Loss\ for\ no\ gap} \\ 0 \;\; \mathrm{AT} = \mathrm{Loss\ for\ no\ sidewall\,(free\ space)} \end{cases} \tag{20}$$

where AT is the total attenuation at receiver antenna.

In the developed software we moved the receiver antenna along the street and computed average total electric field for certain distances from the transmitter for both broken and unbroken models. Then, we calculated the path loss along the street for the LOS conditions as seen in Table 1. Finally, we developed the following field attenuation equation,

$$\mathrm{AT} = \mathrm{AT}_{\mathrm{unbrk}} + (\mathrm{AT}_{\mathrm{open}} - \mathrm{AT}_{\mathrm{unbrk}}) \times (1 - \chi) \tag{21}$$

where AT_{unbrk} represents attenuation at no gap, and AT_{open} represents free space attenuation. We have chosen the parameter χ according to the density of the buildings in the referenced surveys.

Next, we will present the some simulation results, which was done using the parameters from the literature such as street width, brokenness parameter, dielectric properties of the buildings etc.

VI. SIMULATION OF WAVE PROPAGATION FOR THE URBAN AREAS

We have run our software for the study of Open-Groove Structures for verification as seen in Fig. 9. Following parameters have been used for the simulation: f = 2GHz, ε_r = 4.18, σ = 0.026 *S/m* as stated in [4]. These dimensions have also been divided into small sheets as depicted in Fig. 7, in order to find the scattering amplitudes of each strip and total electric fields.

We obtained separate solutions for the vertical and horizontal field density in Fig. 10. Horizontal scale represents distance from the source in meter. We can see from the figures that the path loss is increasing with increasing distance. The path loss for horizontal polarization is more than the one for vertical polarization.

The second simulation has been done for the experimental data presented in [13] for conditions of direct visibility along streets in Manhattan, New York. We used the same parameters of measurement as presented in [13] such as $h_b = 50$ m for average building heights, $f = 900$ MHz for the operating frequency, $a = 30$ m for the street width, $\varepsilon_r = 15$, $\sigma = 7$ for dielectric properties of the sidewalls, and χ=0.8. The output of the simulation is illustrated in Fig. 11.

The graph reveals that the output highly depends on the shape of the streets and the more the shape is uncertain, the more difficult it is to get an accurate result. As we add the slits to our model, the waves at receiver antenna decrease. This leads to lower signal power at receiver point.

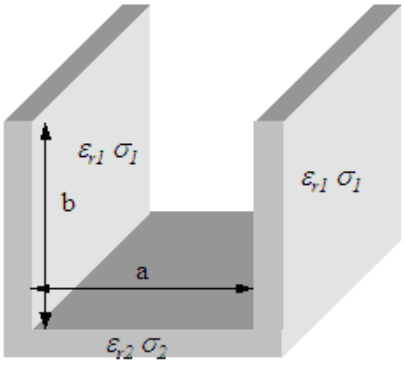

Fig. 9. 3D cross section of open-groove structure.

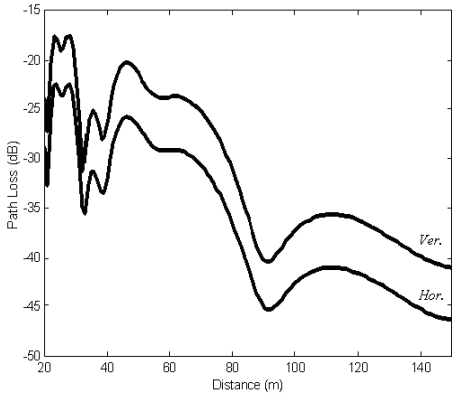

Fig. 10. The simulation results of open groove structure for horizontal and vertical polarization.

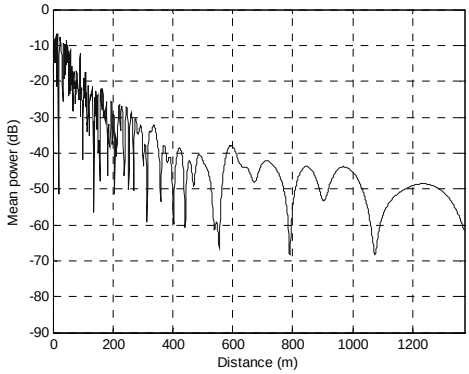

Fig. 11. The simulation results for New York City.

The result of our simulation follows the experimental results staying 10 dB below them. This is due to the contribution of the scattered waves from the other objects in the street. Also the dielectric properties of the buildings, vehicles and unexpected objects affect the total signal power at the receiver.

The following is the simulation result for the small town of Kefar–Yona, Israel [2]. The values for the scattering parameters used in the simulation are $h_b = 10$ m for average building heights, $f = 900$ MHz for the operating frequency, a=50m for the street width, $\varepsilon_r = 15$, $\sigma = 7$ for dielectric constant and conductivity of the sidewalls. The wall thickness is taken as 20 cm. In order to describe the density of the buildings in the brokenness parameter has been defined in the experimental result in the survey. These parameters were used in our simulation. Then, using 20 cm thickness as a model of vegetation canopy is added to the wall. The effect of these layers is investigated. We have found good results for relative signal loss. The signal loss shows the field intensity attenuation, which is relative to the intensity in free space at the distance 100m from the source, as it is done in the study. We have calculated up to three scatterings from the walls and ground, which are

quite close to approximate result. Higher orders do not contribute to the result more than 1 per cent.

The curves in Fig. 12, show our simulation results for urban area with and without vegetation canopy respectively. Our model gives results, which are close to experimental data [2] and can be used for predicting path loss distributions along the street. The effect of plant for signal loss causes 3-5 dB increase in simulation.

We have also run our simulation program for different environmental conditions in the city scene. We have assumed New York streets flooded and used the electric properties of fresh water and calculated the power loss of EM waves. We have used the electrical properties of asphalt in the normal condition which is $\varepsilon_r = 4.28 + j0.1$ [14-15]. The electrical properties of the fresh water are assumed as $\varepsilon_r = 81$ and $\sigma = 0.01$ [9]. Figure 13 depicts the comparison of the two cases using our model. As seen in the figure the electrical properties of the ground surface affects the power loss in the city streets. It can be inferred from this figure that the power loss decreases when the ground gets wet. Finally, we have studied loss in New York City for different brokenness parameters. We have found the following LOS contributions for different brokenness parameters.

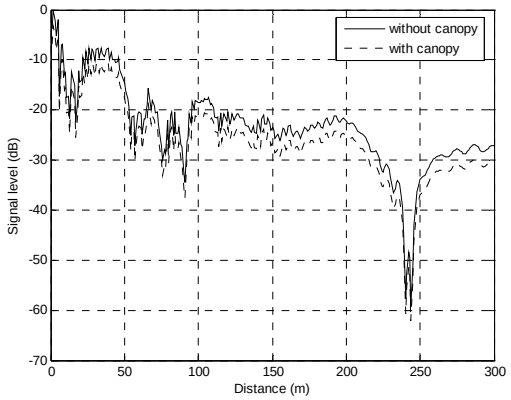

Fig. 12. The simulation result for urban area.

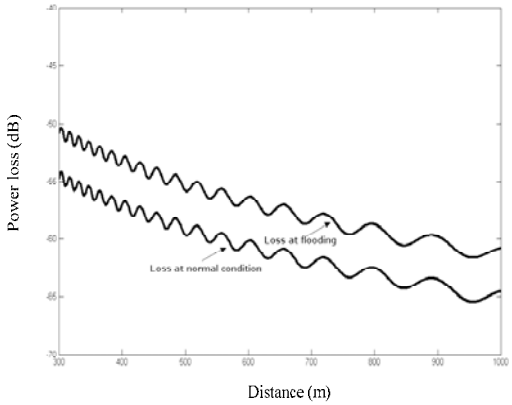

Fig. 13. Power loss of asphalt and flooded surface.

Table 1: LOS contributions of brokenness parameters.

χ	LOS contribution (in per cent)
0	100
0.4	63
0.8	40
1	32

VII. CONCLUSIONS

In this study, a new theoretical model based on the discretized properties of lossy dielectric arbitrary surfaces was developed using scattering theory. Firstly, the model is used to simulate RCS and the attenuation characteristics of EM waves. The simulation results were compared to the values in the literature and it was seen that the model agrees well with them. In our calculation we observed that in the total field, the effect of the first and second order-scattered waves are approximately 20-25 and 10 per cent respectively. After the third order scattering, the contribution of higher orders decreases so that the effect of these waves can be neglected. Direct wave, which reaches (LOS condition) to the receiver antenna is 50-60 per cent. We enhanced the new theoretical model in order to study wave propagation in urban environments for mobile applications and compared with the previous studies to verify our model.

In our developed model, the total field density in the observed point is calculated by adding the line-of-sight and scattered wave contributions from the walls. Furthermore, higher order scattered waves can also be calculated.

The developed discrete model has the following unique advantages over the earlier propagation models :

1. It is possible to calculate the contributions of each direct (LOS) and scattered waves separately. It accounts for the scattering from the walls with/without openings and ground (dry or wet) with holes and irregularities, as well as gaps between the buildings.
2. The developed model is applicable for a broad band of frequencies.
3. If the shape of the urban areas is entered to the simulation program with sufficient detail, the output gets very close to the measurement results. Even when the shape is not entered very accurately; an approximate result can be obtained.
4. This model can be used effectively for prediction of loss characteristics in a situation where two antennas are located below the roof tops in conditions of direct visibility at the ranges more than 150-200 m.
5. The proposed physical propagation model will be useful for describing urban propagation channels and can be extended to more complicated configurations including additional factors affecting the radio wave propagation.

VIII. ACKNOWLEDGEMENTS

This work is supported by Bogazici University Research Foundation (Project No;BAP03A207).

REFERENCES

[1] N. Blaunstein, *Radio Propagation in Cellular Network*, Artech House Inc, Boston-London, 2000.

[2] N. Blaunstein, "Average field attenuation in the nonregular impedance street waveguide," *IEEE Trans. on Anennas and Propagation*, vol. 64, pp. 1782-1788, Dec. 1998.

[3] J. Walfisch and H. L. Bertoni, "A theoretical model of UHF propagation in urban environments," *IEEE Trans. on Antennas and Propagation*, vol. AP-36, pp. 1788-1796, Dec. 1988.

[4] Y. P. Zhang, Y. Hwang, and J. D. Parsons, "UHF radio propagation characteristics in a straight open-groove structures," *IEEE Trans. on Vehicular Technology*, vol. 48, no. 1, pp. 249-254, Jan. 1999.

[5] European Communities, COST231 Final Report, Digital Mobile Radio Toward Future Generation Systems, pp. 115-208, 1999.

[6] D. Didascalou, Y. Venot, M. Döttling, and W. Wiesbeck, "Modeling and measurements of EM-wave propagation in the Berlin Subway," *in Millenium Conference on Antennas&Propagation AP2000*, Davos, Switzerland, April 2000.

[7] S. S. Seker and B. Altay, "Shielding properties of thin curved surfaces," *Proc. IEEE EMC-96*, Santa Clara, USA, 1996.

[8] S. S. Seker, "Radar cross section of thin dielectric bodies," *Proc. IEE*, vol. 133, no. 4, pp 305-307, Aug. 1986.

[9] D. Paris and K. Hurd, *Basic Electromagnetic Theory*, Mc Graw Hill Book Company, 1969.

[10] G. Ruck, D. Barrick, W. Stuart, and C. Krichbaum, *Radar Cross-Section Handbook*, vol. 1, Plenum Press, New York, 1970.

[11] H. Bussey and J. Richmond, "Scattering by a lossy dielectric circular cylindrical multilayer numerical values," *IEEE Trans. on Antennas and Propagation*, vol. 23, no. 5, pp. 723-725, Sep. 1975.

[12] C. Balanis, *Advanced Engineering Electromagnetics*, Wiley and Sons, pp. 578, 1989.

[13] A. J. Rustako, N. Amitay, G. J. Owens, and R. S. Roman, "Radio propagation at microwave frequencies for line-of-sight microcellular mobile and personal communications," *IEEE Trans. on Vehicular Technology*, vol. 40, no. 1, pp. 203-210, Feb. 1991.

[14] ERADS, "Expert Radar Signature Solutions, Common Radar Materials" from World Wide Web < http://stl.uml.edu/tools/scalemodel.html>.

[15] J. Wait, *Wave Propagation Theory*, Pergamon Press, New York, 1981.

APPENDIX

The parameters of (14) and (15) are given as:

$v_{is} = (v_1 + v_2) + \sin\theta_i \sin\theta_s$, $v_1 = \cos\theta_s \cos\phi_s \cos\theta_i \cos\phi_i$
$v_2 = \cos\theta_s \sin\phi_s \cos\theta_i \sin\phi_i$, $h_1 = -\sin\phi_i \sin\phi_s$
$v_3 = 0.5\sin(\phi_i + \phi_s)\cos\theta_s \cos\theta_i$, $h_2 = -\cos\phi_i \cos\phi_s$,
$h_{is} = (h_1 + h_2) = -\cos(\phi_i - \phi_s)$, $h_3 = 0.5\sin(\phi_i + \phi_s)$,
$s_1 = 2\pi a_1 J_0(x_1)$, $s_2 = \pi a_1 \left[J_0(x_1) - J_2(x_1)\cos(2\psi)\right]$,
$s_3 = \pi a_1 \left[J_0(x_1) + J_2(x_1)\cos(2\psi)\right]$
$s_4 = -2\pi a_1 \left[J_2(x_1)\sin(2\psi)\right]$ with $x_1 = k_0 a_1 \sqrt{\gamma_x^2 + \gamma_y^2}$,
$\psi = \tan^{-1}(\gamma_y / \gamma_x)$. In the above equations $J_0(x_1)$ and $J_2(x_1)$ represent Bessel function of the first kind, zero and the second order, respectively.

Selim Seker received his MS and PhD degrees in 1978 and 1982 from the George Washington University, D.C., USA. He has been working in the area of microwave remote sensing, propagation and biological effect of EM. Fields and related areas. In the summer of 1983-85 and 1987 as well as between 1982 to 1983 he was with CyberCom Co., VA, USA and conducted research in the area of EM propagation through forests. In summer of 1986, he worked on the problem of EM scattering and absorbers at BBC Baden Switzerland. On his sabbatical leave 1990-1992, he taught several different courses at both graduate and undergraduate level at GWU, and conducted one year theoretical and experimental research for NASA. He has published several journal and conference papers in the area of EM wave propagation. He is a senior member of IEEE.

Gökhan Apaydin was born in Ankara, Turkey, in 1978. He received his BS, MS, and PhD degrees in Electrical and Electronic Engineering, from Bogazici University, Istanbul, Turkey in 2001, 2003, and 2007 respectively. He was employed by Bogazici University between 2001 and 2006. He has been a research engineer at University of Technology Zurich applied R&D since 2005. He has been working several research projects on EM scattering, the development of Finite Element Method for electromagnetic computation, propagation, web-splines, positioning, RFID applications, filter design, wavelet and related areas. He has published 3 journal papers and presented 11 conference papers. He is also the author of many technical reports and research books at University of Applied Science Zurich. He is a member of IEEE.

MONURBS: A Parallelized Fast Multipole Multilevel Code for Analyzing Complex Bodies Modeled by NURBS Surfaces

[1]I. González, [2]E. García, [1]F. Saez de Adana, and [1]M. F. Cátedra

[1]Dept. Ciencias de la Computación. Universidad de Alcalá.
28871 Alcalá de Henares (MADRID) SPAIN
Fax: +34 91 885 6646. E-mail: felipe.catedra@uah.es

[2]Dept. Automática. Universidad de Alcalá.
28871 Alcalá de Henares (MADRID). SPAIN

Abstract – This paper presents a Parallelized Multilevel Fast Multipole (MLFMA) Moment Method (MoM) code for analyzing the scattering and radiation from electrically large complex bodies modeled by Non-Uniform Rational B-Spline Surfaces (NURBS). The bodies are represented by NURBS surfaces which are discretized without remeshing the original geometry. The basis and testing functions are defined and conformed to the exact representation of the geometry. This code has been parallelized using Message Passing Interface (MPI) and it has been successfully applied to the study of large bodies including complex and periodic multilayer structures where the real size and shape are very important.

I. INTRODUCTION

In recent years, the application of the MoM technique to the analysis of scattering from large and arbitrary objects has been achieved [1]. The application of the multilevel fast multipole technique to the MoM significantly reduces the computer requirements of memory and CPU-time for analyzing electrically large objects.

In this paper the MLFMA technique [1] is applied to the analysis of complex objects composed of a perfect or real conducting electric and/or dielectric material, modeled by NURBS surfaces [2]. Using these surfaces, any arbitrary object can be represented with very little amount of information without loss of accuracy. In the application presented, the MLFMA technique is applied to quadrangular patches defined over small pieces of NURBS surfaces. These quadrangles totally conform to the real shape of the bodies under analysis. With the proposed method, it is possible to analyze the scattering field of large and complex bodies, including multilayer conformed periodic structures, taking into account their real finite size and shape. Thus, the electromagnetic kernel works with the original Computer Aided Design (CAD) model obtained from the general designing process and no remeshing of the geometry is required. This means that no representation error is added.

The code has been improved for analyzing bodies composed of conductors and dielectric slabs, both modeled using volumetric rooftops. Both conductors and dielectric slabs can be limited by curved surfaces. Also, when the dielectric slabs are electrically thin, the "thin dielectric sheets" (TDS) approximation ([1]) is considered for reducing the CPU time.

To analyze electrically very large objects, a parallel version of the code has been developed. A MPI [3] paradigm has been used because it can be applied in both distributed memory machines and in shared memory ones. The goal is to analyze large objects with processors with relatively small memory and with an affordable execution time.

II. MODEL DISCRETIZATION

Traditionally the geometrical models are defined by planar facets. The geometrical models for MONURBS are defined by NURBS surfaces. NURBS surfaces are parametric surfaces used as a standard format for exchange in CAD that permits the representation of complex objects with very little data. Figure 1 shows a NURBS surface in the real space and its definition in the parametric space.

The geometrical model is discretized using quadrangular patches fully conformed to the exact shape of the body. Every surface is divided into quadrangular patches, thus resulting in a lower number of subdomains in comparison with other discretization techniques. In [4] the discretization is made in the parametric space, but the problem is that an equally spaced step in the parametric space can result in a non-equally spaced step in the real space. Thus, this can produce a higher number of subdomains in NURBS degenerated points that can give ill-conditioned problems. The new approach produces the discretization in the real space, thus resulting in a quadrangular mesh nearly uniform in the shape and size of the patches. Figure 2 shows the difference between the division in the parametric space and the real space. A lot

of patches are observed near the pole for the division in the parametric space.

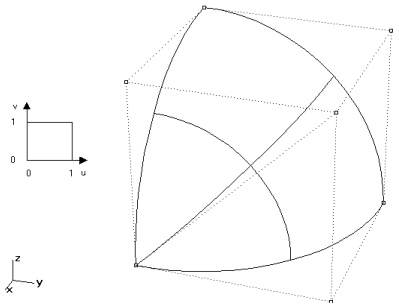

Fig. 1. Example of NURBS surface.

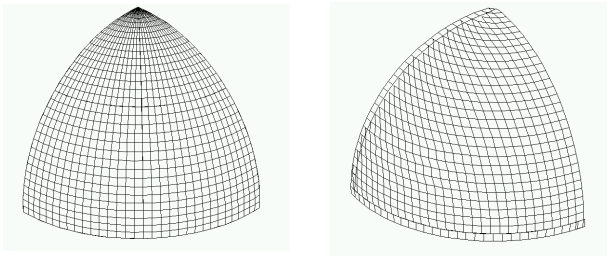

(a) (b)

Fig. 2. Discretization (a) parametric space and (b) real space.

III. ELECTROMAGNETIC KERNEL

The moment method is applied in the parametric space, so the surface current is defined as,

$$\vec{J}(u,v) = J_u(u,v)\vec{e}_u(u,v) + J_v(u,v)\vec{e}_v(u,v) \tag{1}$$

where u and v are the parametric coordinates, and $\vec{e}_u(u,v)$ and $\vec{e}_v(u,v)$ vectors are the derivatives in the parametric space.

Modified rooftops and razor-blade functions are used as basis and testing functions, respectively [3]. Both functions conform to the quadrangular meshes previously described that can be arbitrarily curved (see Figs. 3 and 4).

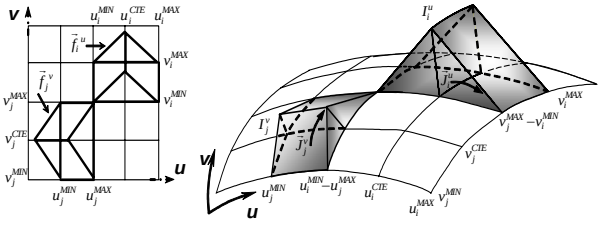

Fig. 3. Basis functions conformed to a curved conducting surface.

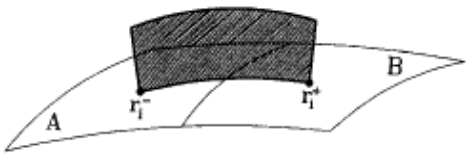

Fig. 4. Testing function conformed to a curve conducting surface.

The electromagnetic kernel of MONURBS can use the Electric Field Integral Equation (EFIE), the Magnetic Field Integral Equation (MFIE), the Combined Field Integral Equation (CFIE) or the Hybrid Integral Equation. For instance, for the EFIE calculation, the coupling between two subdomains i and j is calculated in the parametric space, taking into account both the inductive and the capacitive terms. For the inductive term we have,

$$Z_{ij}^{ind} = \int_{r_i^-}^{r_i^+}\left[\frac{j\omega\mu_0}{4\pi}\int_{S_m} G(\vec{r},\vec{r}')\vec{J}_j^{\,m}(\vec{r}')dS'\right]d\vec{l} + \int_{r_i^-}^{r_i^+}\left[\frac{j\omega\mu_0}{4\pi}\int_{S_n} G(\vec{r},\vec{r}')\vec{J}_j^{\,n}(\vec{r}')dS'\right]d\vec{l} \tag{2}$$

where $G(\vec{r},\vec{r}')$ is the Green function and m, n are the subpatches that define the subdomain. For the capacitive term,

$$Z_{ij}^{cap} = \int_{r_i^-}^{r_i^+}\left[-\frac{1}{j4\pi\varepsilon_0\omega}\nabla\int_{S_m}\frac{G(\vec{r},\vec{r}')}{S_m}dS'\right]d\vec{l} + \int_{r_i^-}^{r_i^+}\left[\frac{1}{j4\pi\varepsilon_0\omega}\nabla\int_{S_n}\frac{G(\vec{r},\vec{r}')}{S_n}dS'\right]d\vec{l}\ . \tag{3}$$

The calculation of the moment method matrix elements is one of the most computational expensive steps. The integrals shown in equations (3) and (4) are calculated using the Gauss quadrature method. All the surface integrals are evaluated in the rectangular parametric space of the corresponding subpatch (u, v parametric coordinates, shown in Fig. 3). This is not difficult because only a variable change in the integration is required. The computation of the impedance matrix terms is optimized by computing once and storing the value of the integrand functions at the Gaussian integral points. These values are used in many integrals. Also, all the parameters of the subpatches (normalized currents, points, derivatives, etc.) are computed once and stored in the geometrical preprocess to avoid further recomputations when the coupling between subdomains is being calculated.

The Fast Multipole Method (FMM) has been implemented and applied to reduce the memory and CPU-time. The coupling between subdomains is calculated using the multipole approximation [1],

$$Z_{ij} = \frac{jk}{4\pi}\int d^2k \vec{V}_{fmj}(\hat{k})\cdot\alpha_{mm'}(\hat{k}\cdot\vec{r}_{mm'})\cdot\vec{V}^{*}_{sm'i}(\hat{k}) \quad (4)$$

where $\vec{V}^{*}_{sm'i}(\hat{k})$, $\alpha_{mm'}(\hat{k}\cdot\vec{r}_{mm'})$ and $\vec{V}_{fmj}(\hat{k})$, respectively are the aggregation, the translation and the disaggregation terms, respectively, of the FMM. The aggregation term is calculated using,

$$\vec{V}_{fmj}(\hat{k}) = \frac{j\omega\mu}{4\pi}\left[\int_{S_m}\vec{J}^{m}_{j}(\vec{r}\,')e^{jk\hat{k}\cdot(\vec{r}_c-\vec{r}\,')}dS' + \int_{S_n}\vec{J}^{n}_{j}(\vec{r}\,')e^{jk\hat{k}\cdot(\vec{r}_c-\vec{r}\,')}dS'\right] \quad (5)$$

where m, n are the subpatches of the subdomain, $\hat{k}$ is the wave vector and $\vec{r}_c$ is the center of the FMM region where the subdomain lies. The disaggregation term is calculated using,

$$\vec{V}^{*}_{fmi}(\hat{k}) = \int_{r_i^-}^{r_i^+} e^{-jk\hat{k}\cdot(\vec{r}_c-\vec{r}\,')}d\vec{l}\,. \quad (6)$$

In addition, the MLFMA has been implemented as an extension of the FMM. The number of levels can be chosen by the user. The aggregation and disaggregation terms of the highest levels are obtained from the lowest level terms using interpolation-anterpolation with matrix-vector product [1].

Modified volumetric rooftops and razor-blade functions, [5], defined over curved domains are considered (Fig. 5) for the analysis of dielectric bodies.

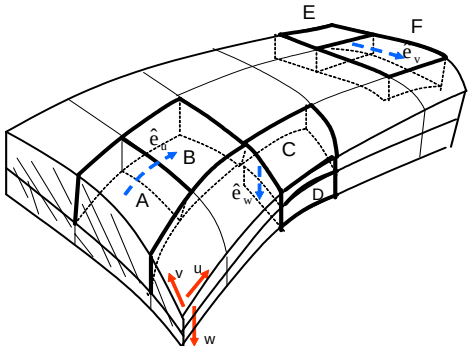

Fig. 5. Basis and testing functions totally conformed to volumetric dielectric bodies.

A parallel version of the code has been developed to be used in both distributed and shared memory machines. This version is based on MPI. The geometry of the problem is immersed into a gridded MLFMA space (Fig. 6). Each processor of the grid computes the coupling that affects the Moment Method unknowns of the cells associated to this processor (computed rigorously or by the multilevel fast multipole approximation). To achieve this goal, each processor needs data computed in others processors. This information is obtained by exchanging explicit messages through a network. All processors cooperate in the resolution of the system of equations when a problem is solved.

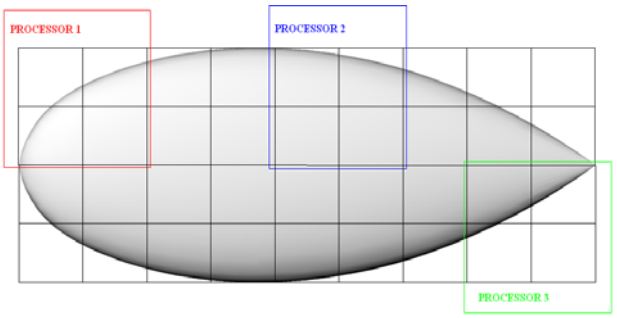

Fig. 6. Problem distribution between processors in the MPI MLFMA application.

IV. RESULTS

Test cases have been tested with MONURBS in several areas of application such as Radar Cross Section, radiation patterns of antennas on board and analysis of multilayer periodic structures like frequency selective surfaces and reflect arrays.

The first case we present here is the analysis of the FLAMME stealth aircraft (see Fig. 7). In this case, a very accurate representation of the actual shape of the aircraft is required. The Bistatic RCS has been obtained for a sweeping angle ϕ ranging from 206º to 360º and θ = 90º at a frequency of 3 GHz.

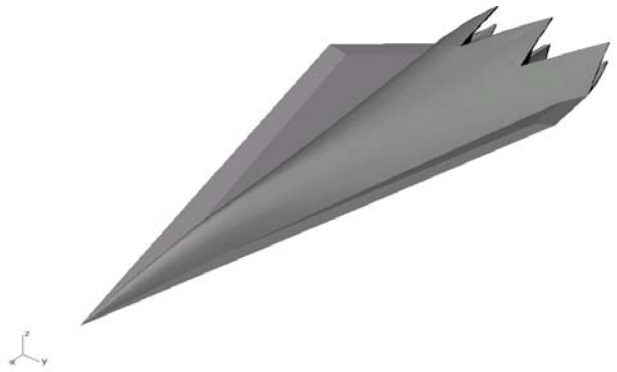

Fig. 7. Geometrical model of FLAMME aircraft.

Figures 8 and 9 compare the simulated and the measured values for polarizations VV and HH, respectively. A good agreement between the simulations and the measurements can be observed in both figures.

The next example analyzed is the perfect electric conducting NASA almond case shown in Fig. 10. The case was proposed in reference [6]. The geometry is defined by the following parametric equations (all dimensions are in inches),

a) for $-0.416667 < \mathbf{t} < 0$

$$x = d\,t$$
$$y = 0.193333\,d\left[\sqrt{1-\left(\frac{t}{0.416667}\right)^2}\right]\cos\psi \qquad (6)$$
$$z = 0.06444\,d\left[\sqrt{1-\left(\frac{t}{0.416667}\right)^2}\right]\sin\psi$$
$$-\pi < \psi < \pi$$

b) for $0 < \mathbf{t} < 0.583333$

$$x = d\,t$$
$$y = 4.833450\,d\left[\sqrt{1-\left(\frac{t}{2.083350}\right)^2}-0.96\right]\cos\psi \qquad (7)$$
$$z = 1.61115d\left[\sqrt{1-\left(\frac{t}{2.083350}\right)^2}-0.96\right]\sin\psi$$
$$-\pi < \psi < \pi$$

where d, the length of the almond, is 9.936 inches. The Monostatic RCS of the almond have been obtained at 7 GHz for HH polarization, θ = 90º and a sweep angle ϕ ranging from 0º to 180º.

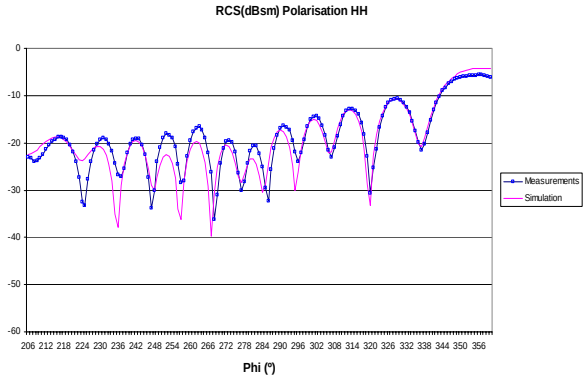

Fig. 8. Measured and computed Bistatic RCS values for FLAMME aircraft, HH polarization.

To show the advantages of the proposed mesh based on NURBS over meshes based on triangular facets, the almond has been analyzed with MONURBS and FIESTA codes. FIESTA is a moment method code that uses a flat triangular mesh, RWG basis functions and a fast direct solution of the moment method linear system of equations, [6]. The almond has been analyzed considering 6, 10, 20, and 40 subdomains per wavelength. The numerical results are also compared between with measurements.

Table 1 shows the number of unknowns required by both numerical approaches for the different number of divisions considered for the geometrical mesh.

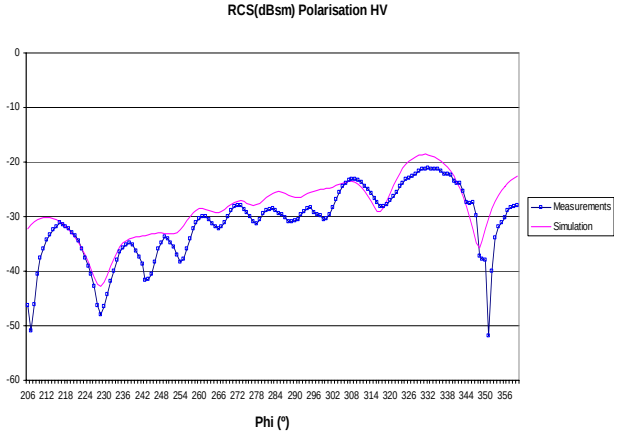

Fig. 9. Measured and computed Bistatic RCS values for FLAMME aircraft, HV polarization.

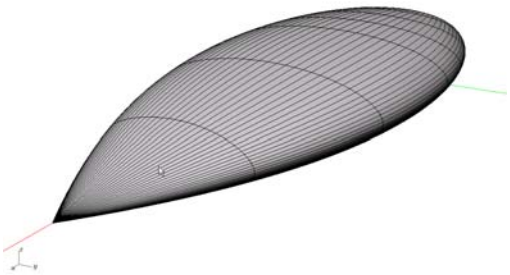

Fig. 10. Geometrical model of the NASA almond.

Table 1. Number of unknowns for the two kinds of meshes considered.

	Unknowns	
Divisions	NURBS	RWG
6	1700	3753
10	4810	8862
20	19730	30492
40	80198	99915

Comparing the results obtained with the NURBS based mesh and the flat faceted mesh, it can be noticed that 6 subdomains per wavelength are not enough to obtain good results. In this case there are several differences between the two numerical approaches and the measurements (Fig. 11). If the number of divisions is increased, the results obtained by the two methods converge to the same values. However, the number of unknowns required by both approaches is different; the mesh based on NURBS requires fewer unknowns than the triangular flat faceted mesh. Comparing with the measurements, both methods provide good results for ten or more subdomains per wavelength (Figs. 12, 13, and 14).

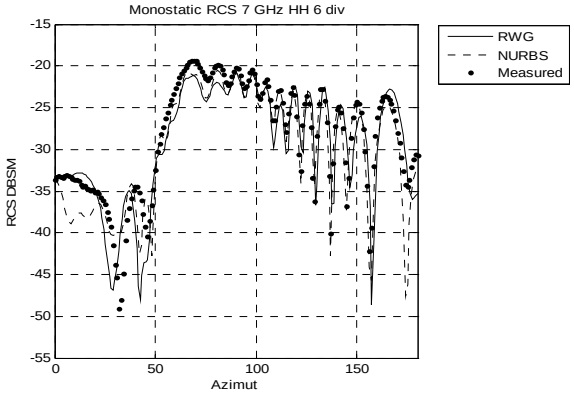

Fig. 11. Comparison between the monostatic numerical RCS values obtained using 6 subdomains per wavelength and measurements.

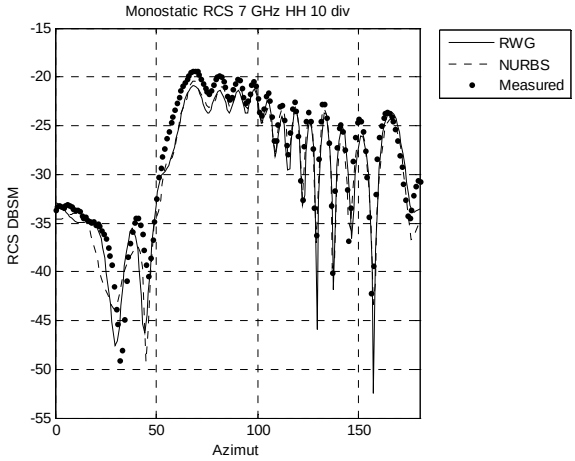

Fig. 12. Comparison between the monostatic numerical RCS values obtained using 10 subdomains per wavelength and measurements.

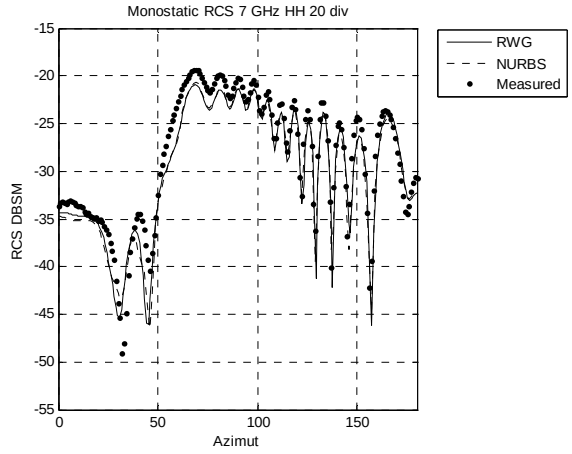

Fig. 13. Comparison between the monostatic numerical RCS values obtained using 20 subdomains per wavelength and measurements.

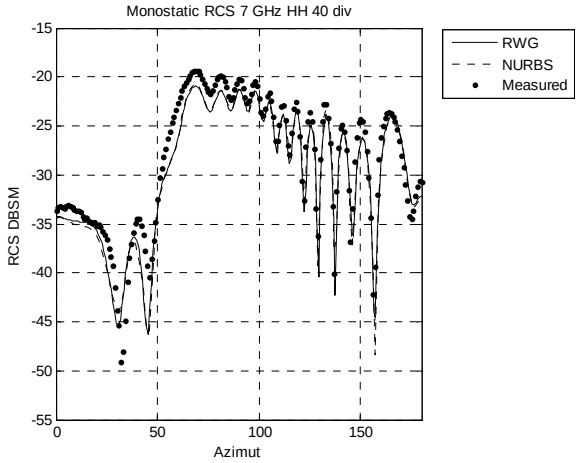

Fig. 14. Comparison between the monostatic numerical RCS values obtained using 40 subdomains per wavelength and measurements.

MONURBS can be also used for obtaining the radiation patterns of antennas on board complex structures. Here the case of an antenna placed on a mock-up of the satellite Jason I is presented. The mock-up has a size of 2.220 m x 1.558 m x 1.507 m and it is shown in Fig. 15 with the antenna location highlighted. This case has been analyzed at 2.2 GHz and the results, shown in Fig. 16 for the cut $\phi = 67.5^{o}$, agree with measurements made by the CNES in an anechoic chamber. The number of unknowns is 152.867 and the simulation lasted for 4 h 28 m on an AMD Opteron 2.4 GHz one processor machine.

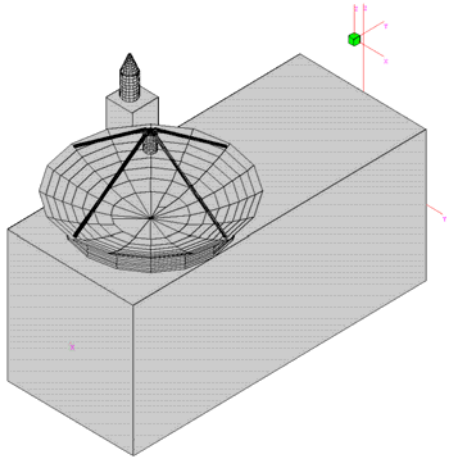

Fig. 15. Geometrical model of Jason-I.

The analysis of multilayer periodic structures could be also conducted with MONURBS using the MLFMA. Several complex multilayer periodic structures have been analyzed and compared with measurements, showing good agreements.

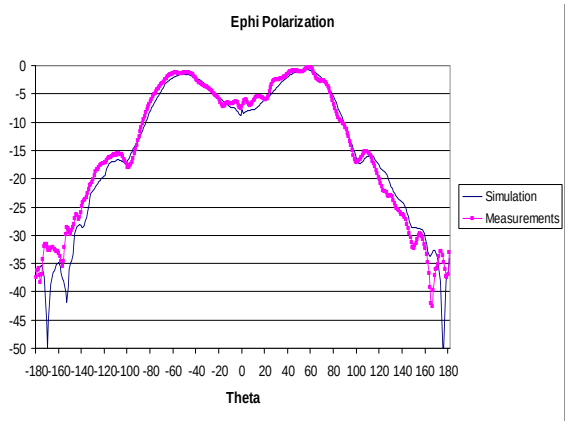

Fig. 16. Comparison between measurements and simulations.

The first complex multilayer periodic structure is the dual three layer reflect array, [7], shown in Fig. 17. The reflect array was designed to generate two pencil beams for TV SAT broadcasting pointing at Europe (11.45 GHz – 12.75 GHz H polarization) and USA (11.45 GHz – 11.7 GHz V-Polarization). The electrical model, shown in Fig. 18, has three layers of periodic structures, several dielectric layers and the ground plane. The reflect array is elliptical with axes at 1036 mm and 980 mm. The number of unknowns considered for the analysis at 12.1 GHz is 1.508.275.

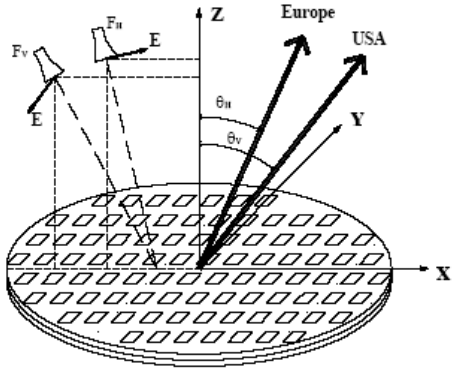

Fig. 17. Three layer reflect array.

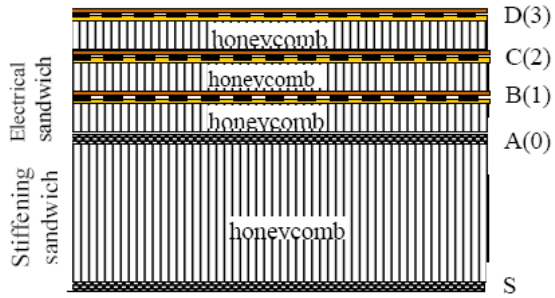

Fig. 18. Electrical description of the reflect array.

The results obtained for both polarizations at 12.1 GHz are shown in Figs. 19 and 21, while the measurements are shown in Figs. 20 and 22. For the H polarization, the location of the pencil beam is right, and is so wide like in the measurements. The contour plots of the dBi are at the same level.

For the V polarization, the location of the pencil beam is right and the shape is very similar to this one obtained in the measurements. This polarization is less sensitive to the dielectric effect.

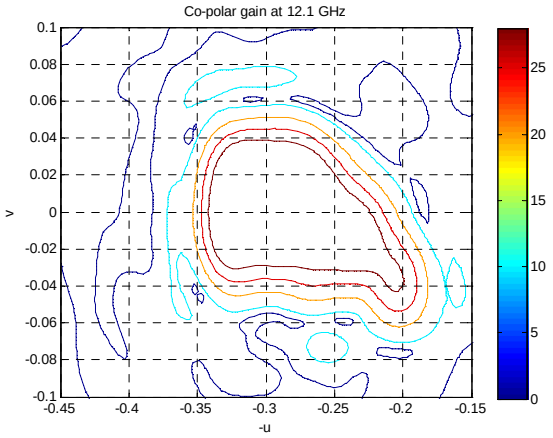

Fig. 19. Contour plot of dBi for the H polarization. Simulation performed at 12.1 GHz.

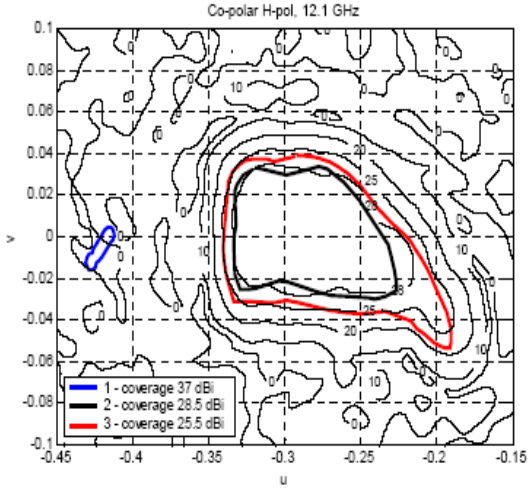

Fig. 20. Contour plot of dBi for the H polarization. Measurements.

The results obtained with the code and the measurements performed at a frequency of 11.05 GHz for the V polarization are shown in Figs. 21 and 22. A good agreement between the simulations and the measurements can be observed.

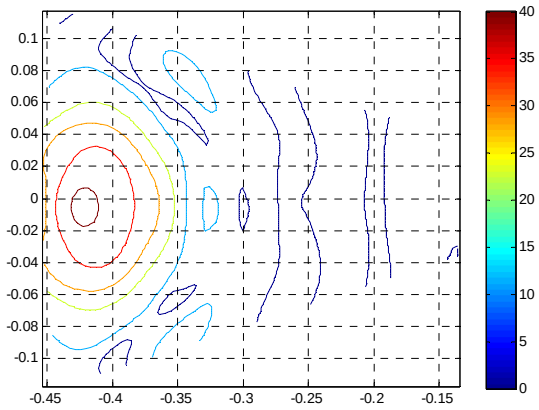

Fig. 21. Contour plot of dBi for V polarization. Simulation performed at 11.05 GHz.

The second periodic structure analyzed is the circular reflect array shown in Fig. 23. It has a radius of 130 mm, a dielectric layer thickness of 0.381 mm and $\varepsilon_r = 2.2$. The primary source is located at (0 mm, 0 mm, 65 mm) and the central design frequency is 94 GHz. This reflect array has been designed and measured by Laboratoire d'Electronique Antennes et Télecommunications, University of Nice, France. Fig. 24 shows the comparisons between the measurements and the simulations for the E plane. There is a good agreement between the measurements and the simulations in a range from 0º to 20º.

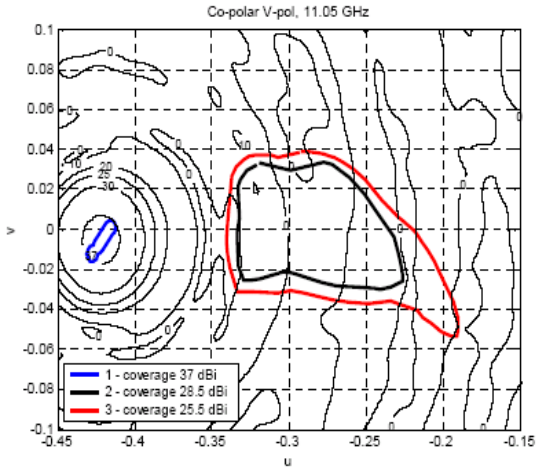

Fig. 22. Contour plot of dBi for V polarization. Measurements.

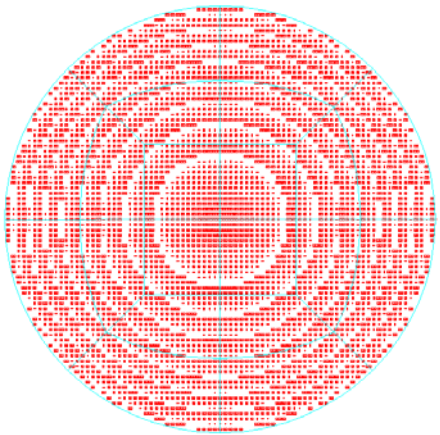

Fig. 23. Circular reflect array.

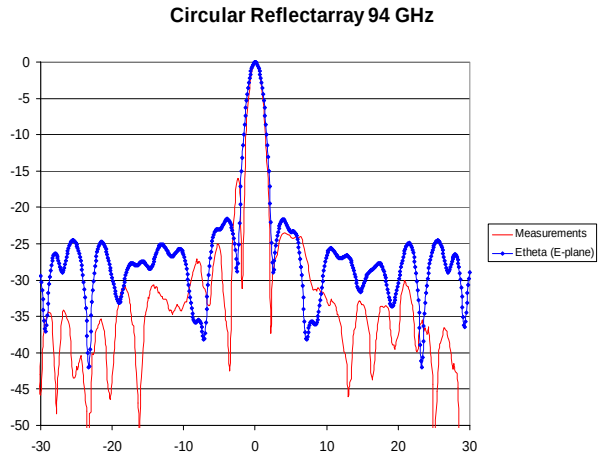

Fig. 24. Comparison between measurements and simulation for the reflectarray at 94 GHz.

V. CONCLUSIONS

An application of the MLFMA has been presented to the analysis of scattering of complex bodies modeled by NURBS surfaces. These surfaces are a powerful tool to represent complex bodies with accuracy. New basis and testing functions defined over the NURBS surfaces/volumes of the model are considered, reducing the number of unknowns and obtaining good results compared with measurements as is demonstrated through several cases.

A code named MONURBS based on the techniques presented here has been implemented. The code is a versatile tool for successfully analyzing scattering and radiation problems from complex structures. MONURBS is commercially available.

ACKNOWLEDGEMENTS

The authors thank the Antenna Department of CNES (France) for the geometrical models and measurements of the JASON-I test case, Prof. Encinar from the Polytechnic University of Madrid for the model and measurements of the multilayer reflectarray, the Laboratoire d'Electronique Antennes et Télecommunications, University of Nice, France for the model and measurements of the reflectarray at 94 GHz, the Electromagnetism and Radar Department, ONERA for the FLAMME test case, and the AntennaLab research group at Universitat Politècnica de Catalunya for the results of the NASA almond obtained with the FIESTA code.

This work has been supported, in part by the Spanish Department of Education and Science, Project TEC 2004-03187 and by Comunidad de Madrid and Universidad de Alcalá, projects PI2005/069, CAM-UAH 2005/005 and Project S-0505/TIC/0255, and I+D+I National Plan , Ref. TEC2006-03140.

REFERENCES

[1] W. C. Chew, J. Jin, E. Michielssen, and J. Song, *Fast and efficient algorithms in computational electromagnetics*, Editors. Arctech House INC., 2001.

[2] G. Farin, "Curves and surfaces for computer aided geometric design," Academic Press, 1988.

[3] G. William "Using MPI portable parallel programming with the message-passing interface," The MIT Press, 1999.

[4] L. Valle, F. Rivas, and M. F. Cátedra, "Combining the moment method with geometrical modelling by NURBS surfaces and Bézier patches," *IEEE Transactions on Antennas and Propagation*, vol. 42, no. 3, pp. 373 - 381, March 1994.

[5] S. M. Rao, D. R. Wilton, and A. W. Glisson "Electromagnetic scattering by surfaces of arbitrary shape," *IEEE Transactions on Antennas and Propagation*, pp. 409 - 418, 1982.

[6] A. Heldring, J. M. Rius, J. M. Tamayo, J. Parrón, and E. Ubeda "Fast direct solution of method of moments linear system," *IEEE Transactions on Antennas and Propagation*, vol. 55, no. 11, November 2007.

[7] J. A. Encinar, L. S. Datashvili, J. A. Zornoza, M. Arrebola, M. Sierra-Castaner, J. L. Besada-Sanmartin, H. Baier, and H. Legay, "Dual-polarization dual-coverage reflectarray for space applications," *IEEE Transactions on Antennas and Propagation*, vol. 54, no. 10, pp. 2827 – 2837, October 2006.

Iván González Diego was born in Torrelavega, Spain in 1971. He received the B.S. and M.S. degrees in telecommunications engineering from the University of Cantabria, Spain, in 1994 and 1997 respectively, and the Ph.D degree in telecommunications engineering from the Univeristy of Alcalá , Madrid, Spain in 2004. He worked in the Detectability Laboratory of the National Institute of Technical Aerospace (INTA), Madrid, Spain and as an Assistant Researcher at the University of Alcalá. He currently works as Assistant Professor in this university. He has participated in several research projects with Spanish and European companies, related with analysis of on board antennas, radio propagation in mobile communications, RCS computation, etc. His research interests are in numerical methods applied to the electromagnetic problems, like genetic algorithms and numerical methods to represent complex bodies for the electromagnetic techniques.

Eliseo Garcia was born in Madrid, Spain, in 1977. He received the B.S., M.S. and Ph.D. degrees in telecommunication engineering from the University of Alcalá, Spain, in 1999, 2001 and 2005, respectively. Since 2005, he worked at the University of Alcalá, first as Assistant Professor and since 2006 as Associated Professor in the Automatic Department. His research interests include numerical methods applied to scattering and radiation problems, parallel computing and fast computational techniques applied to electromagnetics.

Francisco Saez de Adana was born in Santander, Spain, in 1972. He received the BS, MS and PhD. degrees in Telecommunications Engineering from the University of Cantabria, Spain, in 1994, 1996 and 2000, respectively. Since 1998 he works at the University of Alcalá, first as assistant professor and since 2002 as professor. He has worked as faculty research at Arizona State University from March 2003 to August 2003. He has participated in more than forty research projects with Spanish, European, American and Japanese companies and universities, related with analysis of on board antennas, radio propagation in mobile communication, RCS computation, etc. He has directed two Ph. D. Dissertations, has published sixteen papers in referred journals and more than 40 conference contributions at international

symposia. His research interests are in areas of high-frequency methods in electromagnetic radiation and scattering, on-board antennas analysis, radio propagation on mobile communications and ray-tracing acceleration techniques.

Manuel F. Catedra received his M.S. and Ph. D. degrees in Telecommunications Engineering from the Polytechnic University of Madrid (UPM) in 1977 and 1982 respectively. From 1976 to 1989 he was with the Radiocommunication and Signal Processing Department of the UPM. He has been Professor at the University of Cantabria from 1989 to 1998. He is currently Professor at the University of Alcalá, in Madrid, Spain.

He has worked on about 60 research projects solving problems of Electromagnetic Compatibility in Radio and Telecommunication Equipment, Antennas, Microwave Components and Radar Cross Section and Mobile Communications. He has developed and applied CAD tools for radio-equipment systems such as Navy-ships, aircraft, helicopters, satellites, the main contractors being Spanish or European Institutions such as EADS, ALCATEL, CNES, ALENIA, ESA, DASA, SAAB, INTA, BAZAN, INDRA, the Spanish Defence Department.

He has directed about 15 Ph D. dissertations, has published about 45 papers (IEEE, Electronic Letters, etc), two books, about 10 chapters in different books, has given short courses and has given around a hundred and thirty presentations in International Symposia.

Modeling and Simulation of Branched Wiring Networks

C. Lo and C. Furse

University of Utah,
Department of Electrical and Computer Engineering,
Salt Lake City, Utah, USA
Email: cfurse@ece.utah.edu

***Abstract* –** This paper presents a method to analyze the reflectometry responses of a branched network of non-ideal wires. A modified bounce diagram that uses a transition matrix to keep track of signal flow is used. This approach is further improved by including the complex propagation constant to include the frequency dependent filtering effect (phase delay and attenuation) of the non-ideal transmission lines.

I. INTRODUCTION

Modeling and simulation of transmission lines [1-3] has been used to evaluate reflectometry responses or data transmission capability for a variety of applications, particularly evaluation of large scale integrated circuits. With the increasing commercial interest in communication over power lines [4], wire health monitoring for safety and reliability [5], and multipoint communication systems for sensor networks, the ability to perform accurate simulation of transmission responses on branched networks of wires is very important.

A number of approaches for simulating individual point-to-point transmission lines have been developed. Most methods typically rely on the RLGC lumped element model, which models the transmission line as a set of lumped element circuit parameters. Time [6, 7] and frequency domain [8, 9] solutions exist for non-ideal transmission lines including the frequency-dependent losses of the lines. While single lines are of interest in many applications, there are also a number of applications including power distribution systems where the lines branch one or many times, carrying power to multiple locations. Little work has been done on these branched networks. A matrix-based method for analyzing nonideal networks in the time domain was given in [7]. This method works well and could be extended to networks of any size, but it quickly becomes cumbersome and difficult to program for any but the simplest networks. A more scalable method was desired.

This paper introduces a new approach to simulate transmission lines, including easy scalability for branched networks for arbitrary time domain input signals injected at multiple points throughout the network. By merging time domain and frequency domain simulations in a method similar to [6], frequency dependent attenuation on the lossy lines can be taken into consideration for more accurate modeling and simulation. This paper describes the ideal and realistic modeling efforts and how the signatures compare to measured results. The specific application of interest for this paper is the use of reflectometry for location of faults on branched networks of aircraft wiring; however the approach can be readily adapted to other applications.

We will discuss in section II how the transition matrix and state vectors are defined, and present the simulation procedure. The simulation result is compared with measured data in section III. The lumped-element model of the transmission line is the added to the model, and the simulated result is compared with measured data again in section IV.

II. MATRIX REPRESENTATION OF BRANCHED NETWORK

The use of a bounce diagram is a well established method for studying and simulating ideal transmission lines with impedance discontinuities [10]. The bounce diagram is a time domain representation of the reflections in a wire as a set of "bounces" that can be added up to determine the time domain signatures of the signals (reflectometry or communication) on the wire. For transmission lines with multiple branches, the traditional bounce diagram becomes unpalatably complex. Each signal that reaches a branch reflects off the branch and transmits into the branch. To keep track of all of the arms of the branched network, an individual bounce diagram would be needed for each branch, and these separate diagrams would need to be coupled at all of the junction points. In effect, this is what the method described in this paper does. One way to do this is to use a time domain modeling method such as the finite difference time domain method (FDTD) [11], which models the network as an RLGC network, provides special connectivity boundary conditions at all of the junctions, and iteratively evaluates the time domain fields as they move throughout the model. This method works well and provides accurate results, however it is not ideal for use in future work that uses this "forward" model to analyze measured data and produce a "reverse" model of the network that causes them.

In order to provide a simpler method for analysis of the reverse method, a matrix-based approach was used to

replace the iterative FDTD method. This is done by subdividing all of the branches of a network into sections of equal length and evaluating the propagation on each segment of the network simultaneously. The term "equal length" means it takes the signal an equal amount of time, T, to travel between adjacent nodes {e.g., x_i and x_j, or x_k and x_l in Fig. 1} where there is an equal distance of z between the adjacent nodes within wire segments. A transition matrix $A = [a_{uv}]$, where u and v are the column and row index, respectively, is used to keep track of the signal flows. The entries of the transition matrix indicate how much of the signal at a particular node in one instant will be redistributed to the other nodes in the following time instant. For a network that has minimal interconnection as shown in Fig. 1, this matrix will be very sparse. A gridded network (which might be used for sensor connectivity) would be less sparse. The column index is the initiating node, and the row index is the receiving nodes.

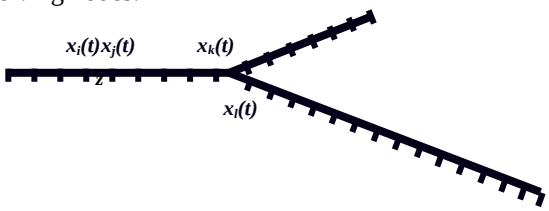

Fig. 1. An example of a simple branched network.

On a transmission line as shown in Fig. 2, the reflection coefficient at any location p on the wire is given by,

$$\Gamma = \frac{V_{ref}}{V_{inc}} = \frac{Z_1 - Z_0}{Z_1 + Z_0} \tag{1}$$

and the transmission coefficient is given by,

$$T = 1 + \Gamma = \frac{V_{trans}}{V_{inc}} \tag{2}$$

where V_{inc} is the incident voltage, V_{ref} is the reflected voltage, V_{trans} is the transmitted voltage, Z_0 and Z_1 are the impedance of the transmission line before and after the point p.

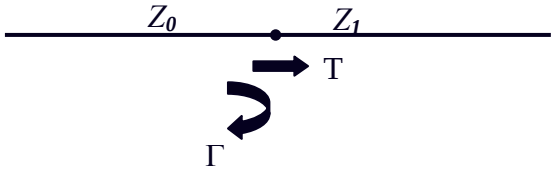

Fig. 2. Illustration of transmission and reflection coefficients.

When the impedances are equal at adjacent notes, such as x_i and x_j shown in Fig. 1, the reflection coefficient is 0, and the transmission coefficient is 1. When a junction between two wires of equal impedance Z_0 is encountered, their effective impedance is $Z_0/2$, the reflection coefficient is 1/3, and the transmission coefficient is 2/3. This means for a network as in Fig. 1, we will have $a_{ij} = 1$, $a_{kl} = 2/3$, etc.

At time t, the signal containing the reflections from all of the nodes can be presented as a state vector x_t where the signal at all of the nodes at time t can be found from the signal at the previous time t-T,

$$\overline{x}_t = A\overline{x}_{t-T} \,. \tag{3}$$

This method is iterative from time step to time step, and is therefore well suited for evaluation of a reflectometry signature, which is normally represented in the time domain. The method is simpler and faster than the FDTD method, and can be adapted to include the effects of frequency dependent attenuation that is present on all realistic wiring systems as described in the following section.

III. COMPARISON OF SIMULATED AND MEASURED DATA

Figure 3 shows a branched network that is simulated with this method (ideal case) and compared with its measured time domain reflectometry (TDR) signature for realistic (slightly lossy, RG58 coax) wire. A TDR transmits a fast rise time step function down the wire and records its reflections in the time domain. The location and change in impedance along the wire are determined from the observation of the delay and the magnitude of the reflection.

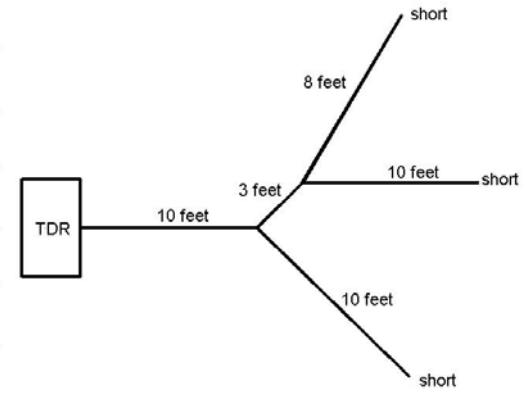

Fig. 3. Branched network to be simulated and measured with TDR. The cables are 50 ohm RG58 coaxial cable.

IV. LUMPED-ELEMENT MODEL OF TRANSMISSION LINE

We can see from Fig. 4 that the simulation is close to the measured response, but it misses the frequency dependent filtering effect of the lossy transmission line. Many transmission lines are much lossier than this coaxial cable and as a result have a much greater mismatch between ideal and measured data. This attenuation is frequency-dependent and can be added to the model by including RLGC transmission line parameters [10].

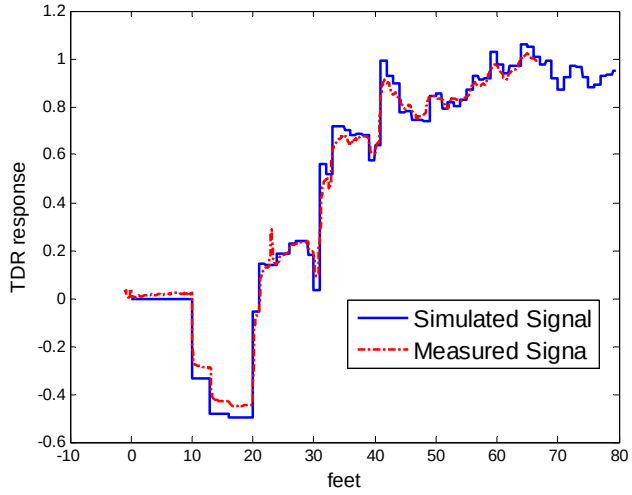

Fig. 4. Comparison of simulated and measured TDR responses for the network of wires shown in Fig. 2.

In equation (4) R is the resistance of the conductor, which is typically small; however, G is the conductance in the insulation and the region around an unshielded transmission line which is typically not small for the high frequency terms in the TDR step function. The complex propagation constant describes the attenuation (real part) and phase shift (imaginary part) for a transmission line,

$$\gamma(\omega) = \sqrt{(R + j\omega L)(G + j\omega C)}\,. \tag{4}$$

This propagation can be considered to be a filter with a transfer function of,

$$H(\omega) = e^{-\gamma(\omega)z}\,. \tag{5}$$

Because it now involves a filtering effect, the signal contained in at a node is now no longer single valued but is a vector of signal values in time at each individual node as shown in Fig. 5.

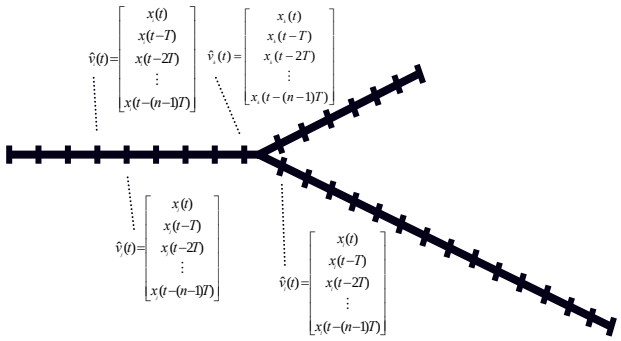

Fig. 5. Illustration of signal vectors, where $x_i(t)$, $x_j(t)$, $x_k(t)$ and $x_l(t)$ are as represented in Fig. 1.

The sampling interval or time resolution for the simulation is naturally determined by the distance z between the adjacent nodes, i.e. the time it takes for the signal to travel a distance of z that is T as in equation (1). According to sampling theory, this sampling interval determines the highest frequency contained in our simulation. At the same time, the frequency resolution, $\Delta\omega$, of the simulation is determined by the length of the signal vectors at individual nodes.

Let the length of the signal vectors be n, and the highest simulation frequency be Ω, which gives the following relationships,

$$\Omega = n\Delta\omega = \frac{2}{T} \tag{6}$$

and

$$nT = \frac{2}{\Delta\omega}\,. \tag{7}$$

The discrete form of the filter $H(\omega)$ becomes

$$H = \begin{bmatrix} 1 & & & & & & \\ & e^{-\Delta\omega z} & & & & & \\ & & e^{-2\Delta\omega z} & & & & \\ & & & \ddots & & & \\ & & & & e^{-\Omega z} & & \\ & & & & & e^{(n-1)\Delta\omega z} & \\ & & & & & & \ddots \\ & & & & & & & e^{\Delta\omega z} \end{bmatrix}. \tag{8}$$

To illustrate the signal vectors at adjacent nodes, we assume $H = I$, i.e., the transmission line is a perfect conductor, or the response of the branched network is an impulse. Then, as in equation (8), we may have at time t,

$$\hat{v}_i(t) = \begin{bmatrix} x_i(t) \\ x_i(t-T) \\ x_i(t-2T) \\ \vdots \\ x_i(t-(n-1)T) \end{bmatrix} \quad (9)$$

and

$$\hat{v}_j(t) = \begin{bmatrix} x_j(t) \\ x_j(t-T) \\ x_j(t-2T) \\ \vdots \\ x_j(t-(n-1)T) \end{bmatrix}. \quad (10)$$

As $H = I$, we have,

$$v_j(t) = \hat{v}_i(t-T). \quad (11)$$

In fact, when H is flat in the frequency domain, there is no information gained by keeping the higher frequency resolution. So, we can set $n = 1$, and when we apply the argument of equation (11) to all the other nodes, we will have equation (3), just as it should be.

Now, let the Fourier Transform of $\hat{v}_i(t)$ and $\hat{v}_j(t)$ be $\hat{V}_i(t)$ and $\hat{V}_j(t)$, respectively. Then for a transmission line with H as in equation (4),

$$\hat{V}_j(t) = H\hat{V}_i(t-T) \ . \quad (12)$$

For this application, it is easier to apply this in the frequency domain rather than in the time domain.

We can further compact our notation by combining the signal vectors at individual nodes into a state vector where each of its entries is a vector itself. The state vector is defined as,

$$\bar{V}_t = \begin{bmatrix} \hat{V}_1^T(t) \\ \hat{V}_2^T(t) \\ \vdots \\ \hat{V}_i^T(t) \\ \hat{V}_j^T(t) \\ \vdots \end{bmatrix} \quad (13)$$

where T indicates a vector transpose.

A is the transition matrix telling us the transition properties between the adjacent nodes, and it can be applied to the frequency domain as well. We have to be aware that the entries of A are now applied to the entries of the state, which are vectors. Combining equations (3), (12), and (13) we have,

$$\bar{V}_t = AH\bar{V}_{t-T} \quad (14)$$

The simulated TDR response of RG58 cables in the branched structure shown in Fig. 3 is presented in Fig. 6.

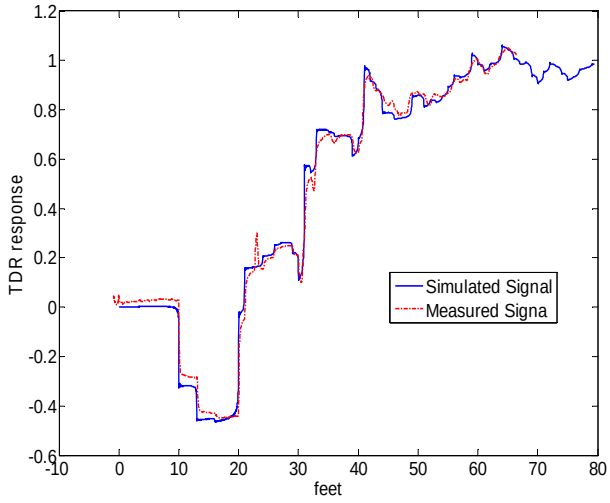

Fig. 6. Comparison of simulated response with transmission line model added and measured TDR response.

From Fig. 6, we observe that by adding the complex propagation constant, the simulation result is improved. Additional differences between the simulated and measured system may be due to variation between the ideal and actual characteristic impedance of the cable and impedance of the connections that was not accounted for in the model.

V. HIGH SPEED REALIZATION

Implementation of equation (14) can be further speeded up if the network consists of a uniform wire type, and the TDR input signal is used as in the previous examples.

Some basic mathematical properties can be used to facilitate further discussion. Let the network be represented by transfer function $h(\cdot)$, which is linear. Then an input signal $f(\cdot)$ will generate an output response of $y(t) = h * f(t)$. In the above expression, * indicates the convolution operation which is defined as,

$$\begin{aligned} y(t) &= h * f(t) \\ &= \int h(\tau) f(t-\tau) d\tau. \end{aligned} \quad (15)$$

This may be represented graphically as in Fig. 7.

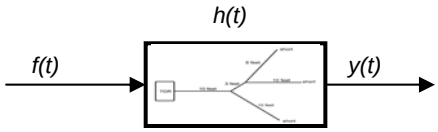

Fig. 7. System representation of wire network.

From equation (15), we have,

$$\begin{aligned}\frac{d}{dt}h*f(t) &= \frac{d}{dt}\int h(\tau)f(t-\tau)d\tau \\ &= \int h(\tau)\frac{d}{dt}[f(t-\tau)]d\tau \\ &= \int h(\tau)f'(t-\tau)d\tau \\ &= h*f'(t) \\ \Rightarrow \quad h*f(t) &= h*f'(t)dt \ .\end{aligned} \tag{16}$$

Since the TDR signal, *f(t)*, is a step function at *0*, then *f'(t)* becomes a delta function *δ(t)*. Then, from equation (3) without considering the filtering effect, the impulse response of the wire network in Fig. 3 is a train of impulses with peaks corresponding to junctions of impedance mismatches and their multiple reflections. Figure 8 shows this train of impulses.

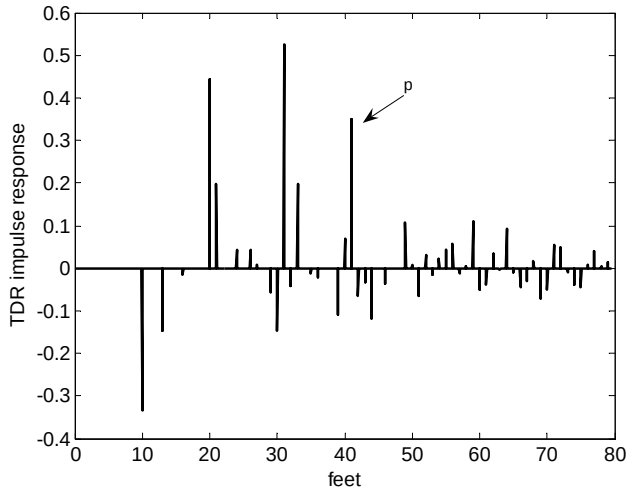

Fig. 8. Impulse response of the wire network in Fig. 3.

Considering a particular peak, p_k, from the train of impulses as marked in Fig. 6, which has a magnitude of A_k and a time delay of T_k gives,

$$p_k = A_k\delta(t-T_k)\,. \tag{17}$$

There are two important aspects of this derivation. First, since n(t) is linear, the filtering effect of the wire can be considered for independent peaks. Second, no matter how many junctions cause multiple reflections of p_k, the total distance of its travel can be determined by delay T_k . The filtering effect p_k will experience depends only on the length of wire it travels through. This filter is denoted by $h_{T_k}(t)$, and the filtered version, of p_k becomes,

$$p_k = A_k h_{T_k}(t-T_k)\,. \tag{18}$$

Summarizing the above two aspects, we have,

$$y'(t) = \sum_i A_i h_i(t-T_i)\,. \tag{19}$$

In its discrete version, equation (19) becomes,

$$y'[n] = \sum_i A_i h_i[n-m_i] \tag{20}$$

where the sample rate is the same as in equations (6) and (7), and m_i is the number of samples for the signal to travel in T_i. So from equation (8), the Fourier transform of $h_{m_i}[n-m_i]$ becomes,

$$H_{m_i} = \Lambda(He)^{m_i} \tag{21}$$

where

$$\Lambda = \begin{bmatrix} 1 & & & & & & \\ & e^{-j2\pi\Delta\omega} & & & & & \\ & & e^{-j4\pi\Delta\omega} & & & & \\ & & & \ddots & & & \\ & & & & e^{-j2\pi\Omega} & & \\ & & & & & e^{j2\pi(n-1)\Delta\omega} & \\ & & & & & & \ddots \\ & & & & & & & e^{j2\pi\Delta\omega} \end{bmatrix}.$$

Then equation (19) may be written as,

$$Y'[k] = \Lambda\sum_i A_i(eH)^{m_i}\bar{1} \tag{22}$$

where $\bar{1}$ is a unit vector. Then *y'*[n] is found from the inverse Fourier transform of equation (22). Then from equation (16), *y*[n] can be obtained by integration. Figure 9 shows the filtered impulse response of the wire network in Fig. 3 with equation (22), and its integral. The integral *y*[n] is the same as the result shown in Fig. 6.

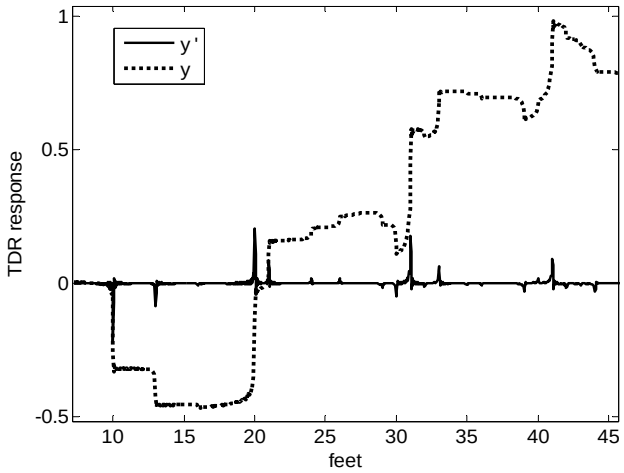

Fig. 9. Impulse response of the wire network in Fig. 3 filtered as equation (24) and its integral.

VI. CONCLUSION

This paper has described a simple and effective method of analyzing time domain fields on ideal or non-ideal branched networks of wires. The method can be used to evaluate both reflectometry signatures and communication systems made up of branched wire networks. It could also be adapted to a grid of wires such as may be used in interconnected sensor networks. Use of the frequency-dependent attenuation constant provided significantly better agreement between the ideal and measured responses.

REFERENCES

[1] L. N. Drowsy, *Modern Transmission Line Theory and Applications*, John Wiley and Sons, Inc., 1997.

[2] C. R. Paul and R. J. W. McKnight, "Prediction of crosstalk involving twisted pairs of wires – Part I: A transmission line model for twisted-wire pairs," *IEEE Trans. On EMC*, vol. 21, no. 2, May 1979.

[3] T. Bostoen, P. Boets, M. Zekri, L. Van Biesen, T. Pollet, and D. Rabijins, "Estimation of the transfer function of a subscriber loop by means of a one-port scattering parameter measurement at the central office," *IEEE Journal on Selected Areas in Communications*, vol. 20, no. 5, June 2002.

[4] P. Lots, Powerline communications, in Proc. TI KVIV Workshop on the use of powerlines for non-power applications, Antwerpen, Belgium, December 9, 1998.

[5] C. Lo and C. Furse, "Noise domain reflectometry for wire fault location," *IEEE Trans. EMC*, February 2005.

[6] J.-F. Mao and Z.-F. Li, "Analysis of the time response of multiconducctor transmission lines with frequency-dependent losses by the method of convolution-characteristics," *IEEE Trans. MTT*, vol. 40, no. 4, pp. 637-644, April 1992.

[7] A. Djordjevic and T. K. Sarkar, "Anlaysis of time response of l ossy multiconductor transmission line networks," *IEEE Trans. MTT*, vol. 35, no. 10, pp. 898-908, October 1987.

[8] G. Antonini, G. Ferri, "A new approach for closed-form transient analysis of multiconductor transmission lines," *IEEE Trans. EMC*, vol. 46, no. 4, pp. 529-543, November 2004.

[9] L. Gruner, "Multiconductor transmission lines and the Green's matrix," *IEEE Trans. MTT*, pp. 837-839, Septemper 1974.

[10] F. T. Ulaby, *Fundamentals of Applied Electromagnetics*, Prentice Hall, 2004.

[11] R. Parakh, "The invisible fray: A formal assessment of the ability of reflectometry to locate frays on aircraft wiring," *Master's thesis*, University of Utah, Salt Lake City, Utah, 2004.

Analysis and Design of a Planar Multilayered FSS with Arbitrary Incidence

[1]L. Latrach, [1]N. Sboui, [1]A. Gharsallah, [1]A. Gharbi, and [2]H. Baudrand

[1] Laboratoire d'Electronique Département de physique Faculté des sciences de Tunis, 2092 El Manar Tunisia
E-mail : noureddine.sboui@fst.rnu.tn
[2] Laboratoire d'Electronique EN SEEIHT de Toulouse France

Abstract – A rigorous technique based on the transverse Wave Concept Iterative Procedure (WCIP) and a Fast Mode Transformation (FMT) is used to analyze the Frequency Selective Surface (FSS). These structures are used as filters and reflector antenna as well as deep-space exploration for multi-frequency operations. In order to initialize the iterative procedure, an incident wave is defined in spatial domain with arbitrary angle of incidence. The numerical complexity is studied and compared to the classical MoM. The good agreement between simulated and published data justifies the design procedure.

Keywords: Arbitrary incidence, single-layer, multilayered, and 2D-FFT algorithm.

I. INTRODUCTION

Frequency Selective Surface structures have played an important role in the recent development of antennas and microwave device technology. They are used as spatial filters [1], artificial surfaces [2] and a deep- space exploration for multi-frequency operations [3]. Typically, FSS structures consist in two-dimensional periodic resonant element supported by one or multilayer of dielectrics. Performances depend on their substrate characteristics, element type, dimensions and the spacing between elements.

To design the FSS arrays, a number of analytical and numerical techniques has been developed. One of the most popular is the Method of Moments (MoM) and its derivatives [4-6]. Yet, one can compute the unknown current distribution on the FSS screens in one-step. Then the small dimensions of the circuit cause some problems in result precisions thus coupling conditions between the different elements must be taken into account. The Mode Expansion Method [7] and the Spectral-Domain Method [8] have been developed to analyze the FSS structures. However, the efficiency, memory consumption and time requirement usually make these methods unsuitable for optimization. For its simplicity, the Equivalent- Circuit Method is used to design the FSS structures [9-10], but its application is limited only for known simple forms [9].

During the last few years, the FMT-WCIP method has been applied in wide variety of microwave structures [11-13]. It consists in successive reflections between the FSS screens and their two sides. It has also an alternative behavior between space and spectral domains. There are several procedures to change wave domains. In [14], The Galerkin technique is used. In each stage of analysis, the transformation passage from spatial to spectral (and vice versa) is long. As in [11-13], we combine the wave concept with the 2D-FFT algorithm to change the domain. The use of the 2D-FFT algorithm is required to mesh the circuit plane into 2D small rectangular cells. Hence, the boundary conditions are satisfied at each cell. By using the 2D-FFT algorithm, a high computational speed can be achieved. This method is simple since it involves neither basic functions nor matrix inversion. Thus, it not only over comes the limitation of the above methods, but it is also suitable for general structure. In [11-13], the circuit under studied is deposed on one dielectric layer surrounded by four perfect electric walls, and is defined in the spatial domain. The source excitation consists in an electric filed E0 placed between the circuit and an electric wall of the cavity. In reference [15], the WCIP is used to study a stratified isotropic/anisotropic FSS structure with a normal incidence angle.

The purpose of this paper is to extend the Wave Concept Iterative Process method WCIP to the analysis of a Frequency Selective Surfaces FSS structures with an arbitrary incident angle in the multilayer configuration. The numerical complexity of the iterative procedure is studied and compared to the classical MoM. Two different examples are studied; single simple layer and multilayer. For the two cases, our simulated results are validated with those of other methods and measurements.

II. THEORY

Let us consider a periodic arbitrary multilayer structure, as shown in Fig. 1. Figure 2 shows the unit cell at the Ω_i interface. This interface can support the circuit and includes two sub-domains Metal M_i and Dielectric D_i. We suppose that the electromagnetic field is known

on all points of the interface plane. The solution of the problem has to satisfy the following boundary conditions,

$$\begin{cases} E_{T\,i} = E_{T\,(i+1)} = 0 \quad On \quad M_i \\ H_T = H_{T\,i} + H_{T\,(i+1)} \quad On \quad D_i \ . \end{cases} \tag{1}$$

In the last equation, E_{Ti} and $E_{T(i+1)}$ are respectively, the spatial tangential components of the electric field at medium *i* and *(i+1)* with H_{Ti} and $H_{T(i+1)}$ as their corresponding magnetic fields.

The wave concept is introduced by writing the tangential electric and magnetic fields (E_{Ti},H_{Ti}) in terms of incident (A_i) and reflected (B_i) waves, as shown in Fig. 3 [13]. It leads to the following equation,

$$\begin{vmatrix} A_i \\ B_i \end{vmatrix} = \frac{1}{2\sqrt{y_{0i}}} \begin{vmatrix} y_{0i} & 1 \\ y_{0i} & -1 \end{vmatrix} \begin{vmatrix} E_{T\,i} \\ H_{T\,i} \wedge n_i \end{vmatrix}. \tag{2}$$

The symbol n_i is the unit vector orthogonal to Ω_i giving the direction of the incident and reflected waves and y_{0i} is an intrinsic admittance characterizing the medium. It is often chosen as $\sqrt{\varepsilon_0 \varepsilon_{ri} / \mu_0}$ in which ε_0, μ_0 and ε_{ri} are respectively, the permittivity and permeability of the vaccum and the relative permittivity of the medium 'i'.

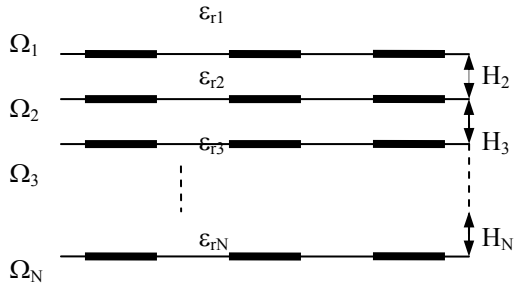

Fig. 1. General periodic multilayer structure.

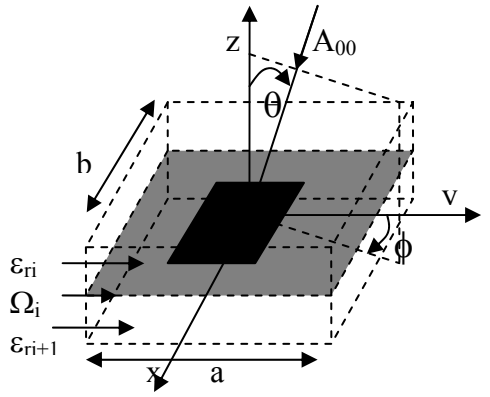

Fig. 2. Unit cell of the periodic structure with arbitrary incidence A_{00}.

This last equation allows us to write the boundary conditions given by equation (1) as the following general spatial equation,

$$\begin{vmatrix} B_i \\ B_i^{'} \end{vmatrix} = \left\{ \underbrace{\left[\hat{S}_{M\,i} \right] + \left[\hat{S}_{D\,i} \right]}_{[\hat{S}_i]} \right\} \cdot \begin{vmatrix} A_i \\ A_i^{'} \end{vmatrix} \tag{3}$$

$$\left[\hat{S}_{Di} \right] = \frac{\hat{H}_{Di}}{1+n_{0i}^2} \begin{vmatrix} 1-n_{0i}^2 & 2n_{0i} \\ 2n_{0i} & n_{0i}^2 - 1 \end{vmatrix},$$

$$n_{0i} = \sqrt{\frac{y_{0i+1}}{y_{0i}}}, \quad \left[\hat{S}_{M\,i} \right] = \begin{vmatrix} -1 & 0 \\ 0 & -1 \end{vmatrix}.$$

and $$\hat{H}_{\pi} = \begin{cases} 1 \ \ if \ \ \pi = M_i \ \ or \ \ D_i \\ 0 \ \ else \ where \end{cases}$$

Hence, we deduce the global spatial equation relating the reflected waves to the incident ones on all the interfaces,

$$\left\{ \begin{vmatrix} B_1 \\ B_1^{'} \\ B_2 \\ B_2^{'} \\ \vdots \\ B_i \\ B_i^{'} \\ \vdots \\ B_N \\ B_N^{'} \end{vmatrix} = \begin{vmatrix} [S_1] & & & & & & \\ & [S_2] & & & & & \\ & & \ddots & & & & \\ & & & [S_i] & & & \\ & & & & \ddots & & \\ & & & & & [S_N] & \end{vmatrix} \begin{vmatrix} A_1 \\ A_1^{'} \\ A_2 \\ A_2^{'} \\ \vdots \\ A_i \\ A_i^{'} \\ \vdots \\ A_N \\ A_N^{'} \end{vmatrix} \right\}_{x,y} . \tag{4}$$

Between two consecutive interfaces (*i* and *i+1* for example), the waves are defined in the spectral domain (TE and TM modes), and are led by the following spectral equation, Fig. 3.

$$\left\{ \begin{vmatrix} A_i^{'} \\ A_{i+1} \end{vmatrix} = \left[L_{i+1} \right] \begin{vmatrix} B_i^{'} \\ B_{i+1} \end{vmatrix} \right\}_{TE,TM}, \tag{5}$$

$$\left[L_{i+1} \right]_{\alpha} = \begin{bmatrix} l_{1\alpha} & l_{2\alpha} \\ l_{2\alpha} & l_{1\alpha} \end{bmatrix}$$

and α= TE or TM.

For the TE_{mn} or TM_{mn} mode, the elements of the matrix L_i become $L_{1mn\alpha}$ and $L_{2mn\alpha}$, which they have the following partitioned form,

$$l_{1mn\alpha}=\frac{\left(Z_{mni\alpha}^2-z_{0i}^2\right)\sinh\left(\gamma_{mni}h_i\right)}{\Delta_c} \text{ and } l_{2mn\alpha}=\frac{2Z_{mni\alpha}z_{0i}}{\Delta_c}$$

where: $Z_{mniTE}=\dfrac{j\omega\mu_0}{\gamma_{mni}}$, $Z_{mniTM}=\dfrac{\gamma_{mni}}{j\omega\varepsilon_0\varepsilon_{ri}}$,

$$\Delta_c=2Z_{mni\alpha}z_{0i}\cosh\left(\gamma_{mni}h_i\right)+\left(Z_{mni\alpha}+z_{0i}^2\right)\sinh\left(\gamma_{mni}h_i\right)$$

$$\gamma_{mni}=\sqrt{\beta_{xm}^2+\beta_{yn}^2-k_0^2\varepsilon_{ri}}\,,\ k_0=\omega\sqrt{\mu_0\varepsilon_0}\,,\omega=2\pi\frac{c}{\lambda}$$

$$\beta_{xm}=\beta_x+\frac{2m\pi}{a}\ \beta_{yn}=\beta_y+\frac{2n\pi}{b},$$

$$\beta_x=\omega\sqrt{\varepsilon_{r1}\mu_{r1}}\sqrt{\varepsilon_0\mu_0}\sin\theta\cos\phi\ ,$$

$$\beta_y=\omega\sqrt{\varepsilon_{r1}\mu_{r1}}\sqrt{\varepsilon_0\mu_0}\sin\phi\cos\theta\,.$$

a and b are respectively the periodicity along (ox) and (oy), θ and φ define the angle of incidence.

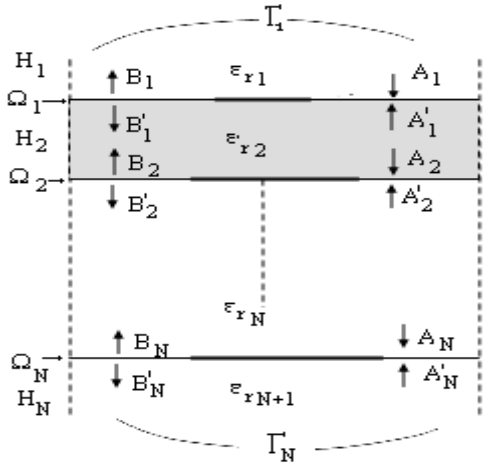

Fig. 3. Definition of waves for the multilayer structure.

On the upper and lower parts of the multilayer structure (medium 1 and medium N), the higher-order modes are shunted by their reactive impedance Z_i, which relates the tangential electric field E_{Ti} to the total current density J_i. Consequently, we obtain,

$$E_{Ti}= Z_i J_i\,. \tag{6}$$

Thus, with equation (2), we can define a reflection operator in modes. Hence, we deduce the reflected spectral wave A_i from the incident spectral B_i as,

$$\left\{A_i=\hat{\Gamma}_i\,B_i\right\}_\alpha \tag{7}$$

$\hat{\Gamma}_{i\alpha}=\dfrac{Z_{mni\alpha}-z_{0i}}{Z_{mni\alpha}+z_{0i}}$, α=TE or TM and i=1 ,or N.

Consequently, with equations (5) and (7), we deduce that the global spectral equation relates the diffracted wave A_i to incident wave B_i in the spectral domain.

$$\left\{\begin{vmatrix}A_1\\A_1'\\A_2\\\vdots\\A_{i-1}'\\A_i\\\vdots\\A_n'\end{vmatrix}=\begin{vmatrix}\Gamma_1 & & & & & & \\ & [L_2] & & & & & \\ & & \ddots & & & & \\ & & & [L_i] & & & \\ & & & & \ddots & & \\ & & & & & \Gamma_N\end{vmatrix}\begin{vmatrix}B_1\\B_1'\\B_2\\\vdots\\B_{i-1}'\\B_i\\\vdots\\B_n'\end{vmatrix}+\begin{Bmatrix}A_{00}\\0\\0\\\\0\\0\\\\0\end{Bmatrix}\right\}_\alpha \tag{8}$$

In the above equation, we have included the excitation wave $A_{00}=\begin{vmatrix}A_{ox}\\A_{oy}\end{vmatrix}$. A_{00} is defined in the spectral domain and has the following expression:

For TE polarization:

$$\begin{cases}A_{0x}=\dfrac{1}{2\sqrt{Z_{oi}}}\dfrac{\beta_y}{\sqrt{|\beta_x|^2+|\beta_y|^2}}\dfrac{1}{\sqrt{ab}}e^{-j(\beta_x x+\beta_y y)}\\ A_{0y}=\dfrac{-1}{2\sqrt{Z_{oi}}}\dfrac{\beta_x}{\sqrt{|\beta_x|^2+|\beta_y|^2}}\dfrac{1}{\sqrt{ab}}e^{-j(\beta_x x+\beta_y y)}\end{cases}. \tag{9}$$

For TM polarization:

$$\begin{cases}A_{0x}=\dfrac{-1}{2\sqrt{Z_{oi}}}\dfrac{\beta_x}{\sqrt{|\beta_x|^2+|\beta_y|^2}}\dfrac{1}{\sqrt{ab}}e^{-j(\beta_x x+\beta_y y)}\\ A_{0y}=\dfrac{1}{2\sqrt{Z_{oi}}}\dfrac{\beta_y}{\sqrt{|\beta_x|^2+|\beta_y|^2}}\dfrac{1}{\sqrt{ab}}e^{-j(\beta_x x+\beta_y y)}\end{cases}. \tag{10}$$

Equations (9) and (10) are derived from the characteristic functions of periodic waveguide.

The implementation of the iterative procedure consists in establishing a recursive relationship between the two spatial and spectral equations, respectively equations (4) and (8).

In addition, this iterative procedure has an alternative behavior between the spatial (on the circuit) and spectral domain (in the two sides). At each iteration, it is necessary to change the type of domain. In the present study, we combine the Wave Concept with the 2D-FFT algorithm, which is called Fast Mode Transformation FMT [15]. The iterative procedure is summarized in Fig. 4. A successive set of iteration is considered to determine a relationship between (k) and (k+1) interaction waves. This is illustrated in the following way.

First, we take the spectral equation (8) and deduce the spectral incident waves $(A_i)_{TE,\,TM}$. In the same iteration, we take the IFMT transformation (Inverse Fast Mode Transformation) to calculate the spatial waves, this transformation is expressed as,

$$\left|\begin{matrix}A_x\\A_y\end{matrix}\right|^k = [T]^{-1}.\left|\begin{matrix}IFFT_{2D}(A_{TE})\\IFFT_{2D}(A_{TM})\end{matrix}\right|^k \qquad (11)$$

The matrix [T] is the transformation matrix from the classical 2D-FFT to 2D-FFT in modes, which is derived from periodic waveguide chrematistic functions and has the following partitioned form,

$$[T] = \left|\begin{matrix}N_{ymn} & -N_{xmn}\\N_{xmn} & N_{ymn}\end{matrix}\right| \qquad (12)$$

with $N_{xmn} = \dfrac{1}{\sqrt{ab}}.\dfrac{\beta_{xm}}{\sqrt{|\beta_{xm}|^2+|\beta_{yn}|^2}}$

and $N_{ymn} = \dfrac{1}{\sqrt{ab}}.\dfrac{\beta_{yn}}{\sqrt{|\beta_{xm}|^2+|\beta_{yn}|^2}}$

a, b, β_{xm} and β_{yn} are defined in equation (5).

The second step consists in taking the spatial equation (4) and deducing the reflected spatial wave (Bi)x,y from the incident (Ai)x,y.

In the third step, we come back to the spectral domain using the direct FMT. This should be done as follows,

$$\left|\begin{matrix}B_{TE}\\B_{TM}\end{matrix}\right|^{k+1} = [T].\left|\begin{matrix}FFT_{2D}(B_X(x,y))\\FFT_{2D}(B_Y(x,y))\end{matrix}\right|^k \qquad (13)$$

Finally, we calculate the scattered matrix parameters, and then we test the convergence and return to the fist step if the convergence is not obtained.

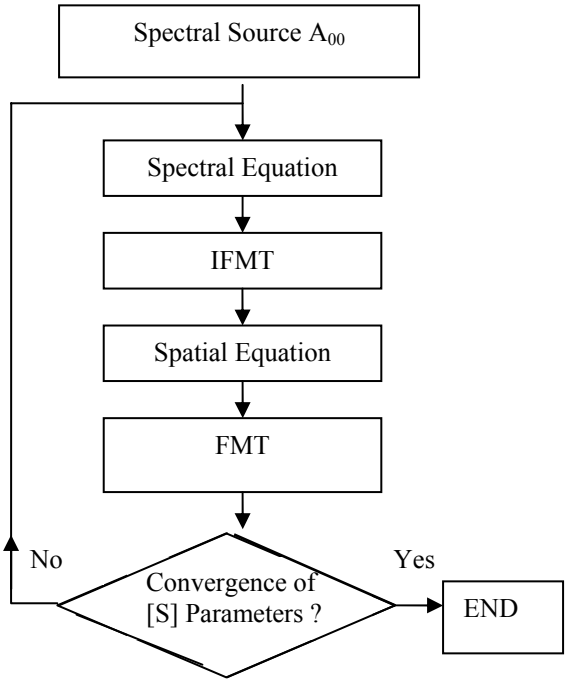

Fig. 4. Schematic description of the iterative process.

III. APPLICATIONS

To evaluate the numerical complexity procedure described in section II, we will make a comparison with the Method of Moments MoM. In terms of the WCIP method, the numerical complexity depends on the interfaces number and the spatial mesh of the circuit plane, whereas in the classical Method of Moments MoM, this complexity depends on the rate of metallization [16]. In order to compare the numerical complexity of these two methods, let us consider Q as the number of cells meshing the whole interface and Q_m the number of cells on the metallic domain. Q_m corresponds to the number of rooftops in the MoM. For the WCIP, the total number of operations for T iterations is $Oper_{WCIP} = 4QT\left(1+3\log_2 Q\right)$ and for the MoM is $Oper_{MoM} = Q^3/3R^3$ where $R = Q/Q_m$ [12]. Figure 5 shows the evolution of the operation numbers as the metallic rate function. The intersection point 'M' of the two curves corresponds to 30% of metallization and 0.9011 107 operations, is calculated with 32x32 cells and 200 iterations. We see that the WCIP is very speedy if the metallization is as large as in the FSS structures.

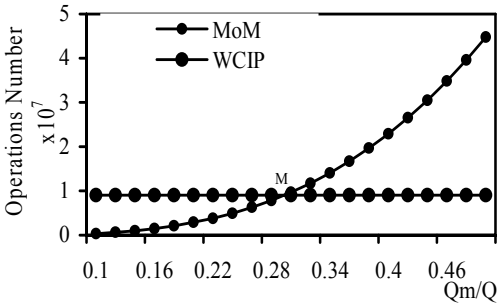

Fig. 5. Comparison in number of operations.

The convergence of the resonance frequency as mesh size thinness Δ is studied. Figure 6 shows that before the convergence, the resonant frequency increases if Δ decreases. At the convergence, the resonance frequency is about 10.3 GHz, is obtained from Δ=0.2 mm. In this study, the source excitation used in this application is the fundamental TM mode with normal incidence *(θ = φ = 0)*.

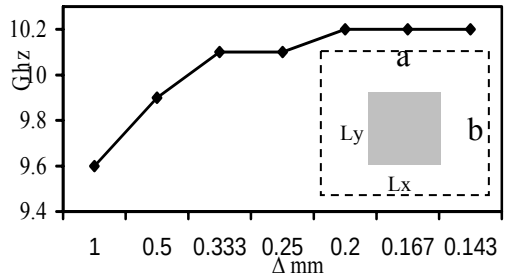

Fig. 6. Convergence of resonance frequency as function of mesh size thinness Δ where: h = 3mm, ε_r =3.5, a = b = 20 mm and $L_x = L_y$ =10 mm.

In order to validate our method, we consider again the structure of Fig. 6. The results of our method are compared to those calculated with Method of Line [17] and depicted in Fig. 7. In the two cases, a good agreement is obtained between results.

The second example consists in studying two layers structure as shown in Fig. 8. A TM source with arbitrary incidence is considered in this application.

The physical parameters are:

$$\begin{cases} a = 0.5\lambda_0, \quad b = 0.5\lambda_0 \\ \text{Plate}: L_x^P = 0.131\lambda_0, \quad L_y^P = 0.15\lambda_0 \\ \text{Slote}: L_x^f = 0.001\lambda_0, \quad L_y^f = 0.115\lambda_0 \\ f = 15\text{GHz}, \; h = 0.002\lambda_0, \; \varepsilon_r = 12.8 \end{cases}$$

Three cases of ϕ are studied: E-plane ($\phi = 0$), D-plane ($\phi = 45^o$)and H-plane ($\phi = 90^o$). In the case of E-plane the evolution of power reflection coefficient as function of θ is plotted in Fig. 9. At all range of θ, a good agreement is observed between our results and measured data [17], a maximum discrepancy is less than 2 %. The total reflection is observed for $\theta = 83^o$.

In the two other cases [D-plane] and [H-plane], the power reflection variation is plotted, respectively in Figs. 10 and 11. Only measured data [18] presents a total reflection at the predicted angle. In our simulation, the total reflection is 0.73 in D-plane and ≈ 0.865 in H-plane. The discrepancy is due to mode excitation. In practice, [17], the excitation is realized by coaxial cable. Then, a field of symmetric cylindrical is produced and the TM mode is coupled at all directions.

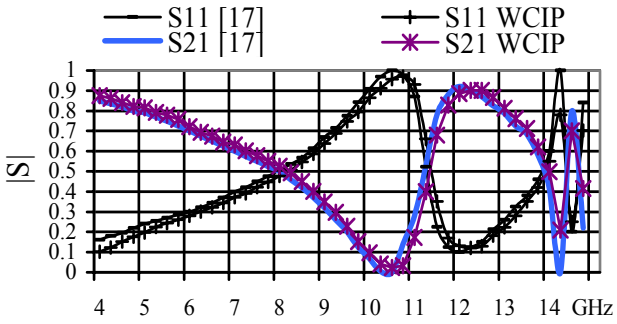

Fig. 7. Power coefficients S_{11}^2 and S_{21}^2as function of frequency where: h = 3mm, ε_r=3.5. a = b = 20 mm and $L_x = L_y$ =10mm.

a: Side View

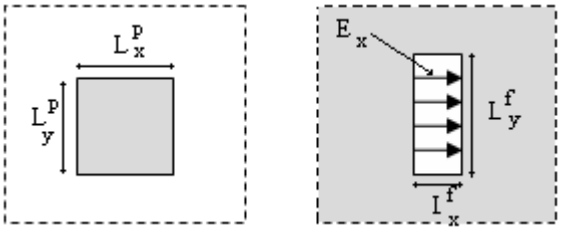

b: Interface Ω_1 c: Interface Ω_2

Fig. 8. Slot coupled periodic antenna.

IV. CONCLUSION

In this paper, the transverse wave concept iterative procedure FMT-WCIP is proposed for the analysis of the frequency selective surface (FSS) with arbitrary angle of excitation. The numerical complexity is studied and compared to the classical MoM. As a result, a minimum computation time is required and the number of operations is reduced by using the FMT based on the 2D-

FFT algorithm. The comparison between the simulation and the measurement results has proved the efficiency of our proposed design procedure of a simple and multilayer FSS.

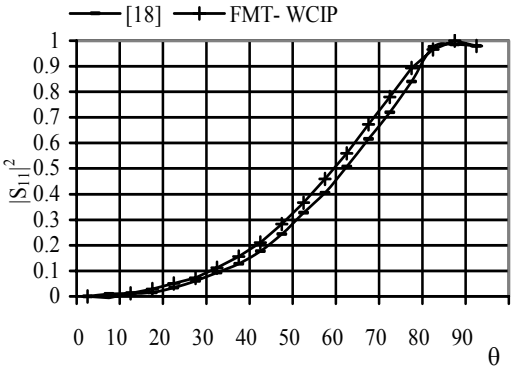

Fig. 9. Amplitude of power reflection coefficient versus θ for E-plane.

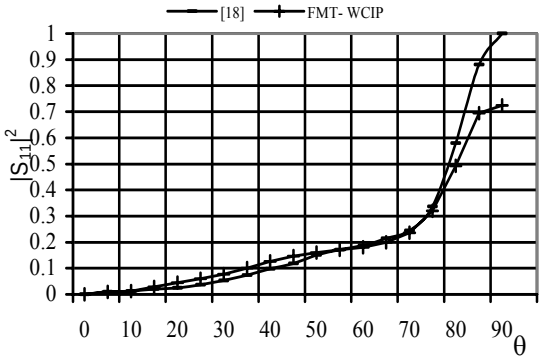

Fig. 10. Amplitude of power reflection coefficient versus θ for D-plane.

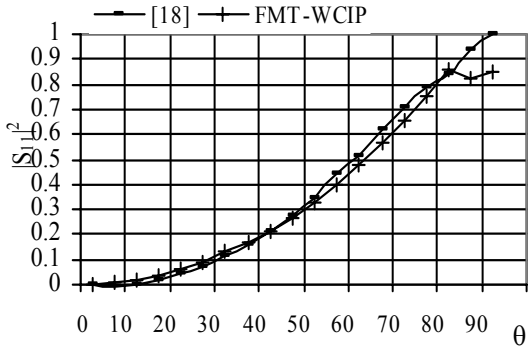

Fig. 11. Amplitude of power reflection coefficient versus θ for H-plane.

REFERENCES

[1] B. A. Munk, *Frequency Selective Surfaces: Theory and Design*, Wiley, New York, 2000.

[2] D. J. D. H. Werver, A. Monorchio, L. Lanuzza, and M. J. Wilhelm, "The design synthesis of multi-band artificial magnetic conductors using high impedance frequency selective surfaces," *IEEE Trans. Antennas Propag.,* vol. 53, no.1, pp. 8-17, Jan. 2005.

[3] D. Hokim and J. Ick Choi, "Design of a multi-band frequency selective surface," *ETRI Journal*, vol. 28 no. 4, Aug. 2006.

[4] N. Bliznyuk and N. Engheta, "Numerical study of polarization dependant focusing for a bi-layer planar FSS reflective at millimeter wave length," *Microwave and Optical Technology Letters,* vol. 40, no. 5, pp. 361-365, Mar. 2004.

[5] A. K. Bhattacharyya, "A numerical model for multilayered microstrip phased-array antennas," *IEEE Trans. Antennas Propag*, vol. 44, no. 10, pp. 1386–1393, Oct. 1996.

[6] M. Bozzi, L. Perregrini, J. Weinzierl, and C. Winnewisser, "Efficient analysis of quasi-optical filters by a hybrid MoM/BI-RME method*," IEEE Trans. Antennas Propag*., vol. 49, no. 7, pp. 1054–1064, Jul. 2001.

[7] G. Zarrillo and K. Aguiar, "Closed-form low frequency solutions for electromagnetic waves through a frequency selective surfaces," *IEEE Trans. Antennas Propag.*, vol. 35, pp. 1406–1417, Dec. 1987.

[8] J. Jin and J. L. Volakis, "Electromagnetic scattering by a perfectly conducting patch array on a dielectric slab," *IEEE Trans. Antennas Propag.*, vol. 38, no. 4, pp. 556–563, 1990.

[9] Zhi Liang Wang, Kozo Hashimoto, Naoki Shinohara, and Hiroshi Matsumoto, "Frequency-Selective Surface for Microwave Power Transmission*," IEEE Trans. MTT,* vol. 47, no.10, Oct. 1999.

[10] R. J. Langley and E. A. Parker, "Equivalent circuit model for arrays of square loops," *Electron. Letters*, vol. 18, pp. 294–296, 1983.

[11] N. Sboui, A. Gharsallah, A. Gharbi, and H. Baudrand, "Analysis of double loop meander line by using iterative process," *Microwave and Optical Technology Letters,* vol. 26, pp. 396-399, June 2000.

[12] N. Sboui, A. Gharsallah, H. Baudrand, and A. Gharbi, "Design and modeling of RF MEMS switch by reducing the number of interfaces*," Microwave and Optical Technology Letters*, vol. 4913, no. 5, pp. 1166-1170, May 2007.

[13] N. Sboui, A. Gharsallah, A. Gharbi, and H. Baudrand, "Global modeling of microwave active circuits by an efficient iterative procedure," *IEE Proc. Microw. Antennas Propag.* vol. 148, no. 3, pp. 209-212, June 2001.

[14] M. Azizi, M. Boussouis, H. Aubert, and H. Baudrand, "A Three-dimensional Analysis of Planar Discontinuities by an Iterative Method," *Microwave and Optical Technology Letters*, vol. 13, no. 6, pp. 372-376, Dec. 1996.

[15] M. Tiataouine, A. G. Neto, H. Baudrand, and F. Djahli, "Analysis of frequency selective surface on isotropic/anisotropic layers using WCIP method," *ETRI Journal,* vol. 29, no. 1, Feb. 2007.

[16] R. Mittra, H. Chan, and T. Cwik, "Techniques for analysis frequency selective surfaces-A Review," *Proceeding of the IEEE,* vol. 76, no. 12, Dec. 1988.

[17] E. Choinière and J. J. Laurin," Modeling of planar multilayer periodic arrays using the method of lines," *ACES Journal,* vol. 17, no. 2, July 2002.

[18] D. M. Pozar and D. H. Schaubert, "Analysis of an infinite array of rectangular microstrip patches with idealized probe feeds," *IEEE Trans. Antennas Propag.,* vol. 32, no. 10, pp. 1101–1107, Oct. 1981.

On The Optimum Directivity of Dipole Arrays Considering Mutual Coupling

V. N. S. Kalaga and M. Hamid

Department of Electrical Engineering, University of South Alabama
Mobile, Alabama, 36688, U.S.A
Email: kalagavnsrinu@yahoo.com

Abstract – Linear half-wave dipole array is optimized on the basis of the directivity considering mutual coupling between the array elements, in horizontal, vertical and three dimensional field patterns. Simulated results for the value of directivity without and with mutual coupling are presented in both broad-side and end-fire configurations, for different number of elements in the array. It is observed that mutual coupling can enhance as well as degrade the overall directivity of the array.

Keywords: Half wave dipole, directivity, broad side array, end fire array, and mutual coupling.

I. INTRODUCTION

Mutual coupling is a phenomenon that depends upon the adjacent array elements and greatly affects the characteristics of an antenna array. Mutual coupling, expressions for mutual impedance and procedure for obtaining currents after mutual coupling in a linear dipole array are discussed in [1-4]. An advanced method of measuring mutual impedance easily is given in [5]. Modeling and estimation of mutual coupling in uniform linear array of dipoles is presented in [6]. Method of computing mutual impedance conducive to digital computer application is given in [7]. Mutual impedance calculated considering scattering from the individual elements is given in [8] and mutual impedance calculated using Finite Difference Method (FDM) is discussed in [9]. Fundamentals of linear arrays can be found in [2, 3, 10]. The optimum directivity of an antenna or its array is given in [11, 12], and approximate directivity expressions for a linear array of uniformly spaced elements are discussed in [13, 14] when the amplitudes for all the array elements are real.

In this paper the directivity of the linear dipole array is improved taking mutual coupling into account rather than trying to compensate the effect. Linear array design by compensating mutual coupling phenomenon is discussed in [15, 16]. Simple expressions to calculate the directivity are presented for a linear array of any large number of identical elements with constant inter element spacing, where elements can have different complex amplitude coefficients. Optimum directivity values and corresponding graphs with respect to the separation between the elements are given, with mutual coupling compared to the case of without mutual coupling for the three amplitude configurations uniform, Dolph-Tchebyscheff and binomial, obtained by simulating in Matlab. The results show that the factors such as amplitudes, phase difference between adjacent elements and total number of elements in the array together greatly influence the effect of mutual coupling on the array directivity. Directivity values for the uniform three dimensional field pattern without mutual coupling for the case of half-wave dipole arrays in both broad-side and end-fire directions are validated by [11, 17], whereas mutual coupled currents are verified with some of the results in [15, 18]. Effect of mutual coupling on the maximum directivity of the array by changing the dipole length [2] from 0.5 λ to 1.5 λ is also given by observing the change in near and far field regions, resulting from the change in the dipole length.

Consider an array of N identical elements with any amplitude and phase excitation, placed along the x axis, symmetrically with respect to origin, as shown in Fig. 1 with constant separation between adjacent elements as d.

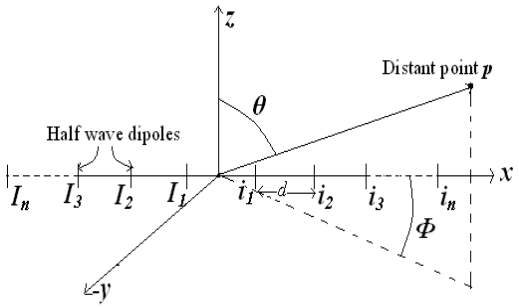

Fig. 1. Linear array of N half wave dipoles with uniform spacing d along the x axis.

The field pattern of this array if the total number of elements in the array is even can be given as,

$$E = E_0[I_n e^{-[N-1]j\psi} .... + I_2 e^{-3j\psi} + I_1 e^{-j\psi} + i_1 e^{+j\psi} + i_2 e^{+3j\psi} .... + i_n e^{+[N-1]j\psi}] \quad (1)$$

where $\Psi = ½\ kd\ \sin\theta\ \cos\varphi$. And for odd number of elements it is,

$$E = E_0[I_n e^{-\frac{[N-1]}{2}j\psi} .... + I_2 e^{-2j\psi} + I_1 e^{-j\psi} + I_0 + i_1 e^{+j\psi} + i_2 e^{+2j\psi} .... + i_n e^{+\frac{[N-1]}{2}j\psi}] \quad (2)$$

where $\Psi = kd \sin\theta \cos\varphi$. I_n is the current excitation coefficient in the left half of the array and i_n is the excitation coefficient in the right half of the array of dipoles with respect to origin. In the case of without mutual coupling $I_1 = i_1$, $I_2 = i_2, \ldots I_n = i_n$. However, they are not equal if we consider mutual coupling between the elements. E_0 is the normalized electric field of a single element and in the case of a half-wave dipole [3]. If we represent the amplitudes of the above array,

$I = [I_n, ...I_2, I_1, i_1, i_2, ...i_n]$ as

$I = [I_1, I_2, I_3 .....I_i ....I_N]$

where $I(i)$ represents the current in the i^{th} element of the array and N represents the total number of elements in the array, then $E \times E^*$ (E^* is the complex conjugate of E) becomes,

$$\begin{aligned} E \times E^* = & \left\{ \sum_{i=1}^{N} [I(i) * I(i)^*] + [\sum_{i=1}^{N-1} I(i) I(i+1)^*] e^{-2j\psi} \right. \\ & + [\sum_{i=1}^{N-1} I(i)^* I(i+1)] e^{2j\psi} + [\sum_{i=1}^{N-2} I(i) I(i+2)^*] e^{-4j\psi} \\ & + [\sum_{i=1}^{N-2} I(i)^* I(i+2)] e^{4j\psi} + ... \\ & + [\sum_{i=1}^{2} I(i) I(i+N-2)^*] e^{-2(N-2)j\psi} \\ & + [\sum_{i=1}^{2} I(i)^* I(i+N-2)] e^{2(N-2)j\psi} + \\ & \left. I(1) I(N)^* e^{-2(N-1)j\psi} + I(1)^* I(N) e^{2(N-1)j\psi} \right\} \left| E_0^{\,2} \right| \end{aligned} \quad (3)$$

note that $E \times E^*$ is not equal to $|E|^2$ if the amplitudes of array elements are not real which will be the case for the array with mutual coupling. Taking the real part of the above expression we get,

$$\begin{aligned} \mathrm{Re}\,al(E \times E^*) = & \left\{ \sum_{i=1}^{N} \mathrm{Re}\,al[I(i) * I(i)^*] \right. \\ & + 2 * \{ \sum_{i=1}^{N-1} \mathrm{Re}\,al[I(i) I(i+1)^*] \cos(2j\psi) \} \\ & + 2 * \{ \sum_{i=1}^{N-2} \mathrm{Re}\,al[I(i) I(i+2)^*] \cos(4j\psi) \} + ... \\ & + 2 * \{ \sum_{i=1}^{2} \mathrm{Re}\,al[I(i) I(i+N-2)^*] \cos(2(N-2)j\psi) \} \\ & \left. + 2 * \{ \mathrm{Re}\,al[I(1) I(N^*)] \cos(2(N-1)j\psi) \} \right\} \left| E_0^{\,2} \right| \end{aligned} \quad (4)$$

with same $\Psi = \frac{1}{2} kd \sin\theta \cos\varphi$, for both even and odd number of elements in the array. If we define $U = \mathrm{Re}\{ E \times E^* \}$, as the radiation intensity of the total array, and then the directivity of the array become, [3]

$$D = \frac{4\pi U_{\max}}{P_{rad}} \quad (5)$$

where P_{rad} is total radiated power given by,

$$P_{rad} = \int_0^{2\pi} \int_0^{\pi} U \sin\theta \, d\theta \, d\varphi \,. \quad (6)$$

II. EFFECT OF MUTUAL COUPLING ON HORIZONTAL FIELD PATTERN

The radiation pattern produced by a half wave dipole in the horizontal (or azimuthal) direction is uniform as an isotropic source and it is a figure '8' pattern in the vertical (or polar) direction. However the radiation pattern or array factor of a two element dipole array in the horizontal direction varies according to separation d and phase difference δ between the elements as well as mutual coupling between them.

Polar plots of horizontal field pattern of a vertical half wave dipole array oriented along the z axis, as a function of phase difference δ and spacing d between two elements, excited with same magnitude of current is given in Fig. 2, with and without mutual coupling. The circles indicate the field pattern of a single reference half wave dipole antenna which is uniform like an isotropic source.

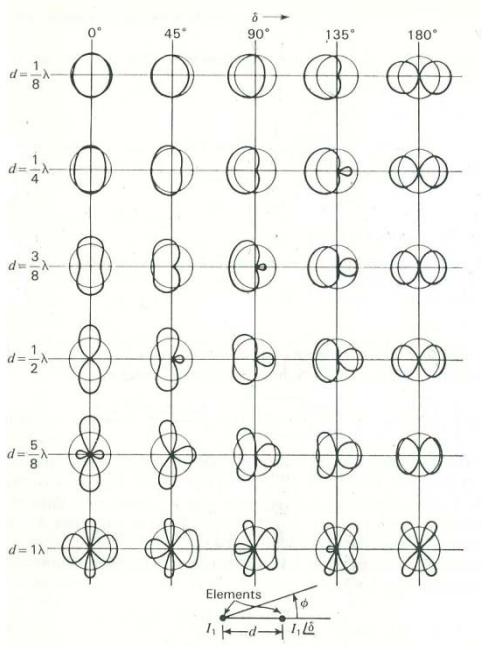

Without mutual coupling. [2]

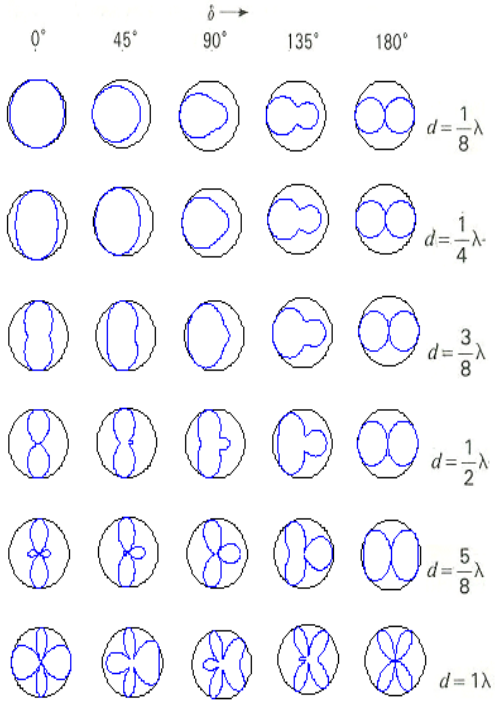

With mutual coupling.

Fig. 2. Field pattern of a two element half wave dipole array vs spacing and phase difference in horizontal plane with and without mutual coupling.

We can see a noticable change in pattern as d & δ vary, due to mutual coupling. In particular there is noticeable enhancement in the size of the back lobe in some cases, which tends to minimize the directivity.

III. BROAD-SIDE CONFIGURATION

In any broad-side array where the relative phase difference between the currents is zero, we analyze mainly three amplitude patterns which are uniform, Dolph-Tchebyscheff (for 20dB side lobe level) and binomial arrays.

The polar field patterns drawn in linear scale, of a three element half wave dipole array along x axis, for each of the above three amplitude configurations with d equal to 0.72 λ, 0.67 λ and 0.67 λ, respectively, which give maximum directivity without mutual coupling, are given in Fig. 3.

The field patterns after considering mutual coupling between the elements are shown in Fig. 4 with same separation d between the elements. D decreases for the uniform amplitude case while increases for the other two amplitude patterns. Notice that the major change in the field patterns with mutual coupling is the change in the side lobe level.

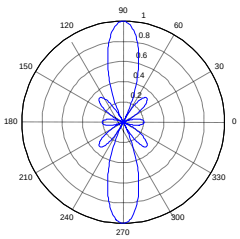

d = 0.72 λ, D = 5.8579
Uniform array

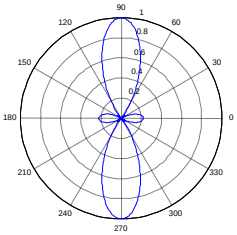

d = 0.72 λ, D = 5.8579
Dolph-Tchebyscheff array

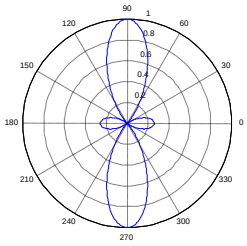

d = 0.67 λ, D = 5.118
Binomial array

Fig. 3. Field patterns of 3 element half wave dipole broad-side uniform, Dolph-Tchebyscheff and binomial arrays with optimum separation '*d*', and maximum directivity '*D'* without mutual coupling.

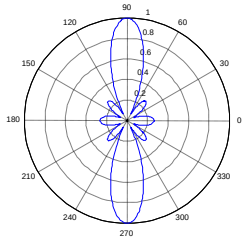

d = 0.72 λ, D = 5.79
Uniform array

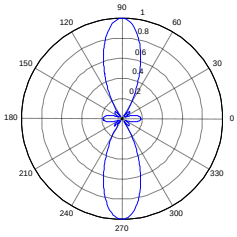

d = 0.67 λ, D = 5.5923
Dolph-Tchebyscheff array

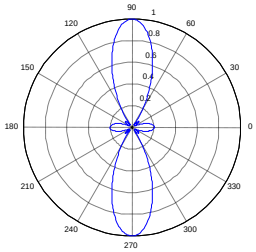

d = 0.67 λ, D = 5.5149
Binomial array

Fig. 4. Field patterns after mutual coupling with same amplitude coefficients and spacing.

The above field patterns are improved for maximum directivity by slightly adjusting the separation between the dipoles. Fig. 5 shows the optimized field patterns after considering mutual coupling, with their corresponding maximum directivity for each of the three amplitude configurations, obtained for d = 0.7 λ, 0.69 λ, and 0.69 λ, respectively. We can notice the increase in the maximum directivity values than those shown in Fig. 4.

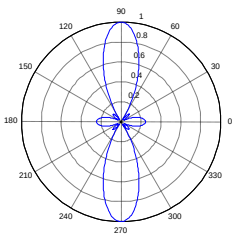

d = 0.7 λ, D = 5.8307
Uniform array

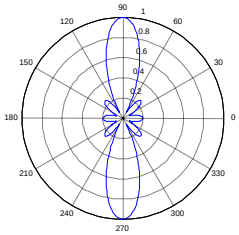

d = 0.69 λ, D = 5.6439
Dolph-Tchebyscheff array

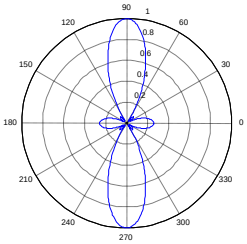

d = 0.69 λ, D = 5.5587
Binomial array

Fig. 5. Optimized field patterns of the three amplitude arrays with mutual coupling.

The variation of directivity for a uniform array of half wave dipoles ranging from 3 to 10, with distance between the elements varying from 0.1 λ to 1 λ is given in Fig. 6. From the graph we can see that there is an increase in the directivity of the array due to mutual coupling for d around 0.5 λ to 0.9 λ at which most broad-side arrays operate and it is less at remaining distances. However maximum directivity of the array is less with mutual coupling than the directivity without coupling.

The optimum separation to maximize directivity for a uniform broad-side array with different number of elements is given in Table 1 with and without mutual coupling. Note that the directivity of the array decreases due to mutual coupling for small N. However, there is little enhancement due to mutual coupling in the optimum directivity for large number of elements in the array. Also the optimum spacing between the elements decreases when mutual coupling is taken into account in order to optimize the directivity for a uniform array.

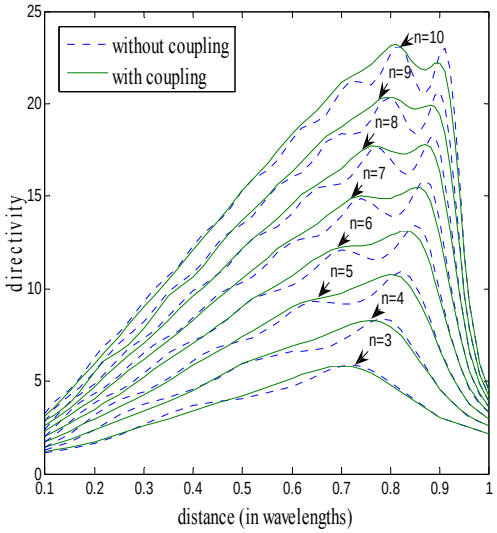

Fig. 6. Variation of directivity with separation d, in uniform n element broad-side array with and without mutual coupling.

Table 1. Uniform broad-side array.

	d	D	d^*	D^*
N=3	0.72 λ	5.8579	0.7 λ	5.8307
N=4	0.78 λ	8.387	0.76 λ	8.3221
N=5	0.82 λ	10.901	0.8 λ	10.7664
N=6	0.85 λ	13.3941	0.83 λ	13.1562
N=7	0.87 λ	15.8495	0.85 λ	15.4865
N=8	0.89 λ	18.2178	0.87 λ	17.7859
N=9	0.9 λ	20.6493	0.8 λ	20.3893
N=10	0.81 λ	23.0761	0.81 λ	23.1784
N=20	0.86 λ	49.601	0.85 λ	49.7916
N=30	0.91 λ	76.9691	0.87 λ	77.1831
N=50	0.92 λ	132.51	0.9 λ	132.87

d = Optimum separation without coupling.
D = Corresponding maximum directivity.
d* = Optimum separation with coupling.
D* = Maximum directivity with coupling.
N = Total number of elements.

For Dolph-Tchebyscheff broad-side array the optimum distance between the elements and the corresponding maximum directivity are given in Table 2, with and without mutual coupling.

Table 2. Broad-side Dolph-Tchebyscheff array.

	d	D	d^*	D^*
N=3	0.67 λ	5.4019	0.69 λ	5.6439
N=4	0.73 λ	7.7082	0.76 λ	8.0623
N=5	0.77 λ	10.2386	0.8 λ	10.6029
N=6	0.8 λ	12.899	0.83 λ	13.2309
N=7	0.83 λ	15.6228	0.85 λ	15.9254
N=8	0.85 λ	18.3781	0.87 λ	18.6261
N=9	0.86λ	21.1917	0.8 λ	21.312
N=10	0.88 λ	23.908	0.81 λ	24.094

Maximum directivity increases due to mutual coupling for this array with a slight adjustment in the spacing between elements.

For the binomial broad side array the optimum separation between the elements and the corresponding directivity are shown in Table 3. Although the directivity of a binomial array is lower relative to uniform and Dolph-Tchebyscheff arrays without coupling, mutual coupling increases the overall directivity of the array because of the larger current amplitudes in the middle of the array. The spacing between the elements needs to be increased for this array to get better directivity.

Table 3. Binomial broad-side array.

	d	*D*	*d**	*D**
N=3	0.67 λ	5.118	0.69 λ	5.5587
N=4	0.70 λ	6.6013	0.74 λ	7.6064
N=5	0.73 λ	7.9028	0.77 λ	9.4228
N=6	0.75 λ	9.0766	0.80 λ	11.0186
N=7	0.76 λ	10.1601	0.81 λ	12.4034
N=8	0.77 λ	11.1627	0.83 λ	13.6332
N=9	0.78λ	12.1052	0.84 λ	14.6996
N=10	0.79 λ	12.9993	0.85 λ	15.6872

IV. END-FIRE CONFIGURATION

In end-fire arrays, if the relative phase difference between the elements is $\delta = kd$, the effect of mutual coupling on the field pattern is more pronounced than in broad-side arrays. The polar field patterns drawn in linear scale, of uniform, Dolph-Tchebyscheff (for 20dB side lobe level) and binomial arrays in end-fire configuration, without mutual coupling between them are given below for a three element array. The optimum distance *d* between the elements to maximize the directivity is 0.37 λ, 0.35 λ, and 0.34 λ, respectively, for the uniform, Dolph-Tchebyscheff and binomial arrays while the directivities for these field patterns are shown in Fig. 7.

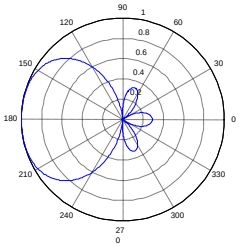

d = 0.37 λ, D = 3.0822
Uniform array

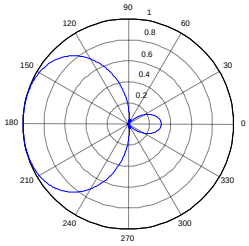

d = 0.35 λ, D = 2.8941
Dolph-Tchebyscheff array

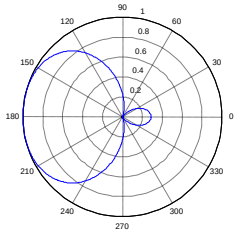

d = 0.34 λ, D = 2.8143
Binomial array

Fig. 7. End fire field patterns of 3 element half wave dipole uniform, Dolph-Tchebyscheff and binomial arrays at optimum separation and with maximum directivity without coupling.

The above field patterns after mutual coupling for same distance *d* between the elements are given in Fig. 8. Observe that there is significant distortion in the shape of the field patterns due to mutual coupling in end-fire arrays, compared to broad side arrays as evidenced from the increase in the back lobe level. As a result the maximum directivity of the array also decreases as shown. When the separation between the elements is changed to improve directivity for each of the three amplitude configurations, the field patterns in Fig. 9 result for *d* = 0.35 λ, 0.29 λ, and 0.28 λ, respectively.

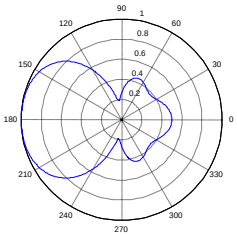

d = 0.37 λ, D = 2.6501
Uniform array

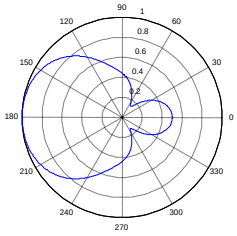

d = 0.35 λ, D = 2.5589
Dolph-Tchebyscheff array

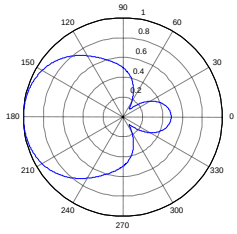

d = 0.34 λ, D = 2.5115
Binomial array

Fig. 8. Field patterns with coupling.

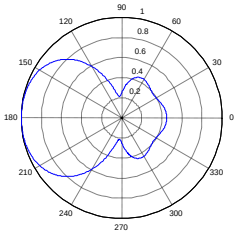

d = 0.35 λ, D = 2.6577
Uniform array

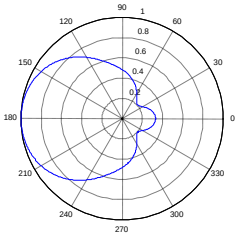

d = 0.28 λ, D = 2.6358
Dolph-Tchebyscheff array

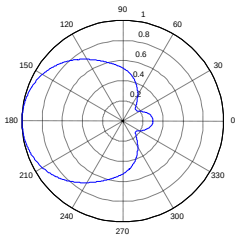

d = 0.29 λ, D = 2.6058
Binomial array

Fig. 9. Optimum patterns with coupling.

Directivity can be increased further by changing the phase excitation between the elements from $\delta = kd$ to $\delta = pkd$ where p is a constant, which is called as Hansen-Woodyard end-fire array. The optimum field patterns obtained this way for the three amplitude excitations neglecting mutual coupling between the dipoles are given in Fig. 10.

However, if we consider mutual coupling between the dipoles, directivity decreases for the three arrays and becomes 3.0039, 1.8317, and 1.419, respectively. We can notice that the directivity for the Dolph-Tchebyscheff and binomial amplitude patterns is very lower compared to before. The new optimum values for p to maximize directivity in the presence of mutual coupling are found to be 1.4, 1.8, and 1.9, for d = 0.27 λ, 0.21 λ, and 0.19 λ, respectively which produces more directivity as shown in Fig. 11. So the effect of mutual coupling is dominant in this type of array and should be considered before designing the array.

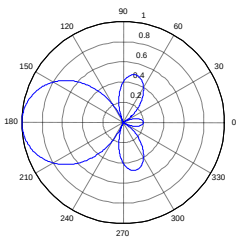

p =1.6, d = 0.27
D = 3.9399
Uniform array

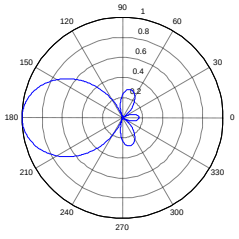

p = 3.9; d = 0.12 λ
D = 4.8319
Dolph-Tchebyscheff array

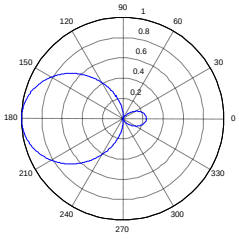

p = 5.2; d = 0.09 λ, D = 4.301
Binomial array

Fig. 10. Field patterns of a 3 element half wave dipole array with the three amplitude patterns and with optimum phase and separation, without mutual coupling.

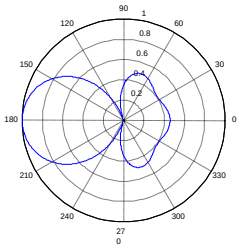

p =1.4; d = 0.27 λ
D = 3.2262
Uniform array

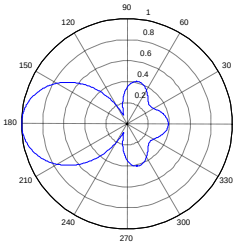

p = 1.8; d = 0.21 λ
D = 3.8761
Dolph-Tchebyscheff array

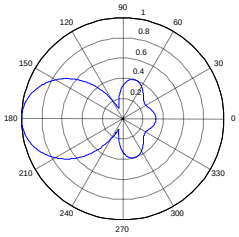

p = 1.9; d = 0.19 λ, D = 3.9694
Binomial array

Fig. 11. Optimized field patterns with change in phase, with mutual coupling.

Variation of directivity with separation between the elements for a two element end-fire array is given in Fig.12. In the end fire operation where elements generally will be placed below half wave length distance (from 0.2λ to 0.5λ approximately), directivity severely decreases due to mutual coupling although there is some increase after half wave length separation. We can observe that mutual coupling has very little effect on the directivity at multiples of half wave length separation. Directivity variation with separation between the elements d and total number of elements N for end fire arrays is shown in Fig.13 which shows the degradation in the directivity due to mutual coupling.

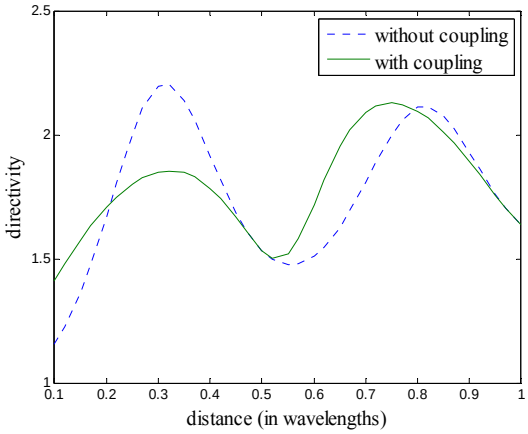

Fig. 12. Variation of directivity with separation, for a 2 element end-fire array with and without mutual coupling.

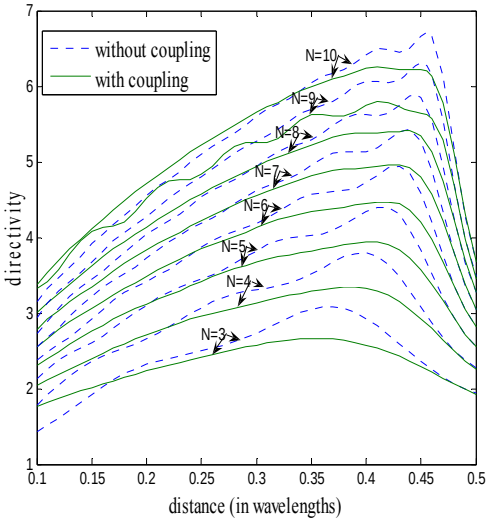

Fig. 13. Variation of directivity with distance in a uniform end-fire array with and without coupling.

Maximum directivity and corresponding optimum separation of a uniform end-fire array is shown in Table 4.

Table 4. Uniform end-fire array.

	d	*D*	*d**	*D**
N=2	0.32 λ	2.2044	0.32 λ	1.8549
N=3	0.37 λ	3.0822	0.35 λ	2.6577
N=4	0.40 λ	3.7922	0.38 λ	3.3426
N=5	0.41 λ	4.396	0.39 λ	3.9395
N=6	0.43 λ	4.9466	0.42 λ	4.4734
N=7	0.44 λ	5.4348	0.43 λ	4.9596
N=8	0.44 λ	5.8683	0.44 λ	5.405
N=9	0.45 λ	6.3121	0.41 λ	5.8047
N=10	0.45 λ	6.7074	0.40 λ	6.2601
N=50	0.48 λ	16.0109	0.47 λ	15.9856
N=70	0.48 λ	19.0824	0.47 λ	19.1346
N=100	0.49 λ	22.9193	0.48 λ	23.1129

with and without mutual coupling, where *N* represents total number of elements in the array. Directivity of the array decreases due to mutual coupling between the elements in uniform end-fire configuration. However, there is little improvement in the directivity if there is large number of elements in the array.

For the Dolph-Tchebyscheff array the maximum directivity is given in Table 5 with corresponding optimum spacing. Maximum directivity decreases for this array due to coupling while the optimum distance with mutual coupling may be below or above the optimum distance obtained without mutual coupling.

Table 5. Dolph-Tchebyscheff end-fire array.

	d	*D*	*d**	*D**
N=3	0.35 λ	2.8941	0.29 λ	2.6358
N=4	0.37 λ	3.505	0.33 λ	3.3119
N=5	0.39 λ	4.0713	0.36 λ	3.8871
N=6	0.41 λ	4.592	0.42 λ	4.4097
N=7	0.42 λ	5.0761	0.43 λ	4.8945
N=8	0.43 λ	5.5216	0.44 λ	5.3425
N=9	0.44 λ	5.9338	0.41 λ	5.8013
N=10	0.44 λ	6.3312	0.43 λ	6.1517

For the binomial end-fire array the optimum distance between the elements and the corresponding maximum directivity is given in Table 6, which shows that maximum directivity decreases when mutual coupling is considered.

Table 6. Binomial end-fire array.

	d	*D*	*d**	*D**
N=3	0.34 λ	2.8143	0.28 λ	2.6058
N=4	0.36 λ	3.2384	0.31 λ	3.0803
N=5	0.37 λ	3.5671	0.34 λ	3.3006
N=6	0.38 λ	3.8408	0.35 λ	3.4236
N=7	0.39 λ	4.0769	0.37 λ	3.5135
N=8	0.4 λ	4.2815	0.38 λ	3.5883
N=9	0.4 λ	4.4682	0.4 λ	3.6629
N=10	0.41 λ	4.6333	0.39 λ	3.7167

V. EFFECT OF MUTUAL COUPLING ON VERTICAL FIELD PATTERN

For the half wave dipole array along *x* axis centered at the origin, mutual coupling affects the directivity of the vertical plane field pattern of constant azimuthal angle. Also note that $\Psi = \frac{1}{2} kd \sin\theta \cos\varphi$ in the array factor now changes to $\Psi = \frac{1}{2} kd \sin\theta$ for $\varphi = 0$ in vertical plane.

Applying the principle of multiplication of field patterns, polar plots of vertical plane field pattern of a 2 element half wave dipole array as a function of phase difference δ and spacing *d* between the elements fed with the same magnitude of current are shown in Fig. 14, with and without mutual coupling. The patterns show

considerable change in some cases due to mutual coupling especially if there is relative phase difference δ between the elements.

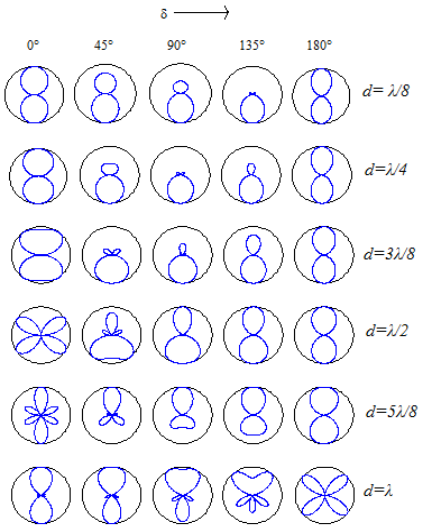

Without mutual coupling

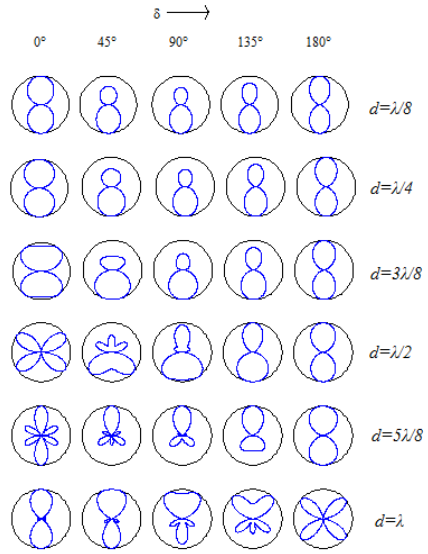

With mutual coupling

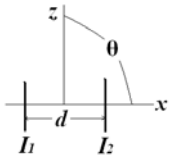

Fig. 14. Field pattern of a 2 element half wave dipole array in vertical direction with variation of spacing and phase difference between the dipoles, before and after considering mutual coupling.

Polar field patterns of a 3 element end-fire half wave dipole array with optimum distance *d* between the elements as 0.85 λ and 0.81 λ and where maximum directivity can be achieved for uniform and binomial amplitude coefficients with phase difference between the elements as $\delta = kd$ without mutual coupling are shown in Fig. 15 with their corresponding directivities.

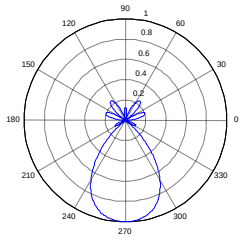

d = 0.85 λ, D = 4.0704
Uniform array

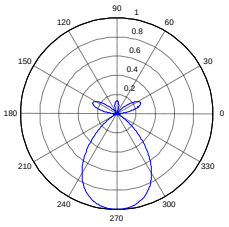

d = 0.81 λ, D = 3.8959
Binomial array

Fig. 15. Polar field pattern of 3 element uniform and binomial amplitude arrays in end-fire direction at optimum spacing.

When mutual coupling is considered between the elements with same amplitudes and separation between the elements, the patterns change to those shown in Fig. 16. As in the case of horizontal plane field pattern, the side lobe level is increased by mutual coupling, however the directivity is increased for the case of binomial array.

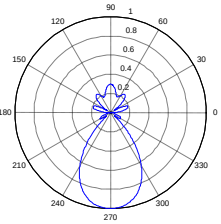

d = 0.85 λ, D = 4.056
Uniform array

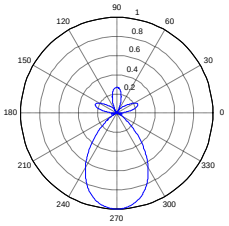

d = 0.81 λ, D = 4.1394
Binomial array

Fig. 16. Above field patterns after considering mutual coupling.

The optimum distance between the elements changes with mutual coupling to improve the directivity. The corresponding field patterns are shown in Fig. 17 along with their directivities.

The new value of *d* that gives maximum directivity is found to be 0.82 λ for both uniform and binomial amplitude arrays.

Optimum value of *d* between the elements and corresponding directivity for both uniform and binomial amplitude coefficients in end-fire configuration are given in Tables 7 and 8, before and after mutual coupling consideration for different *N*.

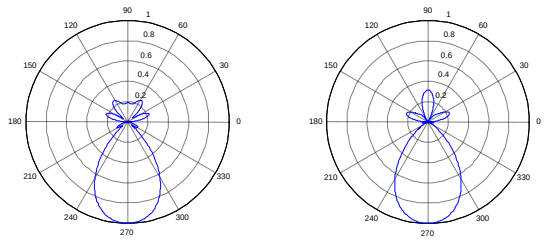

d = 0.82 λ, D = 4.1332
Uniform array

d = 0.82 λ, D = 4.2939
Binomial array

Fig. 17. Optimum field patterns with mutual coupling for maximum directivity.

Table 7. Uniform end-fire array in vertical direction.

	d	*D*	*d**	*D**
N=2	0.79 λ	3.414	0.74 λ	3.4838
N=3	0.85 λ	4.0704	0.82 λ	4.1332
N=10	0.91 λ	6.7963	0.9 λ	7.0594
N=50	0.97 λ	14.8917	0.94 λ	15.3628

Unlike the case of azimuthal patterns, the maximum directivity is slightly improved due to mutual coupling in the vertical plane even for the lower values of *N*.

The directivity in the binomial amplitude end-fire also improves due to mutual coupling after slightly adjusting the spacing between elements as shown in Table 8.

Table 8. Binomial end fire array in vertical direction.

	d	*D*	*d**	*D**
N=3	0.81 λ	3.8959	0.82 λ	4.2939
N=10	0.91 λ	6.7963	0.90 λ	7.0594

VI. EFFECT OF MUTUAL COUPLING ON 3 -D FIELD PATTERN

The maximum directivity and corresponding optimum spacing between the elements for the uniform array placed along the *x* axis in broad-side and end-fire configuration are given in Tables 9 and 10, calculated by considering both polar and azimuthal angles into account. We can clearly see that mutual coupling is degrading the overall directivity of the array in both configurations especially more in the end-fire array. Also the optimum spacing between the elements does not remain the same after considering mutual coupling.

Table 9. Uniform broad-side array.

	d	*D*	*d**	*D**
N=2	0.67 λ	5.0217	0.67 λ	5.0217
N=3	0.76 λ	8.6101	0.74 λ	8.5405
N=10	0.92 λ	34.4619	0.84 λ	33.9866
N=50	0.6 λ	82.6351	0.62 λ	83.8385

Table 10. Uniform end-fire array.

	d	*D*	*d**	*D**
N=2	0.33 λ	3.8437	0.36	3.2705
N=3	0.36 λ	4.2401	0.30	2.8679
N=10	0.46 λ	19.1332	0.43	17.0622
N=50	0.48 λ	94.6537	0.48	88.9445

VII. EFFECT OF CHANGING LENGTH

We observed that maximum directivity is degraded in half wave dipole array due to mutual coupling in both broad-side and end-fire configurations. The change in the maximum directivity of the overall array by adjusting the length [2] of the each dipole in the array can be observed here, by noting the change in near and far field regions, resulting from the change in the dipole length. Variation in the directivity with length of a 2 element uniform broad-side array placed along the *x* axis, is given in Table 11. Here *d* represents the optimum separation where maximum directivity (calculated for the three dimensional field pattern of the array) occurs.

Table 11. Variation of maximum directivity with dipole length, for a 2 element broad-side array.

l	*d*	*D*
0.5 λ	0.67 λ	5.0217
0.6 λ	0.66 λ	5.2952
0.7 λ	0.66 λ	5.6695
0.8 λ	0.65 λ	6.1819
0.9 λ	0.65 λ	6.8924
1 λ	0.64 λ	7.8691
1.1 λ	0.63 λ	9.1178
1.2 λ	0.63 λ	10.2192
1.3 λ	0.63 λ	9.5801

We can see that maximum directivity increases as the length of the dipole increases up to some extent and the optimum length is around 1.2 λ. If the length increases further, the directivity decreases and more side lobes appear. Also we can see that the optimum separation between the dipoles which gives maximum directivity decreases as the length of both dipoles increases.

The directivity variation in the case of 2 element end-fire dipole array is given in Table.12 which shows that directivity decreases after considering mutual coupling for dipole lengths less than 1 λ. However, if we increase the length of the dipole above 1 λ, more directivity can be obtained by adjusting the separation between the dipoles. From the table we can see that maximum directivity occurs for dipole length around 1.3 λ.

Maximum directivities that can be obtained by changing the dipole length of all elements are given in Tables 13 and 14 for both broad side and end fire configuration. We can see that there is improvement in the total directivity of the array by changing the length and this optimum length is found to be around 1.23 λ for

a broad-side array, and in end fire arrays this optimum length is even more. There is much increase in the directivity of the end-fire array by mutual coupling than compared to broad-side array by changing the length of the dipole from 0.5 λ which we can observe. Also the optimum dipole length along with separation between the dipoles is not remained same after considering mutual coupling.

Table 12. Variation of directivity with dipole length for a 2 element end-fire array.

l	*d*	*D*	*d**	*D**
0.5 λ	0.33 λ	3.8437	0.36 λ	3.2705
0.6 λ	0.33 λ	4.003	0.37 λ	3.6289
0.7 λ	0.33 λ	4.2184	0.36 λ	3.8663
0.8 λ	0.33 λ	4.5106	0.36 λ	4.1023
0.9 λ	0.33 λ	4.9107	0.37 λ	4.3463
1 λ	0.32 λ	5.4686	0.35 λ	4.5489
1.1 λ	0.32 λ	6.2226	0.18 λ	8.0466
1.2 λ	0.32 λ	7.1033	0.26 λ	8.1592
1.3 λ	0.33 λ	7.5118	0.28 λ	8.3672
1.4 λ	0.35 λ	6.0750	0.29 λ	7.1492

Table 13. Optimization of directivity by changing length in uniform broad-side array.

	l	*d*	*D*	*l**	*d**	*D**
N=2	1.23	0.63	10.3129	1.23	0.63	10.3129
N=3	1.24	0.74	18.0823	1.23	0.73	18.2829
N=10	1.24	0.91	69.848	1.22	0.9	75.2991
N=50	1.23	0.59	174.2973	1.23	0.57	174.2695

l = optimum length (in wave lengths) without mutual coupling.
*l** = optimum length (in wave lengths) with coupling.

Table 14. Optimization of directivity by changing length in uniform end-fire array.

	l	*d*	*D*	*l**	*d**	*D**
N=2	1.29	0.33	7.5295	1.27	0.28	8.3925
N=3	1.31	0.35	8.2584	1.31	0.32	8.5948
N=10	1.44	0.46	32.1662	1.44	0.41	55.098
N=50	1.54	0.48	120.5469	1.42	0.42	267.2029

VIII. CONCLUSION

The effect of mutual coupling is very less in uniform dipole arrays for multiples of half wave length separation between the elements. The maximum directivity of a λ /2 uniform dipole array decreases due to mutual coupling although there is little increase in broad-side arrays for large number of elements in the array. Therefore we need to minimize the mutual coupling effect if there are few number of elements in the array and if there are large number of elements we need to use the effect for maximum directivity. The degradation with mutual coupling is more severe in uniform end-fire arrays than broad-side arrays. However, there is an increase in the maximum directivity due to mutual coupling with little adjustment in separation between the elements for Dolph-Tchebyscheff and binomial broad-side arrays even with little number of elements in the array. Directivity of the uniform dipole array with mutual coupling can be increased with even less number of elements in the array by adjusting the dipole length to be above 1 λ for broad-side arrays and above 1.25 λ end-fire arrays, being aware of the fact that there will be change in the far and near field regions of the array with the change in the dipole length.

ACKNOWLEDGEMENT

I want to dedicate this to my parents for their love and support. Also the authors express sincere thanks to the faculty of Electrical department, University of South Alabama for their valuable assistance.

REFERENCES

[1] K. R. Siarkiewicz and A. T. Adams, "Near-and far-field thin-wire coupling: theory and experiment," *IEEE Transactions on Electromagnetic compatibility,* vol. 19, no. 4, pp. 394-401, Nov. 1977.

[2] J. D. Kraus, *Antennas*, 2nd edition, McGraw-Hill, Chapters 4, 10, and 11, 1988.

[3] C. A. Balanis, *Antenna Theory*, 3rd edition, John Wiley, Chapters 2, 4, 6, and 7, 2005.

[4] P. S. Carter, "Circuit relations in radiating systems and applications to antenna problems," *Proceedings of the Institute of Radio Engineers,* vol. 20, no. 6, pp. 1004-1041, Jun. 1932.

[5] G. H. Brown, "Directional Antennas", *Proceedings of the Institute of Radio Engineers,* vol. 25, no. 1, pp. 78-145, Jan. 1937.

[6] T. Svantesson, "Modeling and estimation of mutual coupling in a uniform linear array of dipoles," *IEEE International Conference on Acoustics, Speech and Signal Processing,* vol. 5, pp. 2961-2964, 1999.

[7] H. C. Baker and A. H. Lagrone, "Digital Computation of the mutual impedance between thin dipoles," *IRE Transactions on Antennas and Propagation,* vol. 10, no. 2, pp. 173-178, Mar. 1962.

[8] Y. P. Xi, D. G. Fang, Y. X. Sun, and Y. L. Chow, "Mutual coupling in a linear dipole array of finite size," *IEE Proceedings on Microwaves, Antennas and Propagation,* vol. 152, no. 5, pp. 324-330, Oct. 2005.

[9] R. Luebbers and K. Kunz, "Finite difference time domain calculations of antenna mutual coupling," *IEEE Transactions on Electromagnetic Compatibility,* vol. 34, no. 3, pp. 357-359, Aug. 1992.

[10] W. L. Stutzman and G. A. Thiele, *Antenna theory and design*, 2nd edition, John Wiley, Chapter 3, 1998.

[11] C. T. Tai, "The optimum directivity of uniformly spaced broad-side arrays of dipoles," *IEEE Transactions on Antennas and Propagation,* vol. 12, pp. 447-454, July 1964.
[12] A. H. Nuttall and B. A. Cray, "Approximations to directivity for linear, planar, and volumetric apertures and arrays," *IEEE Journal of Oceanic Engineering,* vol. 26, pp. 383-398, July 2001.
[13] J. A. Kinzel, "Radiation characteristics of a planar broad-side array of Directive elements," Ohio State University research foundation, Columbus, Ohio, Apr. 1964.
[14] C. T. Tai and C. S. Pereira, "An approximate formula for calculating the directivity of an antenna," *IEEE Transactions on Antennas and Propagation,* vol. 24, pp. 235-236, Mar. 1976.
[15] K. Nagasawa, R. Kitoh, T. Kondo, and N. Hasebe, "A design method of array antennas taking into account mutual coupling between elements: Uniform arrays consisting of parallel half -wavelength dipoles," *Electronics and Communications in Japan*, Part 1, vol. 86, no. 1, pp. 1-15, Sep. 2002.
[16] F. Sellone and A. Serra, "A novel online mutual coupling compensation algorithm for uniform and linear arrays", *IEEE Transactions on Signal Processing,* vol. 55, no. 2, pp. 560-573, Feb. 2007.
[17] Y. T. Lo and S. W. Lee, *Antenna Handbook: Theory, Applications and Design*, Van Nostrand Reinhold Company, New York, Chapter 11.
[18] Sophocles J. Orfanidis, *Electromagnetic Waves and Antennas*, Chapter 21, http://www.ece.rutgers.edu/~orfanidi/ewa/ch21.pdf

Venkata Naga Srinivas Kalaga was born in Rajahmundry, India, in 1985. He received his Bachelors of Technology degree in Electronics and Communications Engineering in 2006 from JNTU University, India. Currently he is studying Master of Science in Electrical Engineering at University of South Alabama, U.S.A. His graduate research is focused on Antennas and Electromagnetics.

Michael Hamid graduated from McGill University in Montreal with B.Eng. degree in 1960, M.Eng. degree in 1962 and from the University of Toronto with a Ph.D. degree in 1966, all in Electrical Engineering. Presently he is a Professor in Electrical Engineering at the University of South Alabama. He is a past president of the International Microwave Power Institute, a Fellow of IEE and IEEE and published 310 refereed articles and 25 patents.

Analysis of a Cylindrical Dielectric Radome Covering Omnidirectional Waveguide Slot Antennas

[1]J.-Y. Li, [2]J.-Li Guo, [2]Y.-L. Zou, and [2]Qi-Z. Liu

[1] Temasek Laboratories, National University of Singapore
Email: tsllijy@nus.edu.sg

[2] National Key Laboratory of Antennas and Microwave Technology, Xidian University

Abstract – In this paper, the method of moments (MoM) is employed to solve the electromagnetic field integral equation for characterizing slotted waveguide antenna covered by a dielectric radome. Different from those existing practical examples discussed in literature, these structures consist of mixed conducting and homogeneous dielectric objects. Both basis functions and testing functions are chosen as the well-established Rao-Wilton-Glisson (RWG) basis functions. Effects of the radome on the slotted antenna's radiation patterns are analyzed and discussed.

Keywords: Slot antenna, radiation pattern, method of moments, and radome.

I. INTRODUCTION

Omnidirectional waveguide slot array antennas are widely used in communication systems and beacon radar systems. This kind antenna arrays are easily designed and manufactured. They also have low profiles and high gains. The omnidirectional waveguide-slot array antennas have been used in practice for many years since the first experimental work [1]. Later, Lyon and Sangster [2] and Lü [3] theoretically analyzed waveguide slots and a slot-pair by employing the method of moments (MoM) to solve the resultant integral equations for the equivalence magnetic currents. An analysis of omnidirectional waveguide slot-pair in a standard rectangular (both air-filled and dielectric-filled) waveguide was carried out by Sangster and Wang [4]. Recently, Li [5] introduced a way to compute the radiation pattern of the omnidirectional waveguide slot-pair.

Usually, this type antenna must be covered by a radome in the communication system. Then, the radiation pattern of the slot antenna will degrade due to the effects of the radome. The RCS of dielectric material objects is analyzed by [6]. The scattering problems of mixture of conducting and dielectric objects are analyzed in [7-8]. Characterization of radiation by waveguide slot antenna with an arbitrarily shaped radome is an important subject for the communication systems, but it is also a difficult task. In this paper, radiation patterns of a slot-pair array covered by a radome are studied. The integral equation consisting of electric field integral equation and magnetic field integral equation is solved directly using the method of moment with Rao-Wilton-Glisson (RWG) basis functions [9].

The paper is organized as follows. In the next section, we will briefly present necessary mathematical formulations for the problem with mixed conducting and dielectric objects located in an isotropic free space medium at first. We outline how the method of moments is applied to solve the problem of waveguide slot antenna covered by a cylindrical radome. The RWG functions [9] are used as the basis and testing functions in the present the Galerkin's procedure. In the third section, numerical examples are presented so as to depict radiation patterns of several selected examples and the results of these examples are obtained and compared with available data.

II. DESCRIPTION OF FORMULATION

The equations defined here for electromagnetic scattering by mixed dielectric and electric conducting objects of arbitrary shapes are quite well established. As shown in Fig. 1, an example of an arbitrarily shaped homogeneous scatterer next to a conducting object is considered.

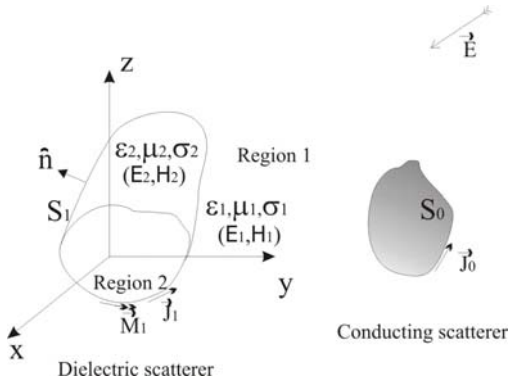

Fig. 1. Geometry of a dielectric scatterer and a conducting scatterer in an isotropic free space medium as a general configuration for the later radome analysis applications.

The permittivity and permeability of the dielectric scatterer are represented by ε_2 and μ_2, respectively. The scatterer is immersed in an infinite and homogeneous medium of permittivity ε_1, and permeability μ_1. In most applications, this infinite medium is free space.

Let $\vec{J}_1(\vec{r})$ and $\vec{M}_1(\vec{r})$ represent equivalent electric and magnetic currents on the surface of the homogeneous object. $\vec{J}_0(\vec{r})$ represents the equivalent electric surface current on the conducting object. Applying the equivalent principle to this electromagnetic problem, and considering the boundary condition, we obtain the electric and magnetic field integral equations below,

$$\vec{E}^1(\vec{r})|_{\tan} = \left\{ \left[j\omega\vec{A}_{11} + \nabla V_{11} \right] + \left[j\omega\vec{A}_{21} + \nabla V_{21} \right] + \left[\frac{1}{\varepsilon_1'} \nabla \times \vec{F}_{11} + \frac{1}{\varepsilon_2'} \nabla \times \vec{F}_{21} \right] + \left[j\omega\vec{A}_{10} + \nabla V_{10} \right] \right\} \Big|_{\tan} \quad (1a)$$

$$\vec{H}^1(\vec{r})|_{\tan} = \left\{ -\left[\frac{1}{\mu_1} \nabla \times \vec{A}_{11} + \frac{1}{\mu_2} \nabla \times \vec{A}_{21} \right] + \left[j\omega\vec{F}_{11} + \nabla U_{11} \right] + \left[j\omega\vec{F}_{21} + \nabla U_{21} \right] - \frac{1}{\mu_1} \nabla \times \vec{A}_{10} \right\} \Big|_{\tan} \quad (1b)$$

for $\vec{r}$ on the surface S_1;

$$\vec{E}^0(\vec{r})|_{\tan} = \left\{ \left[j\omega\vec{A}_{11} + \nabla V_{11} \right] + \left[\frac{1}{\varepsilon_1'} \nabla \times \vec{F}_{11} \right] + \left[j\omega\vec{A}_{10} + \nabla V_{10} \right] \right\} \Big|_{\tan} \quad (1c)$$

for $\vec{r}$ on the surface S_0,

where $\vec{E}^1(\vec{r})$, $\vec{H}^1(\vec{r})$ and $\vec{E}^0(\vec{r})$ stand for the incident electric and magnetic fields in region 1 and the subscript "tan" refer to tangential components on the surfaces, S_1 and S_0. The vector potentials, $\vec{A}_{i1}(\vec{r})$ and $\vec{F}_{i1}(\vec{r})$ for $i = 1,2$, and the scalar potentials, $V_{i1}(\vec{r})$ and $U_{i1}(\vec{r})$, are given by,

$$\vec{A}_{i1} = \vec{A}_{i1}(\vec{r}) = \frac{\mu_i}{4\pi} \int_S G_i(\vec{r},\vec{r}') \cdot \vec{J}_1(\vec{r}') dS' \quad (2a)$$

$$\vec{F}_{i1} = \vec{F}_{i1}(\vec{r}) = \frac{\varepsilon_i'}{4\pi} \int_S G_i(\vec{r},\vec{r}') \cdot \vec{M}_1(\vec{r}') dS' , \quad (2b)$$

$$V_{i1} = V_{i1}(\vec{r}) = \frac{1}{4\pi\varepsilon_i'} \int_S G_i(\vec{r},\vec{r}') \cdot \rho_1^e(\vec{r}) dS' , \quad (2c)$$

$$U_{i1} = U_{i1}(\vec{r}) = \frac{1}{4\pi\mu_i} \int_S G_i(\vec{r},\vec{r}') \cdot \rho_1^m(\vec{r}) dS' , \quad (2d)$$

$$\varepsilon_i' = \varepsilon_i - j\sigma_i/\omega , \quad (2e)$$

$$\rho_1^e(\vec{r}) = \frac{-1}{j\omega} \left[\nabla' \cdot \vec{J}_1(\vec{r}') \right] , \quad (2f)$$

$$\rho_1^m(\vec{r}) = \frac{-1}{j\omega} \left[\nabla' \cdot \vec{M}_1(\vec{r}') \right] , \quad (2g)$$

$$\vec{A}_{10} = \vec{A}_{10}(\vec{r}) = \frac{\mu_i}{4\pi} \int_S G_1(\vec{r},\vec{r}') \cdot \vec{J}_0(\vec{r}') dS' , \quad (2h)$$

$$V_{10} = V_{10}(\vec{r}) = \frac{1}{4\pi\varepsilon_i'} \int_S G_1(\vec{r},\vec{r}') \cdot \rho_0^e(\vec{r}) dS' , \quad (2i)$$

$$\rho_0^e(\vec{r}) = \frac{-1}{j\omega} \left[\nabla' \cdot \vec{J}_0(\vec{r}') \right] . \quad (2j)$$

The Green's functions, $G_i(\vec{r},\vec{r}')$ where $i = 1,2$, have the following form,

$$G_i(\vec{r},\vec{r}') = \frac{e^{-jk_iR}}{R} \quad (3)$$

where $R = |\vec{r} - \vec{r}'|$ and,

$$k_i = \omega\sqrt{\mu_i\varepsilon_i'} \quad . \quad (4)$$

Equations (1a-1c) are solved by applying the method of moments. In this work, all the surfaces of scatterers are approximated by planar triangular patches and thus the RWG functions [9] are chosen as both basis functions and testing functions. As in a conventional MoM solution, the unknown surface electric and magnetic current distributions $\vec{J}_1(\vec{r})$, $\vec{M}_1(\vec{r})$, and $\vec{J}_0(\vec{r})$ are expanded into three sets of basis functions $\{\vec{f}_n^1(\vec{r})\}$, $\{\vec{f}_n^1(\vec{r})\}$ and $\{\vec{f}_n^0(\vec{r})\}$ as follows,

$$\vec{J}_1(\vec{r}) = \sum_{n=1}^{N_d} I_n^1 \cdot \vec{f}_n^1(\vec{r}) \tag{5a}$$

$$\vec{M}_1(\vec{r}) = \sum_{n=1}^{N_d} M_n^1 \cdot \vec{f}_n^1(\vec{r}), \tag{5b}$$

$$\vec{J}_0(\vec{r}) = \sum_{n=1}^{N_c} I_n^0 \cdot \vec{f}_n^0(\vec{r}) \tag{5c}$$

where N_d and N_c stand for the numbers of edges on the dielectric and conducting surfaces of the triangular model, respectively. After applying the method of moments to equations (1a-1c), the equations are converted into a system of N linear equations and are further written in matrix form as follows,

$$\begin{bmatrix} Z_{11} & Z_{12} & Z_{13} \\ Z_{21} & Z_{22} & Z_{23} \\ Z_{31} & Z_{32} & Z_{33} \end{bmatrix} \cdot \begin{bmatrix} I_1 \\ M_1 \\ I_0 \end{bmatrix} = \begin{bmatrix} E_1 \\ H_1 \\ E_0 \end{bmatrix} \tag{6}$$

where the impedance matrix is of dimension NxN with N = N_d + N_c, and all the elements in equation (6) are sub-matrixes [8].

For a scattering problem, the right-hand side of equation (6) may be written,

$$E_{1j} = \int_{S_1} \vec{f}_j^1(\vec{r}) \cdot \vec{E}^1(\vec{r}) dS \tag{7}$$

$$H_{1j} = \int_{S_1} \vec{f}_j^1(\vec{r}) \cdot \vec{H}^1(\vec{r}) dS\ , \tag{8}$$

$$E_{0j} = \int_{S_1} \vec{f}_j^0(\vec{r}) \cdot \vec{E}^0(\vec{r}) dS\ . \tag{9}$$

For the radiation problem, one can set a voltage source in the excitation port. However, only a few elements of E^0 in equation (6) are assigned to be nonzero values.

For the geometry of slotted waveguide antennas covered by a cylinder radome in this paper, a short dipole is placed in the waveguide as the exciting source when we analyze the radiation characteristics of the slotted-waveguide antennas.

III. NUMERICAL RESULTS

Based on the theoretical formulas and MoM, a code is written in fortran language for simulating the waveguide slot array with radome and scattering from hybrid metallic-dielectric objects. To examine the correctness of the code, we first investigate bistatic radar cross sections (RCSs) of a conducting sphere next to an air-filled dielectric sphere. The RCS results are obtained for a plane wave of $\theta\theta$-polarization, with an incidence angle of $\theta = 0^o$ and $\varphi = 90^o$. The results are shown in Fig. 2 where the "Conducting sphere only" results were obtained using the EFIE in the absence of the dielectric objects. Two cases are considered here, one (with 1,200 unknowns) for a conducting sphere of 1 meter radius only, and the other (with 3,600 unknowns) for a conducting sphere of 1 meter radius next to a dielectric sphere of 1-meter radius (which is also considered as a special case, we considered $\varepsilon_r = 1$, $\mu_r = 1$, and $\sigma = 0$, and the distance is 3 meters in the y-direction). A good agreement between the numerical results for both cases is observed in Fig. 2; and certainly the agreement is expected. This indicates that the results produced by the code are reducible to those of special cases, partially verifying the correctness of the code.

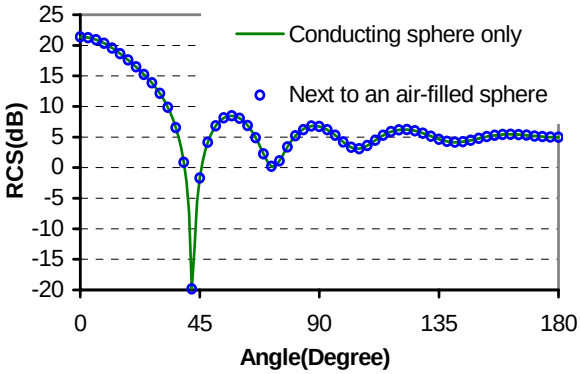

Fig. 2. Bistatic RCS of a sphere at $f = 0.3$ GHz.

The geometer of radome and slotted waveguide are shown in Figs. 3 (a) and (b). The axis of cylinder radome is along z direction. The slotted waveguide is put in the center of the radome along the axis. The radome is open in the bottom and is closed on the top. The height of cylinder radome is 90mm. The radii (R), the depth (D) and the permittivity (ε_r) of the radome are chosen with different values for analyzing the effect of the radome. The slotted waveguide with radome is analyzed as following.

The selected working frequency is 9.375 GHz here. The width of the waveguide is 22.86 mm. The height of waveguide is 1 mm. The total length of waveguide is 1.3 λ_g. The depth of waveguide is 1 mm. One end of the waveguide is shorted, and the dipole is placed near another end (0.25 λ_g, λ_g = 44.8036 mm). The width of the slots is 1.00 mm. Two slot-pairs are cut on the waveguide walls. The distance between the two slot-pairs is 0.5 λ_g.. The length of the slot is 13.90 mm, the offset of the slot-pair is 1.00 mm, the slot center located at 0.25 λ_g away from the shorted plug.

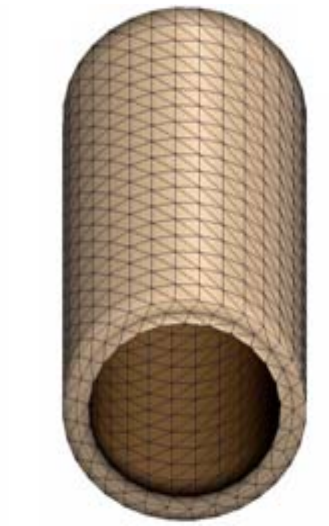

(a) Radome.

(b) slotted waveguide.

Fig. 3. Radome and slotted waveguide antenna.

To further verify the correctness and capability of our code and the idea for analyzing the slotted waveguide, the radiation patterns of the waveguide slot antenna (with air-filled radome, set ε_2=1.0) are computed first. The results are presented in Fig. 4 where both the *E*- and *H*-plane patterns are shown. The *E*-plane and *H*-plane patterns are in x-y plane (θ=90°, ϕ turns from 0° to 360°) and y-z plane (ϕ=90°, θ turns from 0° to 360°), respectively. All the radiation patterns are normalized.

A good agreement between the numerical results of both the air-filled radome case and no radome case is observed. This indicates that the results produced by the code are reducible to those of special cases, partially verifying the correctness of the code and the analysis way.

Different parameters of the radome, namely, the radii (*R*), the depth (*D*) and the permittivity (ε_r), are chosen subsequently for analyzing the effects of the radome. The radii (*R*) are chosen to be: (1) 0.5λ; (2) 0.6λ; (3) 0.65λ; and (4) 0.75λ. The depths (*D*/λ) are assumed to be (1) 0.125; (2) 0.1764; (3) 0.25. The relative permittivities of ε_2 are chosen as (1) 2; (2) 3; and (3) 4.

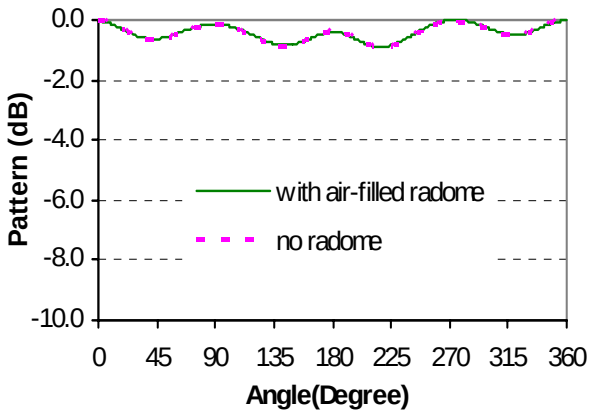

(a) *E*-plane (θ=90°, ϕ changes from 0° to 360°).

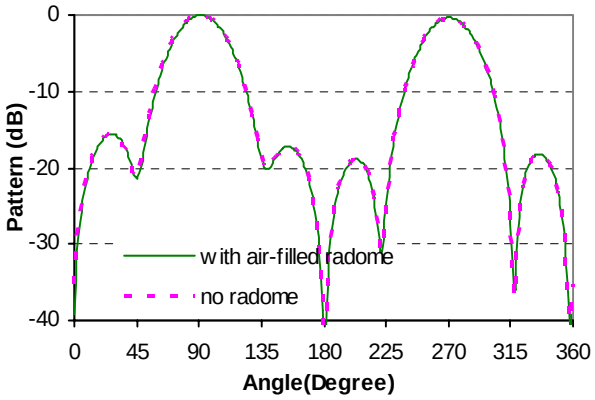

(b) *H*-plane (ϕ=90°, θ changes from 0° to 360°).

Fig. 4. The computed far field patterns of slot-pair.

First of all, we consider the variation of the relative permittivity of the dielectric radome and the radome's radius. The computed results are presented in Figs. 5-7 where the radii (*R*) and the permittivities (ε_r) of the radome are different, and the depth is chosen as 0.125λ. When the radius (*R*) are half a wavelength (*i.e.*, 0.5λ), the *E*-plane and *H*-plane far-zone patterns are both poor. It is however realized that if the radii (*R*) are chosen as 0.6λ and 0.65λ, respectively, the roundness of *E*-plane pattern is better when different permittivities (ε_r) are used. The effects due to permittivity changes are apparently very significant. If ε_r = 2, effects of radii (*R*) becomes less important, but if ε_r increases to be higher in value, we must be very careful to choose appropriate radii of the radome to maintain the generally overall good performance of the antenna. Therefore, it is very important for a radome designer to know clearly what kind of effects will be caused by changing the configurations of the whole system during the antenna and its dielectric radome designs.

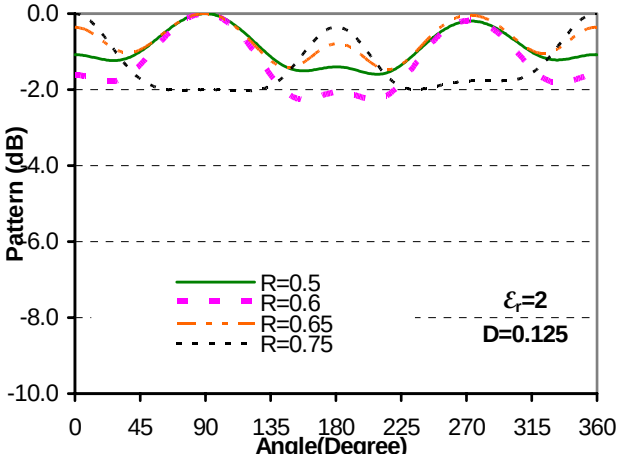

(a) *E*-plane.

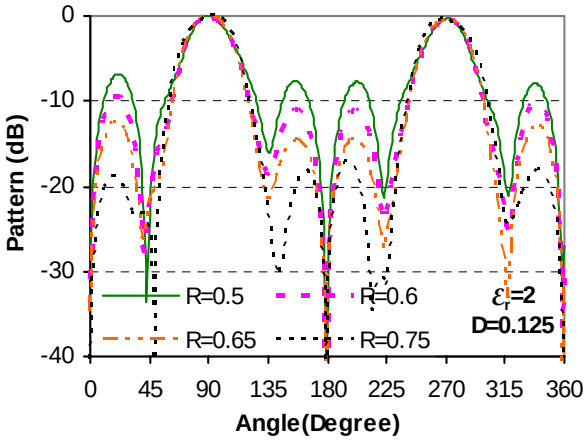

(b) *H*-plane.

Fig. 5. The computed far field patterns of the slot-pair.

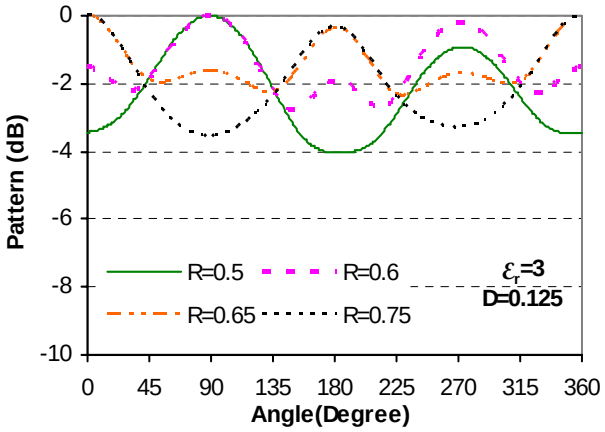

(a) *E*-plane.

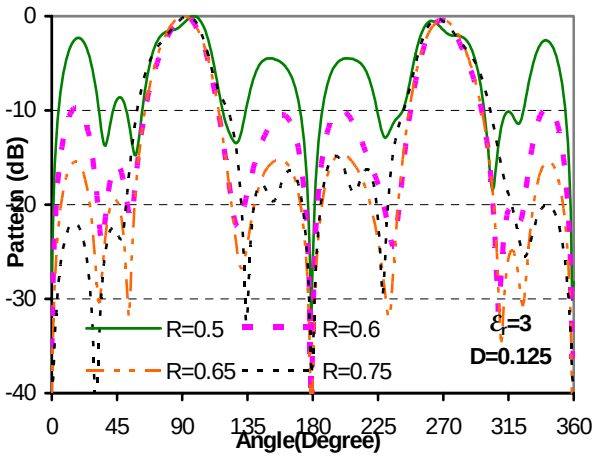

(b) *H*-plane.

Fig. 6. The computed far field patterns of the slot-pair.

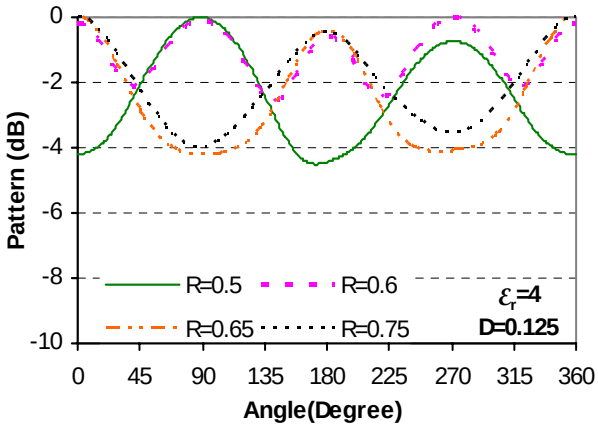

(a) *E*-plane.

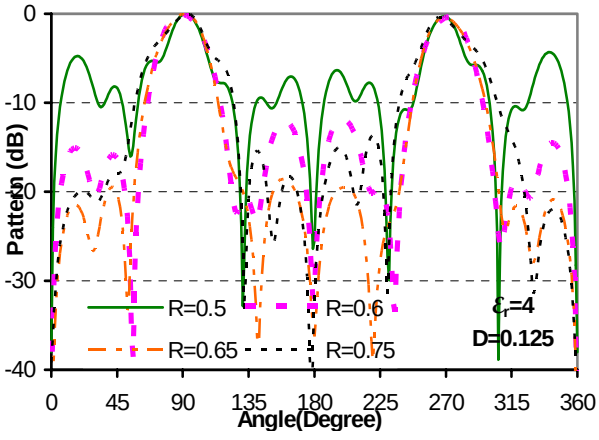

(b) *H*-plane.

Fig. 7. The computed far field patterns of the slot-pair.

Subsequently, computed results (when the depth is chosen as 0.1764λ) are presented in Figs. 8-10 where the radii (R) and the permittivities (ε_r) of the radome vary. When the radii (R) are chosen to be 0.5λ and 0.75λ, respectively, the E-plane and H-plane antenna patterns are both poor. If the radii (R) are chosen as 0.6λ and 0.65λ, respectively, the E-plane pattern is apparently improved when the different permittivity (ε_r) values are used.

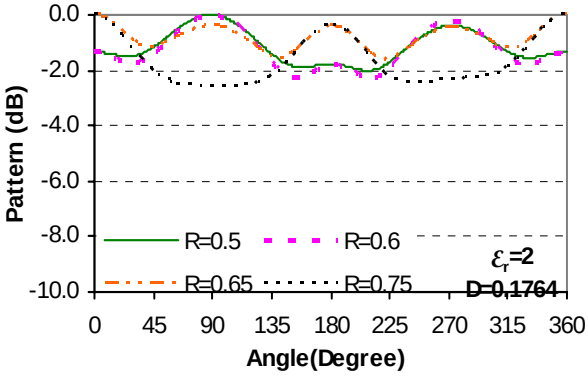

(a) E-plane.

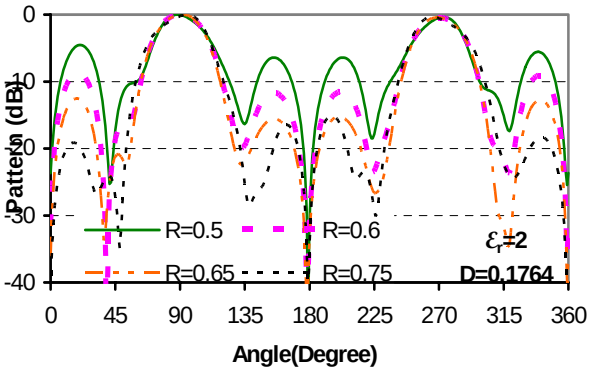

(b) H-plane.

Fig. 8. The computed far field patterns of the slot-pair.

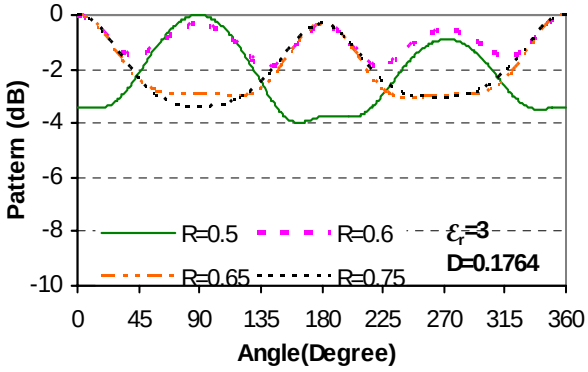

(a) E-plane)

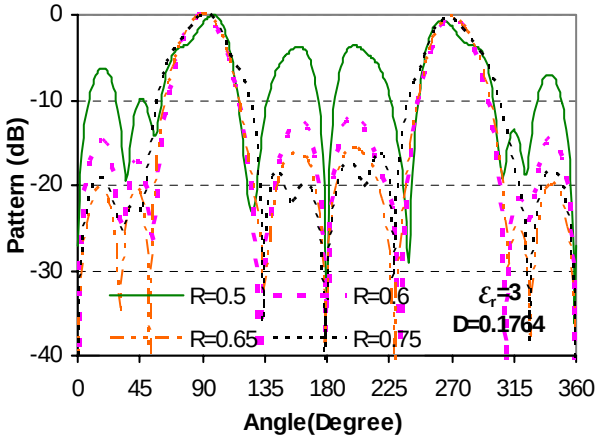

(b) H-plane

Fig. 9. The computed far field patterns of the slot-pair.

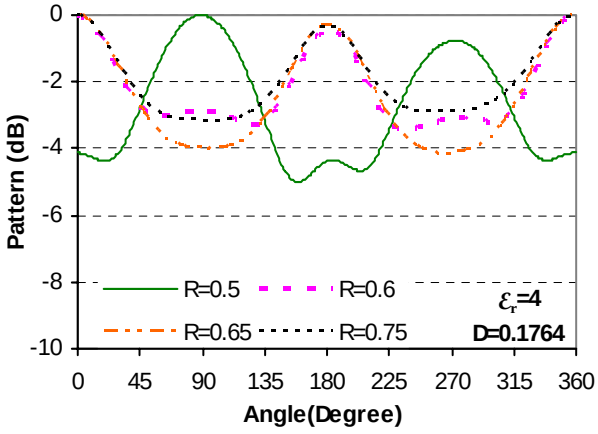

(a) E-plane

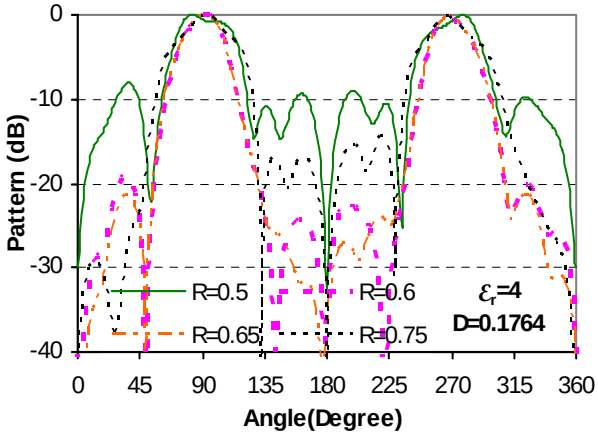

(b) H-plane.

Fig. 10. The computed far field patterns of the slot-pair.

Finally, the radiation patterns are obtained for a depth of 0.25 λ and different radii (R) and permittivity (ε_r) values. The obtained results are shown in Fig. 11. The E-plane and H-plane patterns are found both very good and the distortion due to the radome is very minimal. It is shown that when the radome is designed, the radii (R) of the cylindrical radome are preferably chosen as 0.6λ and 0.65λ so as to provide desired antenna patterns.

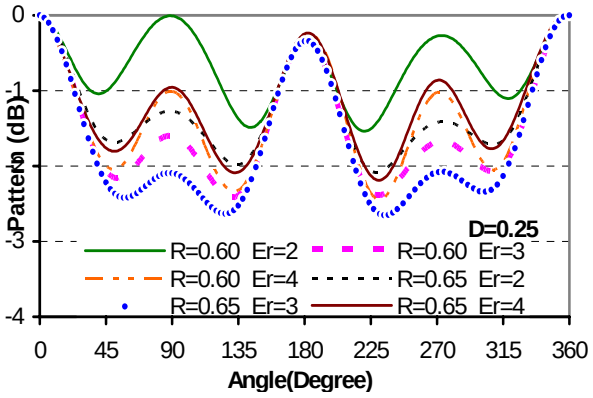

(a) E-plane.

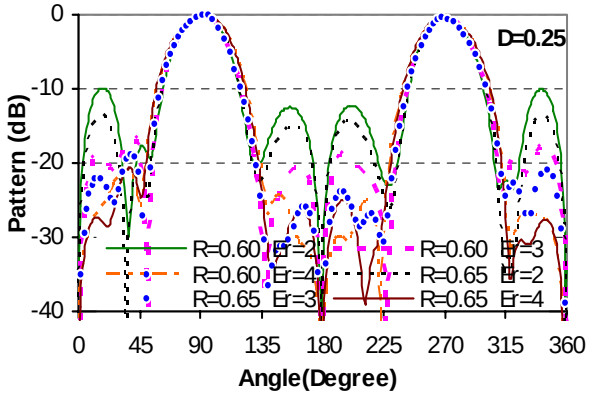

(b) H-plane.

Fig. 11. The computed far field patterns of the slot-pair where Er denotes permittivity.

IV. CONCLUSION

In this paper, the method of moments is employed to analyze waveguide slot antenna in the presence of a dielectric radome. The detailed electromagnetic field integral equation formulations for radiation (and scattering) by these antennas (and scatterer) of arbitrarily shaped 3D geometry are carried out. The Galerkin's MoM procedure is utilized to solve the integrate equations. Some numerical examples are considered and their results are shown to verify the correctness of formulations and capability of our numerical codes. The waveguide slot antennas with radome (as the examples) are analyzed in detail.

REFERENCES

[1] T. Takeshima, "X-band omnidirecrectional double-slot array antenna," *Electron Eng.*, vol. 39, pp. 617–621, Oct. 1967.

[2] S. W. LÜ, "Study of properties of slot-pair in waveguide," *ACTA Electronica Sinica*, vol. 16, pp. 104–107, Sept. 1988. (in Chinese)

[3] R. W. Lyon and A. J. Sangster, "Efficient moment method analysis of radiating slots in a thick-walled rectangular waveguide," *Proc. Inst. Elect. Eng. Part H*, vol. 128, pp. 197–205, Aug. 1981.

[4] A. J. Sangster and H. Wang, "Resonance properties of omnidirectional slot doublet in rectangular waveguide," *Electronics Letters*, vol. 29, no. 1, pp. 16–18, 1993.

[5] J. Y. Li, L. W. Li, and Y. B. Gan, "Method of moments analysis of waveguide slot antennas using the EFIE," *Journal of Electromagnetic Waves and Applications*, vol. 19, no. 13, pp. 1729-1748, 2005.

[6] K. Umashankar, A. Taflove, and S. M. Rao, "Electromagnetic scattering by arbitrary shaped three-dimensional homogeneous lossy dielectric objcts," *IEEE Trans. on Antennas and Propagation,* vol. 34, no. 6, pp. 758–766, June 1986.

[7] B. M. Kolundzija, "Electromagnetic modeling of composite metallic and dielectric structures," *IEEE Trans. on microwave theory and techniques,* vol. 47, no. 7, pp. 1021–1032, July 1999.

[8] J. Y. Li and L. W. Li, "Electromagnetic scattering by a mixture of conducting and dielectric objects: analysis using method of moments," *IEEE Trans. on Vehicular Technology,* vol. 53, no. 2, pp. 514–520, 2004.

[9] S. M. Rao, D. R. Wilton, and A. W. Glisson, "Electromagnetic scattering by surfaces of arbitrary shape, " *IEEE Trans. on Antennas and Propagation,* vol. 30, no. 5, pp. 409–418, May 1982.

Jian-Ying Li received the degrees of B.Sc. in Mathematics, and M.Eng.Sc. and Ph.D. both in Electromagnetic Field and Microwave Technology from Henan Normal University, Xinxiang, China, in 1986, and Xidian University, Xi'an, China, in 1992 and 1999, respectively. From 1992 to 1996, he worked at Xi'an Electronic Engineering Research Institute, Xi'an, China as a Research&Design Engineer. From 1999 to 2001, he was with the Department of Electrical and Computer Engineering at the National University of Singapore (NUS) where he was a Postdoctoral Research Fellow. From 2001 to 2003, he was with High Performance Computation for Engineered Systems (HPCES)

Programme at the Singapore-MIT Alliance (SMA), as a Research Fellow. Currently, he is a Research Scientist of Temasek Laboratories, National University of Singapore. His main research interests include fast algorithms in computational electromagnetics, wave propagation and scattering, design and analysis of phased arrays, waveguide slot antennas, and microstrip antennas, and broadband electrical small antennas etc.

Jing-Li Guo received the B.Eng. and M.Eng., and Ph.D degrees all in Electronic Engineering from Xidian University, Xi'an, China, China in 1999, 2002 and 2005, respectively.

Currently, she is a Lecturer in the National Key Laboratory of Antennas and Microwave Technology, Xidian University. Her research interests include antenna array, broadband miniature antenna analysis and design, computation electromagnetic, and EMC.

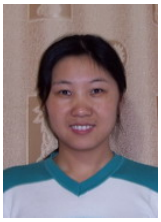

Yan-Lin Zou received the B.Eng. and M.Eng. degrees in electronic engineering from Xidian University, Xi'an, China, in 2002 and 2005, respectively. Currently, she is a Doctor candidate and a Lecturer in the National Key Laboratory of Antennas and Microwave Technology, Xidian University. Her research interests include smart antenna, broadband electrically small antenna, antenna array, computation electromagnetic.

Qi-Zhong Liu was born in Sichuan, China, in 1938. He is now a professor of the National Key Laboratory of Antennas and Microwave Technology, Xidian University. He is the editorial member of Chinese Journal of Radio Science and the senior member of Chinese Institute of Electronics. His research interests include analysis and design of array antenna, smart antenna, broadband miniature antenna, computation of RCS, and EMC.

Beam Squint Using Integrated Gyrotropic Phase Shifter

S. S. Iqbal and M. R. Ali

KFUPM, Dhahran 31261, Saudi Arabia
sheikhsi@kfupm.edu.sa

Abstract − Gyrotropic planar phase shifters are widely used to control the radiation properties of phased array antennas. The design and performance of a microstrip array antenna with integrated ferrite phase-shifter are described. Calculated tunable differential phase shift and simulated beam scanning properties of the linear phased array antenna are presented and corroborated with measured results.

I. INTRODUCTION

The revolution in PCB techniques and the recent availability of low loss and commercially viable microwave ferrites have renewed the interest in printed antennas on ferrite substrate. When magnetized, ferrite substrates offer greater agility in controlling the beam steering and pattern shaping characteristics of the microstrip array antennas [1, 2]. The high dielectric constant of the ferrite brings a reduction in the antenna dimension [3] and the inherent anisotropy and non-reciprocal behavior of this media is often used to achieve frequency tuning and polarization diversity [4]. In this paper, a microstrip array antenna with integrated phase shifter is realized on a transversely magnetized planar ferrite substrate. Tunable progressive phase shift is achieved by varying the magnetic bias that changes the permeability of ferrite material, which in turn changes the phase velocity, hence, the insertion phase of the propagating microwave signal. Analytical methods are used to calculate the tunable differential phase shift of the microstrip phase shifter, integrated with the four-way Wilkinson type array feeder. Commercial CAD software is used to analyze the impedance matching and the beam scanning properties of the designed microstrip linear phased array antenna. The simulated responses are verified using the measured results, obtained from a vector network analyzer and an antenna measurement system.

II. METHOD OF ANALYSIS

The parallel plate waveguide has long been used to study the electromagnetic wave propagation in planar microstrip structures [3]. An analytical method is used here to predict the phase shift properties of an externally magnetized ferrite filled parallel plate waveguide. In the presence of a transversely applied biasing magnetic field, the gyromagnetic behavior of ferrite material is described by its tensor permeability,

$$[\mu_r] = \begin{bmatrix} \mu & 0 & -j\kappa \\ 0 & \mu_z & 0 \\ j\kappa & 0 & \mu \end{bmatrix} \tag{1}$$

where

$$\mu = 1 + \frac{\gamma^2 (H_0 - MN) M}{\gamma^2 (H_0 - MN)^2 - f^2}, \quad \kappa = \frac{\gamma M f}{\gamma^2 (H_0 - MN)^2 - f^2}.$$

The symbol 'H_0' is the external biasing field, 'f' is the signal frequency, 'γ' is the gyromagnetic ratio, 'M' is the magnetization, and 'N' is the demagnetization factor of the planar (μ_z=1) ferrite material. Thus, for a lossless and transversely (y-directed) magnetized ferrite filled parallel plate waveguide, substituting the tensor permeability ($[\mu_r]$) and the boundary conditions into Maxwell's equation, the derived characteristic equation can be written as,

$$\frac{-\beta^2 + K_0^2 \varepsilon_r}{-\beta^2 + K_0^2 \mu \varepsilon_r} \left\{ -\beta^2 \mu + K_0^2 \mu \varepsilon_r \mu_{eff} \right\} = \left\{ (2m+1) \frac{\pi}{d} \right\}^2 \tag{2}$$

where, '$2d$' is the separation between plates, '$K_0 = \omega\sqrt{(\mu_0 \varepsilon_0)}$', '$\mu_{eff} = (\mu^2 - \kappa^2)/\mu$' and '$m$' determines the mode of operation. Since the resonance conditions in magnetized ferrites are associated with singular value of effective permeability ($\mu_{eff} \to \infty$), this analysis is restricted to modes operating at magnetic bias below resonance region.

III. DESIGN AND RESULTS

The phase-constant (β) and the external bias field (H_0) solution of equation (2) is plotted in Fig. 1, for a ferrite filled parallel plate structure. Note the sharp changes in the insertion phase near the resonance region, where β can be tuned significantly by slightly varying the biasing field. While designing the ferrite based microstrip integrated array feeder, Pucels analytical expressions [5]

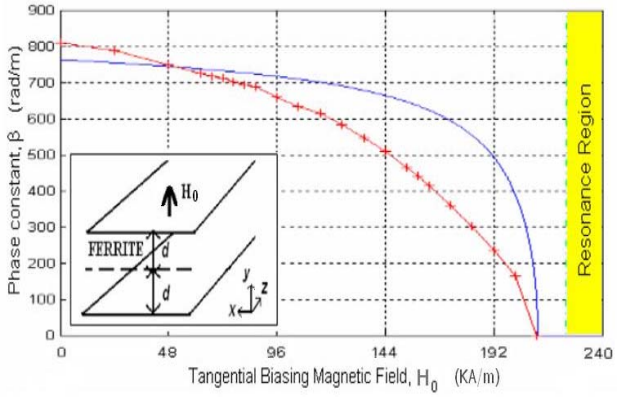

Fig. 1. Tunable phase constants for parallel plate waveguide filled with transversely magnetized ferrite at f=10GHz. (M_s=63 KA/m, ε_r=14, ΔH=10 Oe, d=0.2mm).

are used to calculate the required microstrip parameters. Figure 2 (a) shows the integrated array feeder, designed to provide 360° progressive phase shift on an unbiased (H_0=0 KA/m) ferrite substrate. The spacing in x-axis is carefully selected to provide adequate space for realizing radiating patches that generate a broadside radiation.

The scattering parameters of the array feeder are plotted in Fig. 2 (b). Note that the reflection (S_{11}, S_{22}, S_{33}, S_{44}) and isolation (not shown) parameters exhibit acceptable responses (below -20dB), whereas the transmission parameters (S_{21}, S_{31}, S_{41}, S_{51}) display unequal amplitudes of the patch excitation signals. Since the excitation amplitudes also depend on the external biasing field, this apparent disadvantages of the ferrite substrate can be exploited to design a non-uniform phased array antenna, which requires a different excitation amplitude and phase for each radiating element.

Figure 3 superimposes the simulated and experimental reflection responses ($|S_{11}|$) of the 4-element linear array antenna based on dielectric-ferrite composite substrate. The picture of the fabricated antenna is also shown in the inset of Fig. 3.

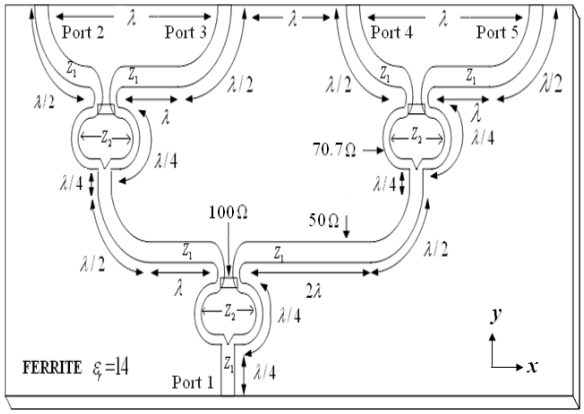

(a)

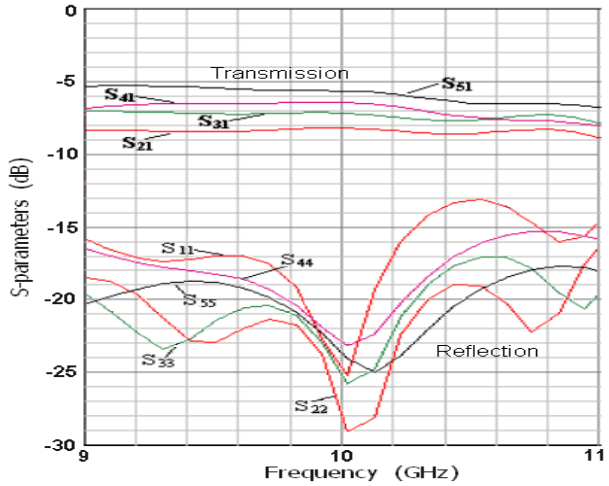

(b)

Fig. 2. (a) Ferrite based integrated array feeder to provide 360° progressive phase shift. (b) Reflection and transmission responses of the 4-port array feeder.

Note that a quarter wavelength transformer is used to match the impedance of the radiating patches with array feeder. Although the array antenna is designed to operate at 10 GHz, the discrepancy between these responses is mainly due to computational and fabrication related limitations. Since basic microstrip array is inherently a narrow band device, the impedance bandwidth for the designed antenna array is observed to be 6.5%. The radiation properties of the antenna also exhibited acceptable responses, such as, gain of 14 dB, beam-width of 28° and main-to-side lobe ratio of -16 dB.

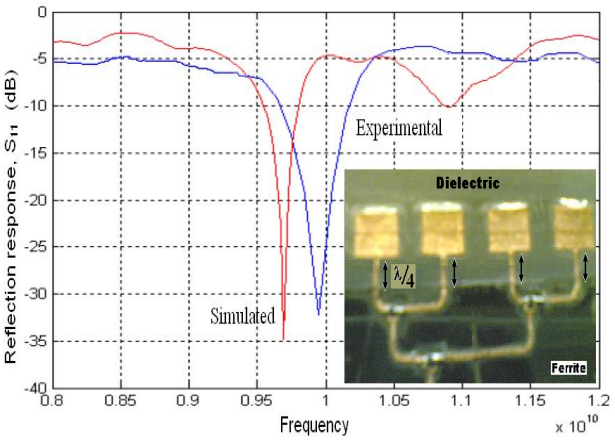

Fig. 3. Simulated and experimental reflection responses of the un-magnetized 10 GHz, 4-element composite linear array antenna (shown in the inset of the figure).

The beam scanning properties of the array antenna is shown in Fig. 4. The simulated angles of the squinted main beam for six different magnetic biases are shown in

Fig. 4 (a), and related measured results are shown in Fig. 4 (b). Note that for magnetic biases up to 150 KA/m, the main beam is steered by a very small angle ($\approx 3^0$). But, when the biasing field is increased from 200 KA/m to 240 KA/m, the main beam is observed to squint by 23^0, where the beam directions are observed at -7^0, -14.5^0, -19.7^0 and -22.5^0 degrees for external basing fields of 200 KA/m, 225 KA/m, 235 KA/m and 240 KA/m, respectively. Although increasing magnetic fields produces sharp beam scanning, it also biases the ferrite material close to lossy ferrimagentic resonance. So a compromise is essential between the acceptable losses and the required sharp changes in progressive phase shift that leads to larger angle of the beam squint.

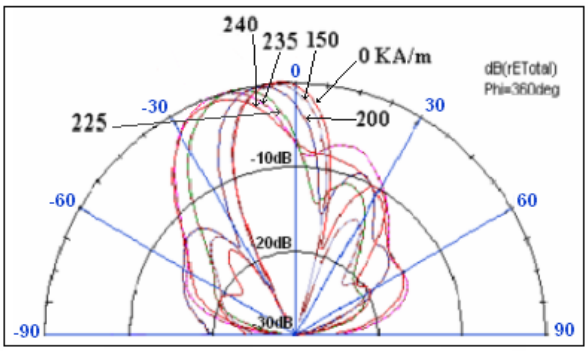

(a)

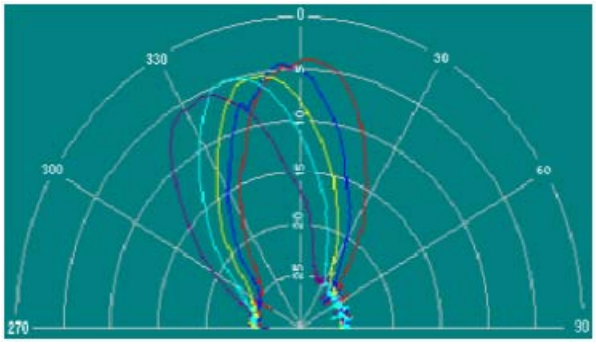

(b)

Fig. 4. (a) Simulated and (b) Measured radiation response of the ferrite based 4-element linear array for six specific external magnetic bias (in y-axis).

IV. CONCLUSION

A linear phased array antenna based on composite dielectric-ferrite substrate is presented. The tunable insertion phase of the integrated microstrip phase shifter is investigated. Steep phase variation is observed near ferromagnetic resonance region, although the amplitudes of the patch excitation signals are observed to be unequal. The radiation response demonstrated significant beam squint for a small variation of magnetic bias and without major degradation of the antenna properties.

ACKNOWLEDGEMENT

The authors are thankful to "King Fahd University of Petroleum & Minerals (KFUPM)" for the support during the research work.

REFERENCES

[1] J. C. Batchelor, *et. a.l*, "Scanned microstrip arrays using simple integrated Ferrite phase shifters," *IEE Proc. Microwave Antennas Prop.*, vol. 147, no. 3, pp. 237-241, 2000.

[2] A. Henderson and J. R. James, "Magnetized microstrip antenna with pattern control," *Electronics Letter*, vol. 24, no. 1, pp. 45-47, 1988.

[3] D. M. Pozar, "Radiation and scattering characteristics of microstrip antennas on normally biased ferrite substrates," *IEEE Trans. Antennas Propagation*, vol. 40, no. 9, pp. 1084-1092, 1992.

[4] P. J. Rainville and F. J. Harackiewiz, "Magnetic tuning of a microstrip patch antenna fabricated on a ferrite file," *IEEE Microwave and Guided Wave Letters*, vol. 2, pp. 483-485, 1992.

[5] R. A. Pucel and D. J. Masse, "Microstrip propagation on magnetic substrates- Part1: design theory," *IEEE Trans. Microwave Theory and Tech.*, vol. 20, no. 5, pp. 304-308, 1972.

Sheikh Sharif Iqbal finished his MSc and Phd degrees in Electrical Engineering from University of Manchester Institute of Science and Technology, UK in 1992 and 1996, respectively. In 1997 he started his teaching career as an assistant professor in the EE department of Islamic Institute of Techonology (IIT), Bangladesh and a year later joined the EE department of King Fahd University of Petroleum and Mineral (KFUPM), Saudi Arabia. Dr Sheikh also worked as post doctoral research fellow in the Telecommunication Research Center of Arizona State University, USA and in UMIST, Manchester, UK during the summer terms of 2001 and 2000, respectively.

Mir Riyaz Ali completed his MSc degree from the EE department of King Fahd University of Petroleum and Mineral (KFUPM), Saudi Arabia in Dec., 2005.

Coplanar Waveguide Slot-coupled K_a-band Patch Antenna for Integration with Wafer-scale Beam-steering MEMS Control Board

S. D. Keller

U.S. Army Research Laboratory
2800 Powder Mill Road
Adelphi, MD 20783
steven.keller4@arl.army.mil

Abstract – A coplanar waveguide (CPW) slot-coupled K_a-band patch antenna is designed, constructed and tested for subsequent integration with a wafer-scale MEMS-switched antenna array beam-steering control board. The antenna is designed for fabrication on a high resistivity silicon (HRS) wafer ($\varepsilon_r \approx 11.8$) for operation with 25-30 GHz satellite communication systems. A simulated 10 dB return loss bandwidth of 2.96 GHz (9.8 %) is achieved with a 4.6 dB peak gain and 110° half-power beamwidth (HPBW). A scaled prototype at 6 GHz is constructed on RT/Duroid 6010 substrate ($\varepsilon_r \approx 10.2$) and yields a measured bandwidth of 360 MHz (6.0 %) and a peak gain of 4 dB. A CPW feedline / slot misalignment sensitivity test is conducted through simulations to investigate the effects that fabrication errors may have on antenna performance during wafer-scale integration of the patch antenna onto the HRS substrate. Simulation results show that slot misalignment less than 200-400 μm should only minimally affect antenna performance, with the most significant degradation being a 2.5 – 4.0 % drop in antenna bandwidth. The successful design of this patch antenna demonstrates a compact, efficient method for integration of a CPW slot-coupled K_a-band patch antenna onto a wafer-scale MEMS control board without the need for additional substrate layers or feedline interconnects, minimizing total system weight and fabrication complexity.

Keywords: Coplanar waveguide, patch antenna, wafer-scale, and MEMS.

I. INTRODUCTION

Several key metrics including size, efficiency, and affordability must be optimized when Army communication systems are designed. With this in mind, research on embodiments of a compact, efficient microwave electronic scanning array (ESA) has been proposed for integration with future battlefield platforms. One such ESA involves a K_a-band aperture-coupled patch antenna array as the radiating element on a wafer-scale MEMS-switched control board for a lightweight, compact electronically-controlled beam and null steering unit for satellite communication systems. Integration of a patch antenna array onto such a wafer-scale control board requires a design approach that differs from the traditional aperture-coupled microstrip patch antenna technique, since the feedlines that extend from the MEMS switching elements are typically coplanar waveguide (CPW) structures. The design, simulation and testing of a single K_a-band patch antenna will be discussed, with a focus on its future integration with a CPW-fed wafer-scale MEMS-switched control board.

II. DESIGN APPROACH

The first step in the design of a K_a-band patch antenna for integration with a wafer-scale MEMS control board is to develop a solid understanding of the wafer structure and the MEMS-switched beam/null-steering control board design. The MEMS switches are fabricated onto a 4" diameter, 500 μm thick high resistivity silicon (HRS) wafer ($\varepsilon_r \approx 11.8$, $\tan(\delta) \approx 0.02$, $\sigma < 0.01$ S/m) with gold trace used for the transmission lines and the ground plane. While microstrip feed lines are typically used for aperture-coupled patch antennas, CPW transmission lines are most easily fabricated on the HRS wafer where the MEMS switching elements reside. While research on this topic has been scarce, especially prior to the early 1990s, the recent interest in incorporating active antennas into monolithic microwave integrated circuits (MMICs) has yielded a number of papers that detail promising techniques for CPW aperture coupling. One such technique involves two substrates, with the CPW line on the lower surface of the bottom substrate. A ground plane with an aperture is placed on the upper surface of this substrate and a second substrate is placed on top of this structure, with a patch antenna located on its upper surface. The CPW line couples energy through the aperture to the patch antenna similar to the traditional microstrip aperture coupling approach [1-3]. Another technique involves a single substrate and completely eliminates the need for an embedded aperture and ground plane between two separate substrates [4, 5]. With this

technique, a patch antenna is fabricated on the upper surface of a substrate and a CPW feedline is fabricated on the lower surface, with a coupling slot integrated beneath the patch at the end of this feedline. The CPW feedline couples energy directly through this slot to the patch. One recent embodiment of this approach incorporated a novel tuning stub into the CPW feedline for important reactive tuning for better impedance matching [5].

The integration of a K_a-band patch antenna with a CPW-fed MEMS control board required careful consideration of fabrication ease and substrate dimension constraints. A center frequency of ~30 GHz was chosen in order to facilitate the usage of a final wafer-scale MEMS-switched antenna array based on this design as the uplink mechanism for a typical satellite communication system. At 30 GHz, the 500 µm HRS substrate tended to be too thick to serve as the lower substrate in a two-substrate aperture-coupling setup. Test simulations in HFSS yielded a much higher bandwidth of ~6-7% using the single-substrate CPW aperture-coupling method [4, 5] than the ~1-2% bandwidth yielded by the two-substrate method [1-3]. In addition to this notable bandwidth improvement, the single-substrate technique also reduces fabrication complexity by incorporating the control board and antenna on the same structure and reduces the weight of the final unit by eliminating the need for additional substrate layers to be bonded to the HRS wafer. Thus, the single-substrate CPW slot-coupling method was chosen for the final 30 GHz patch antenna design, with the tuning stub pioneered in [5] included for reactive tuning.

III. WAFER-SCALE PATCH ANTENNA DESIGN/SIMULATION

A CPW slot-coupled patch antenna was then designed from patch antenna and coplanar waveguide theory [6, 7] and was simulated and fine-tuned in *Ansoft* HFSS [8] and *EMAG* EMPiCASSO [9], with the CPW feedline incorporated into the ground plane of the HRS substrate and a tuning stub included for reactive impedance matching. The final antenna design is shown in Fig. 1, with detailed dimensions and substrate properties listed in Table 1.

The simulated return loss for this CPW slot-coupled patch antenna design is shown in Fig. 2. In HFSS, an excellent resonance at ~30.2 GHz was obtained after the patch antenna dimensions and CPW feedline characteristics were fine-tuned accordingly from theoretical values to their final values listed in Table 1, with a resulting 10 dB return loss bandwidth of ~2.96 GHz (9.8 %), from 28.59 – 31.55 GHz. The EMPiCASSO return loss results exhibit a center frequency shift up to ~30.5 GHz and a 10 dB return loss bandwidth decreases down to ~1.62 GHz (5.3 %), from 29.69 – 31.31 GHz. The causes of these small discrepancies between the HFSS and EMPiCASSO results will be discussed when the measured data for a scaled prototype is presented.

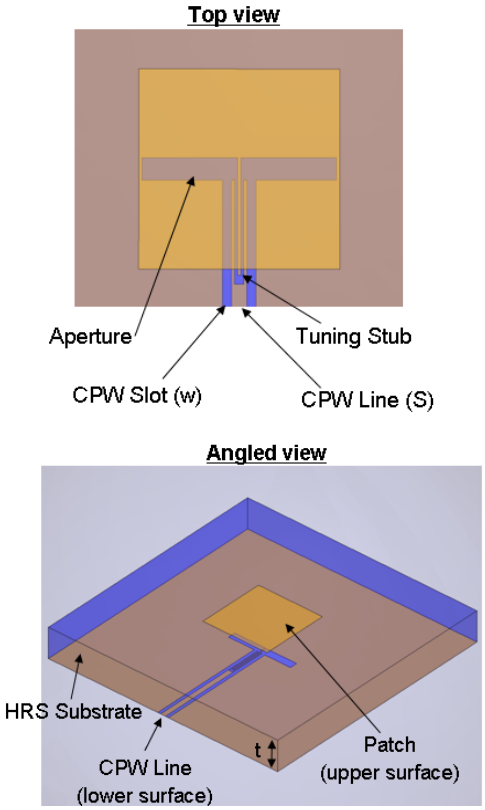

Fig. 1. HFSS model of a 30 GHz CPW slot-coupled patch antenna.

Table 1. 30 GHz CPW slot-coupled patch antenna design parameters.

Variable	Dimensions
Patch	1115 x 1115 µm
Substrate	4000 x 4000 µm, t = 500 µm
CPW line width (S)	85 µm
CPW slot width (w)	50 µm
Slot dimensions	1078 x 124 µm
Tuning stub length (from bottom edge of aperture)	530 µm
Substrate material properties	$\varepsilon_r \approx 11.8$, $\tan(\delta) \approx 0.015$, $\sigma <$ 0.01 S/m
Patch / CPW feedline material properties	Gold trace: $\sigma \approx 4.7e07$ S/m, t = 0.75 µm

The simulated gain for this antenna design is shown in Fig. 3. The peak gain occurs at 0° and is ~4 dB, with a half-power beamwidth (HPBW) of ~110°. The low gain value is mainly attributed to the lossy HRS wafer that the antenna resides upon, with a high dielectric constant, relatively large thickness, and low resistivity compared to most low-loss substrates used for traditional patch antenna designs. This reduction in gain has been deemed a fair tradeoff for the ease of fabrication and unit weight reduction that results from the single-substrate integration of the antenna directly onto the HRS wafer.

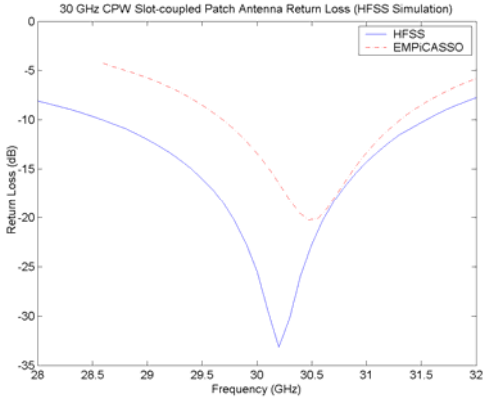

Fig. 2. HFSS-simulated S_{11} data for 30 GHz CPW slot-coupled patch antenna.

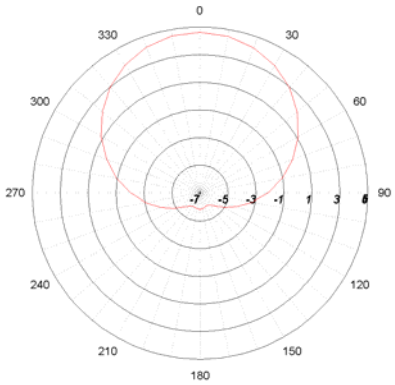

Fig. 3. HFSS-simulated total gain pattern for 30 GHz CPW slot-coupled patch antenna.

IV. SCALED PROTOTYPE ANTENNA SIMULATION/MEASUREMENTS

Since this design was too small to be constructed with an on-site router (6 mil bit size limitation), the antenna frequency was scaled down to 6 GHz in order to increase the structure size enough so that a test unit could be efficiently and accurately fabricated. Detailed dimensions and substrate properties are summarized in Table 2. A single element prototype of this 6 GHz design was then constructed on a 3" x 3", 2.54 mm thick RT/Duroid 6010 substrate ($\varepsilon_r \approx 10.2$) with an end-launch coaxial cable connector soldered to the CPW line. RT/Duroid 6010 substrate was used in place of the HRS wafer due to its reasonably similar dielectric constant, ε_r. A picture of this prototype is shown in Fig. 4. The return loss data for this prototype is shown in Fig. 5.

Table 2. Scaled prototype CPW slot-coupled patch antenna design parameters.

Variable	Dimensions
Patch	5.67 x 5.67 mm
Substrate	76.2 x 76.2 mm, t = 2.54 mm
CPW line width (S)	0.91 mm
CPW slot width (w)	0.41 mm
Slot dimensions	5.45 x 0.57 mm
Tuning stub length (from bottom edge of aperture)	3.25 mm
Substrate dielectric constant	$\varepsilon_r \approx 10.2$

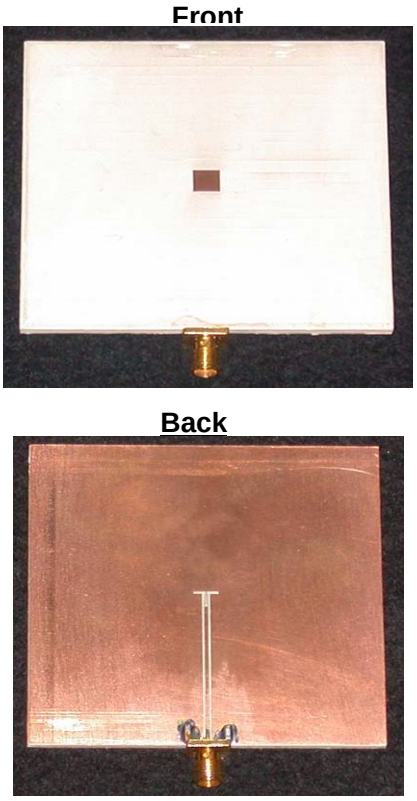

Fig. 4. Fully-constructed 6 GHz scaled prototype of CPW slot-coupled patch antenna.

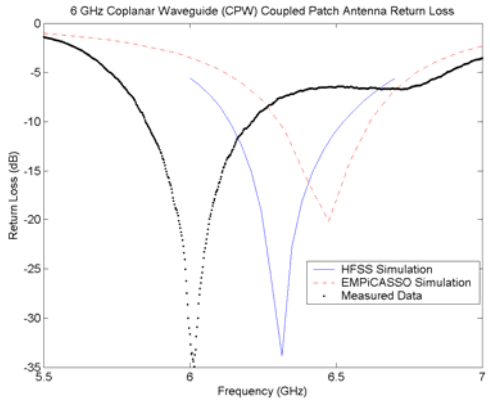

Fig. 5. Measured S_{11} data for 6 GHz prototype CPW slot-coupled patch antenna.

While the measured return loss for this 6 GHz prototype ended up having a center frequency about ~300-500 MHz lower than the HFSS and EMPiCASSO results, it did confirm the feasibility of the excellent HFSS simulation results of the 30 GHz design. A resonance at ~6.01 GHz was obtained with a 10 dB return loss bandwidth of ~360 MHz (6.0 %), from 5.85 – 6.21 GHz. This measured bandwidth is nearly double the achieved bandwidth of existing single-substrate CPW-fed slot-coupled patch antenna designs [4], [5]. E-plane and H-plane radiation pattern measurements are shown in Figs. 6 and 7.

The resulting peak gain for this prototype was 4.4 dB. While a generally broadside radiation pattern is confirmed by these measurements, a small drop of 1-2 dB is seen in the E-plane radiation pattern between -10° and 15°. HFSS simulation results for the 6 GHz scaled patch antenna with a 3" x 3" substrate, also shown in Figs. 6 and 7, confirms this phenomenon and matches the measured data reasonably well in shape and final realized gain.

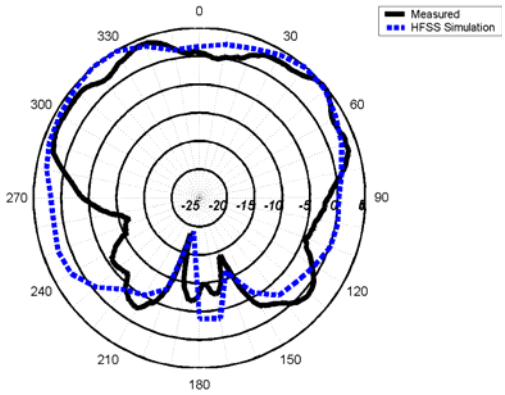

Fig. 6. Measured E-plane radiation pattern data for 6 GHz prototype CPW slot-coupled patch antenna.

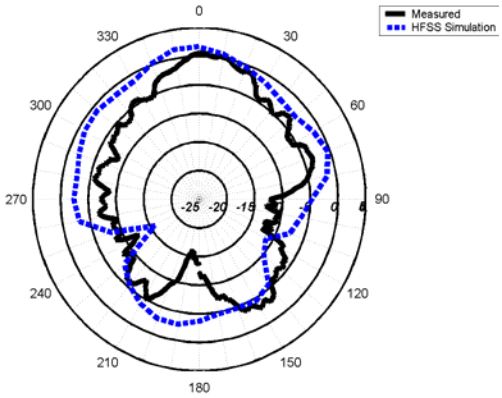

Fig. 7. Measured H-plane radiation pattern data for 6 GHz prototype CPW slot-coupled patch antenna.

The 0° dip in the measured prototype results is a significant deviation from the simulated 30 GHz wafer-scale patch antenna total gain pattern shown in Fig. 3. This simulated patch antenna was placed onto a substrate that was approximately 4 times larger in size than the patch area. The scaled 6 GHz prototype, however, was constructed on a substrate that was 15 times larger than the patch antenna. Increased surface wave radiation from this notable increase in substrate / ground plane size is expected to be the cause of the measured radiation pattern abnormalities. In order to confirm this theory, HFSS simulations were conducted with the 6 GHz scaled prototype design placed on substrates of different sizes. The resulting E-plane and H-plane radiation patterns are shown in Fig. 8 and 9. A slight tilt towards 5° exists in the broadside E-plane pattern maximum with the 1-inch substrate, but the 0° power loss is significantly mitigated. The general trend observed from comparing this simulation data is that the overall radiation pattern tends to become a more efficient broadside pattern as the substrate size is decreased. Considering that surface wave contributions to patch antenna radiation increase as the substrate size increases, particularly in the E-plane [10], these results strongly indicate that surface wave diffraction from the substrate edges are the main cause of the slightly-degraded radiation pattern [10-12]. The final wafer-scale patch antenna array will be incorporated onto a silicon wafer approximately 100 times larger (4" x 4") than an individual patch antenna, so techniques for mitigating the effect that this surface wave diffraction has on the final antenna array gain and radiation pattern should be explored further. A promising candidate for reducing this surface wave distortion is the incorporation of an electromagnetic bandgap (EBG) structure [10, 13] or a uniplanar compact photonic bandgap structure (UC-PBG) [14, 15] onto the silicon wafer. The next phase of research for this wafer-scale patch antenna array will focus on the incorporation of such a structure into this design for further optimization of the antenna radiation performance.

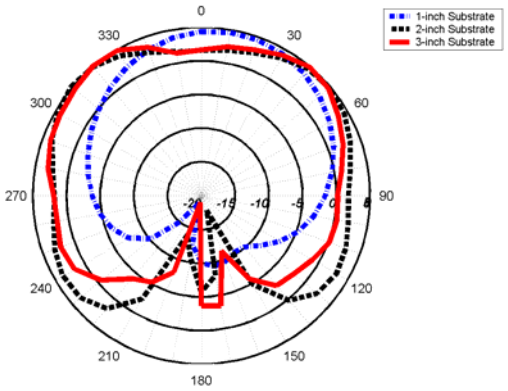

Fig. 8. Effect of substrate/ground plane size on E-plane radiation pattern for 30 GHz wafer-scale patch antenna.

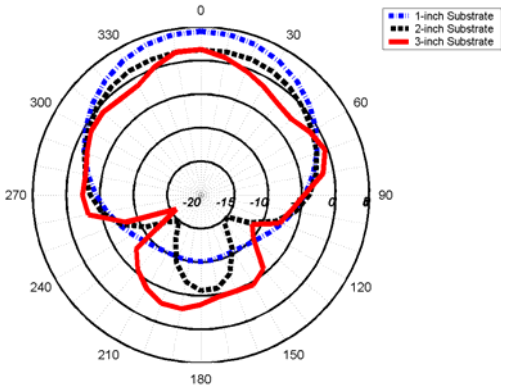

Fig. 9. Effect of substrate/ground plane size on H-plane radiation pattern for 30 GHz wafer-scale patch antenna.

A comparison of the HFSS and EMPiCASSO simulated return loss plots in Fig. 2 and 5 yields a consistent relationship between the two simulation program results for both the 30 GHz wafer-scale design and the 6 GHz scaled prototype design. In both cases, the EMPiCASSO results show less-pronounced resonance at a center frequency about 150 – 200 MHz higher than the HFSS results and exhibits a 2 – 4 % bandwidth decrease. When placed side-by-side with the 6 GHz measured data, the HFSS simulation results are much closer than the EMPiCASSO simulation data, yielding a very similar resonance shape and bandwidth and only having a +300 MHz center frequency shift versus the less comparable resonance shape and +475 MHz shift that the EMPiCASSO results displayed. The less accurate results obtained by EMPiCASSO are likely attributed to its 2.5D geometry scheme which employs an infinite substrate and ground plane size. The > 300 MHz difference between the simulated and measured results for this prototype could also be attributed to fabrication/measurements inaccuracies and to limitations in the simulation model. Even with these small discrepancies between simulated and measured results, the data obtained from the 6 GHz scaled prototype demonstrate the effectiveness that the 30 GHz wafer-scale design should have when it is fabricated onto an HRS substrate.

V. WAFER-SCALE FABRICATION ERROR SENSITIVITY TEST

When this patch antenna design is fabricated onto an HRS wafer, there is a potential for misalignment between the patch on the upper surface of the wafer and the CPW feedline and slot on the lower surface. Using a photoetching process, this misalignment should be limited to a worst-case offset of ~5 μm. An alignment sensitivity test was conducted in HFSS to predict what effects this misalignment would have on the patch antenna performance. The CPW feedline and slot were both offset from their centered position under the patch antenna by 5 μm along the x-plane and then the y-plane. A diagram of this feedline/slot offsetting strategy is shown in Fig. 10.

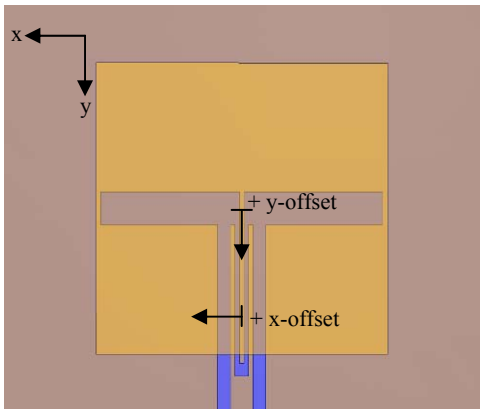

Fig. 10. Offset orientation diagram for CPW feedline / slot alignment sensitivity test.

A comparison of the HFSS-simulated returns loss for these misaligned cases with that of the perfectly-aligned case is shown in Fig. 11. The +/- y-plane offsets were both simulated due to the asymmetry in the y- plane due to the feedline and tuning stub in the + y-plane. However, since symmetry exists in the x-plane, only the + x-plane offset was simulated. The results of these simulations indicate that the worst-case photoetching misalignment should very minimally affect the performance of the wafer-scale patch antenna. The only notable effect seemed to be a +100 MHz center frequency shift with the +5 μm y-plane offset, which may partially be attributed to the model meshing variability between this simulation and that of the perfectly-aligned model and may also result from more of the feedline / tuning stub being shifted under the patch. The bandwidth, peak gain and HPBW remained minimally affected, with approximately the same values for the misaligned cases as those for the perfectly-aligned case.

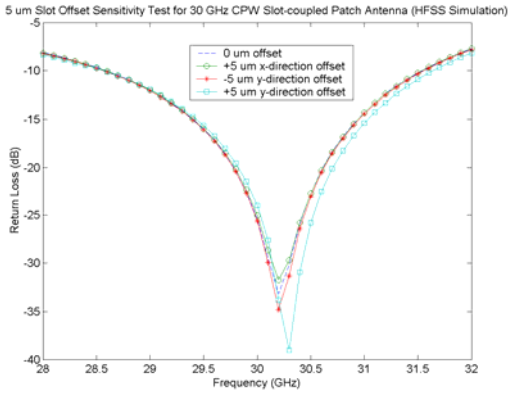

Fig. 11. HFSS-simulated S_{11} of wafer-scale patch antenna with 5 µm slot misalignment.

Next, this sensitivity test was expanded to discover approximately how misaligned the patch antenna and CPW feedline and slot must be in order to have a significant effect on antenna performance. The CPW feedline and slot were both offset from their centered position under the patch antenna at increments of ~54.5 µm in the + x-plane and at larger increments in the +/- y-plane up to the point where no part of the slot resided under the patch.

The results of the x-plane sensitivity test are shown in Fig. 12. These data indicates that a misalignment smaller than ~400 µm should yield a small (~0 to 100 MHz) center frequency shift and a bandwidth reduction down to ~6.5 – 7% (from its original 9.8% value). A misalignment greater than 400 µm may yield a significant return loss increase and consequential loss of resonance. Beyond 550 µm misalignment, the return loss increases above 10 dB for the entire 28 – 32 GHz frequency region of interest.

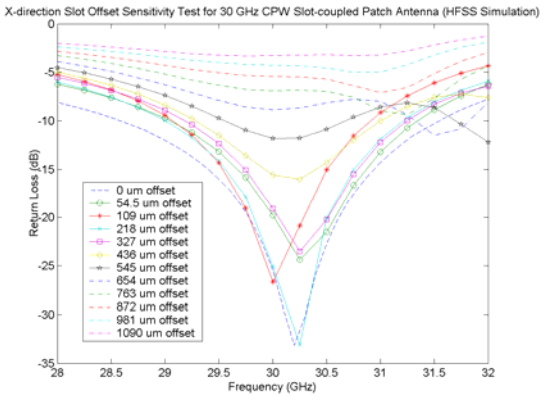

Fig. 12. HFSS-simulated S_{11} for wafer-scale patch antenna x-direction slot alignment sensitivity test.

The results of the y-plane sensitivity test are shown in Fig. 13. These data indicates that misalignment smaller than ~250 µm yields a small (~0 to 100 MHz) center frequency shift and a bandwidth reduction down to ~5.7 – 6.0 % (from its original 9.8 % value). A misalignment greater than 250 µm yields a significant return loss increase and loss of resonance. Beyond 400 µm misalignment, the return loss increases above 10 dB for the entire 28 – 32 GHz frequency region of interest.

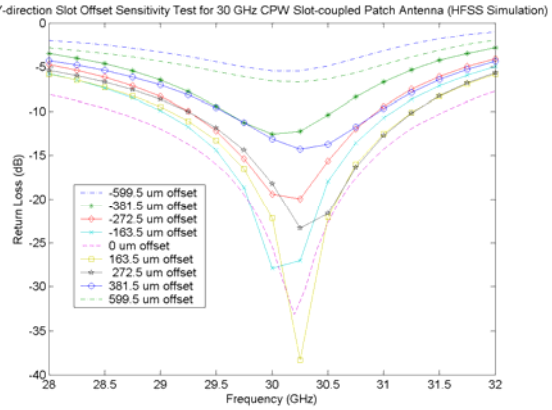

Fig. 13. HFSS-simulated S_{11} for wafer-scale patch antenna y-direction slot alignment sensitivity test.

From these results, the antenna performance is shown to be more sensitive to misalignment in the y-plane, with loss of resonance occurring at a misalignment ~150 µm smaller in the y-plane than in the x-plane. Another notable performance difference between x and y-plane misalignment is that the patch antenna bandwidth appears to be more critically affected by small y-plane misalignment than by x-plane misalignment, suffering a 0.8 – 1.0 % further decrease in bandwidth. Thus, according to these simulation results, a fabrication error of 300 – 400 µm or smaller in the x-plane or 200 – 300 µm or smaller in the y-plane should only cause a small % loss of bandwidth and should minimally affect the antenna resonance at 30 GHz. A very rare photo mask misalignment in the photoetching process could potentially bring about a slot/patch antenna misalignment greater than 300 – 500 µm, but with regards to the more common 0 – 5 µm-range fabrication errors, these tests have shown that the performance of this wafer-scale patch antenna design is considerably robust to slot misalignment.

VI. CONCLUSIONS

A coplanar waveguide slot-coupled K_a-band patch antenna has been successfully designed, constructed and tested for integration with a wafer-scale MEMS-switched antenna array beam-steering control board. HFSS simulation results show a 10 dB return loss bandwidth of 2.96 GHz (9.8 %) with a 4.6 dB peak gain and 110° HPBW. A scaled prototype at 6 GHz that was constructed on RT/Duroid 6010 substrate ($\varepsilon_r \approx 10.2$) yielded a

measured bandwidth of 360 MHz (6.0 %) and a peak gain of 4 dB. The measured bandwidth is nearly double the achieved bandwidth of existing single-substrate CPW-fed slot-coupled patch antenna designs and the promising simulation results for the wafer-scale design indicates the potential for bandwidth improvement of up to 4 times that of previously-reported designs.

The results from a wafer-scale fabrication error sensitivity test indicated that a CPW feedline / slot misalignment less than 200-400 μm should produce minimal degradation of antenna functionality, with the most significant impact being a 2.5 – 4.0 % drop in the antenna bandwidth and a small shift in the center frequency of 100 MHz or less. With wafer-scale fabrication errors on the order of less than 5 μm, the performance of this antenna design should be minimally affected by such circumstances. From this, it may be inferred that the production yield for a final wafer-scale integrated antenna array and MEMS beam-steering control board will not be significantly impacted by the antenna design and will mainly be dependent upon the MEMS switching element yield percentage.

The successful design and implementation of this patch antenna demonstrates a compact, efficient method for integration of a CPW slot-coupled K_a-band patch antenna onto a wafer-scale MEMS-switched control board without the need for additional substrate layers or feedline interconnects. This, in turn, minimizes the total system weight and decreases the wafer-scale fabrication complexity, yielding a lightweight, cost-effective solution for a microwave electronic scanning array for satellite communication.

REFERENCES

[1] R. N. Simons and R. Q. Lee, "Coplanar waveguide aperture-coupled patch antennas with ground plane/substrate of finite extent," *Electronic Letters*, vol. 28, no. 1, pp. 75-76, January 1992.

[2] R. Q. Lee and R. N. Simons, "Coplanar waveguide aperture-coupled microstrip patch antenna," *IEEE Microwave and Guided Wave Letters*, vol. 2, no. 4, pp. 138-139, April 1992.

[3] M. Forman and Z. Popović, "A Ka-band ground-backed CPW balanced and integrated antenna feed," *European Microwave Conference*, October 2000.

[4] W. Menzel and W. Grabherr, "A microstrip patch antenna with coplanar feed line," *IEEE Microwave and Guided Wave Letters*, vol. 1, no. 11, pp. 340-342, November 1991.

[5] K. Hettak, G. Delisle, and M. Boulmalf, "A novel integrated antenna for millimeter-wave personal communications systems," *IEEE Transactions on Antennas and Propagation*, vol. 46, no. 11, pp. 1757-1758, November 1998.

[6] C. A. Balanis, *Antenna Theory, Analysis and Design (2nd edition)*, p. 728-731, John Wiley & Sons, 1997.

[7] W. T. Joines, *Microwave Electronic Circuits*, p. 41, Duke University, 2005.

[8] Ansoft Corporation, High Frequency Structure Simulator (HFSS), http://www.ansoft.com/, 2007.

[9] EMAG Technologies Inc., EMPiCASSO, http://www.emagware.com/ , 2006.

[10] M. Bozzetti, G. Costantini, A. D'Orazio, M. DeSario, V. Petruzzelli, F. Prudenzano, and F. Renna, "Grounded dielectric slab finite size effect on patch antenna radiation patterns," *Electronics Letters*, vol. 39, no. 6, March 2003.

[11] J. Huang, "The finite ground plane effect on the microstrip antenna radiation patterns," *IEEE Transactions on Antennas and Propagation*, vol. 31, no. 4, pp. 649-653, July 1983.

[12] S. Maci, L. Borselli, and L. Rossi, "Diffraction at the edge of a truncated grounded dielectric slab," *IEEE Transactions on Antennas and Propagation*, vol. 44, no. 6, pp. 863-873, June 1996.

[13] F. Yang and Y. Rahmat-Samii, "Microstrip antennas integrated with electromagnetic band-gap (EBG) structures: a low mutual coupling design for array applications," *IEEE Transactions on Antennas and Propagation*, vol. 51, no. 10, pp. 2936-2946, October 2003.

[14] F.-R. Yang, Y. Qian, R Coccioli, and T. Itoh, "A novel low-loss slow-wave microstrip structure," *IEEE Microwave and Guided Wave Letters*, vol. 8, no. 11, pp. 372-374, November 1998.

[15] R. Coccioli, F.-R. Yang, K.-P. Ma, and T. Itoh, "Aperture-coupled patch antenna on UC-PBG substrate," *IEEE Transactions on Microwave Theory and Techniques*, vol. 47, no. 11, pp. 2123-2130, November 1999.

Steven D. Keller received the B.S. degree in electrical and computer engineering from Cornell University, Ithaca, NY, in 2004 and the M.S. and Ph.D. degrees in electrical and computer engineering from Duke University, Durham, NC, in 2006 and 2008, respectively. From 2002 to 2004, he served as a summer intern in the air traffic control division at Sensis Corporation, Dewitt, NY. In 2006 and 2007, he served as a summer intern in the millimeter wave branch of the sensors and electron devices directorate of the US Army Research Laboratory, Adelphi, MD. He recently completed the doctoral program at Duke University, where he conducted research on the integration of high speed semiconductor switching devices with antenna structures under the advisement of Dr. William T. Joines, and co-advisement of Dr. W. Devereux Palmer.

2007 INSTITUTIONAL MEMBERS

AUSTRALIAN DEFENCE LIBRARY
Northcott Drive
Canberra, A.C.T. 2600 Australia

DARTMOUTH COLL-FELDBERG LIB
6193 Murdough Center
Hanover, NH 03755-3560

DSTO-DSTORL EDINBURGH
Jets AU/33851-99, PO Box 562
Milsons Point, NSW
Australia 1565

DTIC-OCP/LIBRARY
8725 John J. Kingman Rd. Ste 0944
Ft. Belvoir, VA 22060-6218

ELSEVIER
Bibliographic Databases
PO Box 2227
Amsterdam, Netherlands 1000 CE

ENGINEERING INFORMATION, INC
PO Box 543
Amsterdam, Netherlands 1000 Am

ETSE TELECOMUNICACION
Biblioteca, Campus Lagoas
Vigo, 36200 Spain

FGAN-FHR
Neuenahrerstrasse 20
Wachtberg, Germany 53343

FLORIDA INTERNATIONAL UNIV
10555 W. Flagler Street
Miami, FL 33174

GEORGIA TECH LIBRARY
225 North Avenue, NW
Atlanta, GA 30332-0001

HANYANG UNIVERSITY
Paiknam Academic Info. Ctr Library
17 Haengdang-Dong
Seongdong-Ku
Seoul, South Korea 133-791

HRL LABS, RESEARCH LIBRARY
3011 Malibu Canyon
Malibu, CA 90265

IEE INSPEC/Acquisitions Section
Michael Faraday House
6 Hills Way
Stevenage, Herts UK SG1 2AY

INSTITUTE FOR SCIENTIFIC INFO.
Publication Processing Dept.
3501 Market St.
Philadelphia, PA 19104-3302

IPS RADIO & SPACE SERVICES
PO Box 1386
Haymarket NSW Australia 1240

LIBRARY – DRDC OTTAWA
3701 Carling Avenue
Ottawa, Ontario, Canada K1A OZ4

LIBRARY of CONGRESS
Reg. Of Copyrights
Attn: 40T Deposits
Washington DC, 20559

LINDA HALL LIBRARY
5109 Cherry Street
Kansas City, MO 64110-2498

MISSISSIPPI STATE UNIV LIBRARY
PO Box 9570Mississippi State, MS
39762

MIT LINCOLN LABORATORY
Periodicals Library
244 Wood Street
Lexington, MA 02420

NAVAL POSTGRADUATE SCHOOL
Attn:J. Rozdal/411 Dyer Rd./ Rm 111
Monterey, CA 93943-5101

NDL KAGAKU
C/0 KWE-ACCESS
PO Box 300613 (JFK A/P)
Jamaica, NY 11430-0613

OHIO STATE UNIVERSITY
1320 Kinnear Road
Columbus, OH 43212

OVIEDO LIBRARY
PO BOX 830679
Birmingham, AL 35283

PENN STATE UNIVERSITY
126 Paterno Library
University Park, PA 16802-1808

CHRIS A. PENWELL
3500 LONG DRIVE
MINDER, NV 89423

PHILIPS RESEARCH LABORATORY
Cross Oak Lane, Stella Cox
Salfords, Redhill
UK RH1 5HA

DAVID J. PINION
1122 E PIKE STREET #1217
SEATTLE, WA 98122

SOUTHWEST RESEARCH
INSTITUTE
6220 Culebra Road
San Antonio, TX 78238

SWETS INFORMATION SERVICES
160 Ninth Avenue, Suite A
Runnemede, NJ 08078

TECHNISCHE UNIV. DELFT
Mekelweg 4, Delft, Holland, 2628 CD
Netherlands

TELSTRA
TRL/M2/770 Blackburn Road
Clayton, Victoria, Australia 3168

TIB & UNIV. BIB. HANNOVER
DE/5100/G1/0001
Welfengarten 1B
Hannover, Germany 30167

TU DARMSTADT
Schlossgartenstrasse 8
Darmstadt, Hessen
Germany D-64289

UNIV OF CENTRAL FLORIDA LIB.
4000 Central Florida Boulevard
Orlando, FL 32816-8005

UNIV OF COLORADO LIBRARY
Campus Box 184
Boulder, CO 80309-0184

UNIV OF MISSOURI-ROLLA LIB.
1870 Miner Circle
Rolla, MO 65409-0001

USAE ENG. RES. & DEV. CENTER
Attn: Library/Journals
72 Lyme Road
Hanover, NH 03755-1290

ACES COPYRIGHT FORM

This form is intended for original, previously unpublished manuscripts submitted to ACES periodicals and conference publications. The signed form, appropriately completed, MUST ACCOMPANY any paper in order to be published by ACES. PLEASE READ REVERSE SIDE OF THIS FORM FOR FURTHER DETAILS.

TITLE OF PAPER:

AUTHORS(S)

PUBLICATION TITLE/DATE:

RETURN FORM TO:

Dr. Atef Z. Elsherbeni
University of Mississippi
Dept. of Electrical Engineering
Anderson Hall Box 13
University, MS 38677 USA

PART A - COPYRIGHT TRANSFER FORM

(NOTE: Company or other forms may not be substituted for this form. U.S. Government employees whose work is not subject to copyright may so certify by signing Part B below. Authors whose work is subject to Crown Copyright may sign Part C overleaf).

The undersigned, desiring to publish the above paper in a publication of ACES, hereby transfer their copyrights in the above paper to The Applied Computational Electromagnetics Society (ACES). The undersigned hereby represents and warrants that the paper is original and that he/she is the author of the paper or otherwise has the power and authority to make and execute this assignment.

Returned Rights: In return for these rights, ACES hereby grants to the above authors, and the employers for whom the work was performed, royalty-free permission to:

1. Retain all proprietary rights other than copyright, such as patent rights.
2. Reuse all or portions of the above paper in other works.
3. Reproduce, or have reproduced, the above paper for the author's personal use or for internal company use provided that (a) the source and ACES copyright are indicated, (b) the copies are not used in a way that implies ACES endorsement of a product or service of an employer, and (c) the copies per se are not offered for sale.
4. Make limited distribution of all or portions of the above paper prior to publication.
5. In the case of work performed under U.S. Government contract, ACES grants the U.S. Government royalty-free permission to reproduce all or portions of the above paper, and to authorize others to do so, for U.S. Government purposes only.

ACES Obligations: In exercising its rights under copyright, ACES will make all reasonable efforts to act in the interests of the authors and employers as well as in its own interest. In particular, ACES REQUIRES that:

1. The consent of the first-named author be sought as a condition in granting re-publication permission to others.
2. The consent of the undersigned employer be obtained as a condition in granting permission to others to reuse all or portions of the paper for promotion or marketing purposes.

In the event the above paper is not accepted and published by ACES or is withdrawn by the author(s) before acceptance by ACES, this agreement becomes null and void.

AUTHORIZED SIGNATURE — TITLE (IF NOT AUTHOR)

EMPLOYER FOR WHOM WORK WAS PERFORMED — DATE FORM SIGNED

Part B - U.S. GOVERNMENT EMPLOYEE CERTIFICATION

(NOTE: if your work was performed under Government contract but you are not a Government employee, sign transfer form above and see item 5 under Returned Rights).

This certifies that all authors of the above paper are employees of the U.S. Government and performed this work as part of their employment and that the paper is therefor not subject to U.S. copyright protection.

AUTHORIZED SIGNATURE — TITLE (IF NOT AUTHOR)

NAME OF GOVERNMENT ORGANIZATION — DATE FORM SIGNED

PART C - CROWN COPYRIGHT

(NOTE: ACES recognizes and will honor Crown Copyright as it does U.S. Copyright. It is understood that, in asserting Crown Copyright, ACES in no way diminishes its rights as publisher. Sign only if *ALL* authors are subject to Crown Copyright).

This certifies that all authors of the above Paper are subject to Crown Copyright. (Appropriate documentation and instructions regarding form of Crown Copyright notice may be attached).

AUTHORIZED SIGNATURE TITLE OF SIGNEE

NAME OF GOVERNMENT BRANCH DATE FORM SIGNED

Information to Authors

ACES POLICY

ACES distributes its technical publications throughout the world, and it may be necessary to translate and abstract its publications, and articles contained therein, for inclusion in various compendiums and similar publications, etc. When an article is submitted for publication by ACES, acceptance of the article implies that ACES has the rights to do all of the things it normally does with such an article.

In connection with its publishing activities, it is the policy of ACES to own the copyrights in its technical publications, and to the contributions contained therein, in order to protect the interests of ACES, its authors and their employers, and at the same time to facilitate the appropriate re-use of this material by others.

The new United States copyright law requires that the transfer of copyrights in each contribution from the author to ACES be confirmed in writing. It is therefore necessary that you execute either Part A-Copyright Transfer Form or Part B-U.S. Government Employee Certification or Part C-Crown Copyright on this sheet and return it to the Managing Editor (or person who supplied this sheet) as promptly as possible.

CLEARANCE OF PAPERS

ACES must of necessity assume that materials presented at its meetings or submitted to its publications is properly available for general dissemination to the audiences these activities are organized to serve. It is the responsibility of the authors, not ACES, to determine whether disclosure of their material requires the prior consent of other parties and if so, to obtain it. Furthermore, ACES must assume that, if an author uses within his/her article previously published and/or copyrighted material that permission has been obtained for such use and that any required credit lines, copyright notices, etc. are duly noted.

AUTHOR/COMPANY RIGHTS

If you are employed and you prepared your paper as a part of your job, the rights to your paper initially rest with your employer. In that case, when you sign the copyright form, we assume you are authorized to do so by your employer and that your employer has consented to all of the terms and conditions of this form. If not, it should be signed by someone so authorized.

NOTE RE RETURNED RIGHTS: Just as ACES now requires a signed copyright transfer form in order to do "business as usual", it is the intent of this form to return rights to the author and employer so that they too may do "business as usual". If further clarification is required, please contact: The Managing Editor, R. W. Adler, Naval Postgraduate School, Code EC/AB, Monterey, CA, 93943, USA (408)656-2352.

Please note that, although authors are permitted to re-use all or portions of their ACES copyrighted material in other works, this does not include granting third party requests for reprinting, republishing, or other types of re-use.

JOINT AUTHORSHIP

For jointly authored papers, only one signature is required, but we assume all authors have been advised and have consented to the terms of this form.

U.S. GOVERNMENT EMPLOYEES

Authors who are U.S. Government employees are not required to sign the Copyright Transfer Form (Part A), but any co-authors outside the Government are.

Part B of the form is to be used instead of Part A only if all authors are U.S. Government employees and prepared the paper as part of their job.

NOTE RE GOVERNMENT CONTRACT WORK: Authors whose work was performed under a U.S. Government contract but who are not Government employees are required so sign Part A-Copyright Transfer Form. However, item 5 of the form returns reproduction rights to the U. S. Government when required, even though ACES copyright policy is in effect with respect to the reuse of material by the general public.

APPLIED COMPUTATIONAL ELECTROMAGNETICS SOCIETY JOURNAL
http://aces.ee.olemiss.edu

INFORMATION FOR AUTHORS

PUBLICATION CRITERIA

Each paper is required to manifest some relation to applied computational electromagnetics. **Papers may address general issues in applied computational electromagnetics, or they may focus on specific applications, techniques, codes, or computational issues.** While the following list is not exhaustive, each paper will generally relate to at least one of these areas:

1. **Code validation.** This is done using internal checks or experimental, analytical or other computational data. Measured data of potential utility to code validation efforts will also be considered for publication.

2. **Code performance analysis.** This usually involves identification of numerical accuracy or other limitations, solution convergence, numerical and physical modeling error, and parameter tradeoffs. However, it is also permissible to address issues such as ease-of-use, set-up time, run time, special outputs, or other special features.

3. **Computational studies of basic physics.** This involves using a code, algorithm, or computational technique to simulate reality in such a way that better, or new physical insight or understanding, is achieved.

4. **New computational techniques** or new applications for existing computational techniques or codes.

5. **"Tricks of the trade"** in selecting and applying codes and techniques.

6. **New codes, algorithms, code enhancement, and code fixes.** This category is self-explanatory, but includes significant changes to existing codes, such as applicability extensions, algorithm optimization, problem correction, limitation removal, or other performance improvement. **Note: Code (or algorithm) capability descriptions are not acceptable, unless they contain sufficient technical material to justify consideration.**

7. **Code input/output issues.** This normally involves innovations in input (such as input geometry standardization, automatic mesh generation, or computer-aided design) or in output (whether it be tabular, graphical, statistical, Fourier-transformed, or otherwise signal-processed). Material dealing with input/output database management, output interpretation, or other input/output issues will also be considered for publication.

8. **Computer hardware issues.** This is the category for analysis of hardware capabilities and limitations of various types of electromagnetics computational requirements. Vector and parallel computational techniques and implementation are of particular interest.

Applications of interest include, but are not limited to, antennas (and their electromagnetic environments), networks, static fields, radar cross section, inverse scattering, shielding, radiation hazards, biological effects, biomedical applications, electromagnetic pulse (EMP), electromagnetic interference (EMI), electromagnetic compatibility (EMC), power transmission, charge transport, dielectric, magnetic and nonlinear materials, microwave components, MEMS, RFID, and MMIC technologies, remote sensing and geometrical and physical optics, radar and communications systems, sensors, fiber optics, plasmas, particle accelerators, generators and motors, electromagnetic wave propagation, non-destructive evaluation, eddy currents, and inverse scattering.

Techniques of interest include but not limited to frequency-domain and time-domain techniques, integral equation and differential equation techniques, diffraction theories, physical and geometrical optics, method of moments, finite differences and finite element techniques, transmission line method, modal expansions, perturbation methods, and hybrid methods.

Where possible and appropriate, authors are required to provide statements of quantitative accuracy for measured and/or computed data. This issue is discussed in "Accuracy & Publication: Requiring, quantitative accuracy statements to accompany data," by E. K. Miller, *ACES Newsletter,* Vol. 9, No. 3, pp. 23-29, 1994, ISBN 1056-9170.

SUBMITTAL PROCEDURE

All submissions should be uploaded to ACES server through ACES web site (http://aces.ee.olemiss.edu) by using the upload button, journal section. Only pdf files are accepted for submission. The file size should not be larger than 5MB, otherwise permission from the Editor-in-Chief should be obtained first. Automated acknowledgment of the electronic submission, after the upload process is successfully completed, will be sent to the corresponding author only. It is the responsibility of the corresponding author to keep the remaining authors, if applicable, informed. Email submission is not accepted and will not be processed.

PAPER FORMAT (INITIAL SUBMISSION)

The preferred format for initial submission manuscripts is 12 point Times Roman font, single line spacing and single column format, with 1 inch for top, bottom, left, and right margins. Manuscripts should be prepared for standard 8.5x11 inch paper.

EDITORIAL REVIEW

In order to ensure an appropriate level of quality control, papers are peer reviewed. They are reviewed both for

technical correctness and for adherence to the listed guidelines regarding information content and format.

PAPER FORMAT (FINAL SUBMISSION)

Only camera-ready electronic files are accepted for publication. The term **"camera-ready" means that the material is neat, legible, reproducible, and in accordance with the final version format listed below.**

The following requirements are in effect for the final version of an ACES Journal paper:

1. The paper title should not be placed on a separate page. The title, author(s), abstract, and (space permitting) beginning of the paper itself should all be on the first page. The title, author(s), and author affiliations should be centered (center-justified) on the first page. The title should be of font size 16 and bolded, the author names should be of font size 12 and bolded, and the author affiliation should be of font size 12 (regular font, neither italic nor bolded).

2. An abstract is required. The abstract should be a brief summary of the work described in the paper. It should state the computer codes, computational techniques, and applications discussed in the paper (as applicable) and should otherwise be usable by technical abstracting and indexing services. The word "Abstract" has to be placed at the left margin of the paper, and should be bolded and italic. It also should be followed by a hyphen (—) with the main text of the abstract starting on the same line.

3. All section titles have to be centered and all the title letters should be written in caps. The section titles need to be numbered using roman numbering (I. II. ….)

4. Either British English or American English spellings may be used, provided that each word is spelled consistently throughout the paper.

5. Internal consistency of references format should be maintained. As a guideline for authors, we recommend that references be given using numerical numbering in the body of the paper (with numerical listing of all references at the end of the paper). The first letter of the authors' first name should be listed followed by a period, which in turn, followed by the authors' complete last name. Use a coma (,) to separate between the authors' names. Titles of papers or articles should be in quotation marks (" "), followed by the title of journal, which should be in italic font. The journal volume (vol.), issue number (no.), page numbering (pp.), month and year of publication should come after the journal title in the sequence listed here.

6. Internal consistency shall also be maintained for other elements of style, such as equation numbering. As a guideline for authors who have no other preference, we suggest that equation numbers be placed in parentheses at the right column margin.

7. The intent and meaning of all text must be clear. For authors who are not masters of the English language, the ACES Editorial Staff will provide assistance with grammar (subject to clarity of intent and meaning). However, this may delay the scheduled publication date.

8. Unused space should be minimized. Sections and subsections should not normally begin on a new page.

ACES reserves the right to edit any uploaded material, however, this is not generally done. It is the author(s) responsibility to provide acceptable camera-ready pdf files. Incompatible or incomplete pdf files will not be processed for publication, and authors will be requested to re-upload a revised acceptable version.

COPYRIGHTS AND RELEASES

Each primary author must sign a copyright form and obtain a release from his/her organization vesting the copyright with ACES. Copyright forms are available at ACES, web site (http://aces.ee.olemiss.edu). To shorten the review process time, the executed copyright form should be forwarded to the Editor-in-Chief immediately after the completion of the upload (electronic submission) process. Both the author and his/her organization are allowed to use the copyrighted material freely for their own private purposes.

Permission is granted to quote short passages and reproduce figures and tables from and ACES Journal issue provided the source is cited. Copies of ACES Journal articles may be made in accordance with usage permitted by Sections 107 or 108 of the U.S. Copyright Law. This consent does not extend to other kinds of copying, such as for general distribution, for advertising or promotional purposes, for creating new collective works, or for resale. The reproduction of multiple copies and the use of articles or extracts for commercial purposes require the consent of the author and specific permission from ACES. Institutional members are allowed to copy any ACES Journal issue for their internal distribution only.

PUBLICATION CHARGES

All authors are allowed for 8 printed pages per paper without charge. Mandatory page charges of $75 a page apply to all pages in excess of 8 printed pages. Authors are entitled to one, free of charge, copy of the journal issue in which their paper was published. Additional reprints are available for a nominal fee by submitting a request to the managing editor or ACES Secretary.

Authors are subject to fill out a one page over-page charge form and submit it online along with the copyright form before publication of their manuscript.

ACES Journal is abstracted in INSPEC, in Engineering Index, DTIC, Science Citation Index Expanded, the Research Alert, and to Current Contents/Engineering, Computing & Technology.